

INFORMATION TO USERS

This manuscript has been reproduced from the microfilm master. UMI films the text directly from the original or copy submitted. Thus, some thesis and dissertation copies are in typewriter face, while others may be from any type of computer printer.

The quality of this reproduction is dependent upon the quality of the copy submitted. Broken or indistinct print, colored or poor quality illustrations and photographs, print bleedthrough, substandard margins, and improper alignment can adversely affect reproduction.

In the unlikely event that the author did not send UMI a complete manuscript and there are missing pages, these will be noted. Also, if unauthorized copyright material had to be removed, a note will indicate the deletion.

Oversize materials (e.g., maps, drawings, charts) are reproduced by sectioning the original, beginning at the upper left-hand corner and continuing from left to right in equal sections with small overlaps.

Photographs included in the original manuscript have been reproduced xerographically in this copy. Higher quality 6" x 9" black and white photographic prints are available for any photographs or illustrations appearing in this copy for an additional charge. Contact UMI directly to order.

Bell & Howell Information and Learning
300 North Zeeb Road, Ann Arbor, MI 48106-1346 USA
800-521-0600

UMI[®]

**THE FLORIDA STATE UNIVERSITY
COLLEGE OF ARTS AND SCIENCES**

OCEAN DYNAMICS AROUND NEW ZEALAND

By

CHARLES E. TILBURG

**A dissertation submitted to the
Department of Oceanography
in partial Fulfillment of the
requirements for the degree of
Doctor of Philosophy**

**Degree Awarded:
Fall Semester, 2000**

UMI Number: 9990405



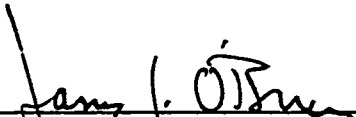
UMI Microform 9990405

Copyright 2001 by Bell & Howell Information and Learning Company.

All rights reserved. This microform edition is protected against
unauthorized copying under Title 17, United States Code.

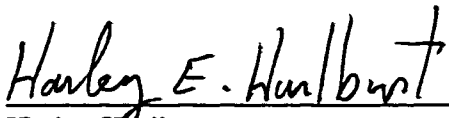
Bell & Howell Information and Learning Company
300 North Zeeb Road
P.O. Box 1346
Ann Arbor, MI 48106-1346

The members of the Committee approve the dissertation of Charles E. Tilburg defended on September 29, 2000.

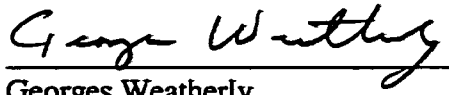

James J. O'Brien
Professor Directing Dissertation


Eutiquio Young
Outside Committee Member


Allan Clarke
Committee Member


Harley Hurlburt
Committee Member


William Landing
Committee Member


Georges Weatherly
Committee Member

To Christine

ACKNOWLEDGMENTS

No one can complete a dissertation without significant help from many different sources. I have had the privilege to learn from my fellow students and professors through their example, enthusiasm, and advice. For these lessons and experiences, I am eternally thankful. There is a long list of people who have helped me, encouraged me, and challenged me. Thank you Dr. James O'Brien for helping me become a better scientist. Thank you Dr. Harley Hurlburt for helping me choose my research topic, providing me with advice and encouragement when I most needed them, and showing me what it means to be a scientist. Thanks Joe Metzger and Dr. Jay Shriver for providing answers to countless questions. Thank you Dr. Allan Clarke, Dr. William Landing, Dr. Georges Weatherly, and Dr. Eutiquio Young for your advice and time. Thanks Dr. Steven Morey, soon to be Drs. Luis Zamudio and Paige Leitman, and countless others at the Center for Ocean-Atmospheric Prediction Studies and the Department of Oceanography for your encouragement, scientific input, and support. Thank you Mom and Dad for encouraging me while I was in school. But most of all thank you Christine for putting up with me while I wrote this dissertation!

Throughout my graduate studies I have received financial support from the Department of Defense through a National Defense Science and Engineering Graduate

Fellowship. This work is a contribution to the 6.1 Project “Thermodynamic and Topographic Forcing in Global Ocean Models” sponsored by the Office of Naval Research under program element 601 153N. The computations in this paper were performed on AHPCRC, ARSC, CEWES and NAVO Cray T3Es using grants of computer time from the Defense Department High Performance Computing Modernization Office. The 1/16° global simulations were performed under the FY97 DOD HPC Challenge project “1/16° Global Ocean Model” on the CEWES T3E and using early access on the NAVO T3E.

TABLE OF CONTENTS

LIST OF TABLES	vii
LIST OF FIGURES.....	viii
ABSTRACT.....	xii
1. INTRODUCTION.....	I
2. THE OCEAN MODEL	10
3. CLIMATOLOGICAL DYNAMICS.....	16
<i>a. Linear Dynamics</i>	<i>16</i>
<i>b. Nonlinear Dynamics: Flat Bottom and Reduced Gravity Cases</i>	<i>31</i>
<i>c. Nonlinear Dynamics: Realistic Bottom Topography Case</i>	<i>53</i>
4. SUMMARY AND CONCLUSIONS	81
APPENDIX A: Explanation of Symbols and Notations	86
APPENDIX B: Explanation of Baroclinic Instability Analysis	89
APPENDIX C: Explanation of Barotropic Instability Analysis.....	96
REFERENCES	100
BIOGRAPHICAL SKETCH.....	106

LIST OF TABLES

Table 1. World Ocean Simulations.....	14
Table 2. Additional Model Parameters	15
Table 3. Mean Transport from Selected Sections	22
Table 4. Mean interface depths (m) at land boundaries south of Australia and New Zealand	51

LIST OF FIGURES

Figure 1. Schematic diagram of the major surface currents, features and transport sections (gray lines) in the Tasman Sea and the region surrounding New Zealand	2
Figure 2. Sea floor topography surrounding New Zealand	3
Figure 3. Climatological dynamic sea surface height with respect to 2000 db in the region north of New Zealand compiled by Roemmich and Sutton (1998)	7
Figure 4a. Mean transport streamfunctions from the $1/8^\circ$ linear 1.5 layer simulation RG1 for the Southern Hemisphere depicting the interbasin supergyre and the nested intrabasin gyres	18
Figure 4b. Mean transport streamfunctions from the $1/8^\circ$ linear 1.5 layer simulation RG1 for the region surrounding New Zealand	19
Figure 5. Mean transport streamfunctions from the $1/8^\circ$ linear 1.5 layer simulation RG2 with New Zealand removed from the flow field	25
Figure 6. Annual mean wind stress curl field derived from Hellerman and Rosenstein (1983)	26
Figure 7. Illustration of the mass balance of the region from 32°S to 39°S	28
Figure 8. Mean transport streamfunctions from the $1/8^\circ$ linear 1.5 layer simulations of (a) RG3 and (b) RG4	30

Figure 9a. Mean surface currents from the $1/8^\circ$ nonlinear six-layer simulation with a flat bottom, FB	32
Figure 9b. Mean surface currents from the $1/8^\circ$ nonlinear 5.5 layer reduced gravity simulation, RG5.5	36
Figure 10. Longitude-time plots of sea surface height deviations at 33°S from (a) RG5.5, (b) FB, and (c) RB8a	37
Figure 11. Mean surface layer pressures (red) of FB overlaid on abyssal layer pressures (black)	39
Figure 12. (a) Velocity within the simulated Tasman Front (FB) as a function of depth (b) Velocity of FB separated into the barotropic mode and five baroclinic modes	43
Figure 13. a) Imaginary component of phase speed of the disturbance as a function of wave number for FB. b) Real component of phase speed of the disturbance as a function of wave number for FB.	44
Figure 14. Average velocities of the surface jet associated with the Tasman Front from FB at 165°E	46
Figure 15. Latitude-time plot of normalized dQ/dy at 165°E from FB where Q is the absolute vorticity calculated from the depth-averaged velocities.....	48
Figure 16. Mean surface currents from the $1/8^\circ$ nonlinear six-layer simulation with realistic bottom topography, RB8a, superimposed on the bottom topography	54

Figure 17. (a) Velocity within the simulated Tasman Front (RB8a) as a function of depth (b) Velocity of RB8a separated into the barotropic mode and five baroclinic modes	58
Figure 18. Average velocities of the surface jet associated with the Tasman Front from RB8a at 165°E.	59
Figure 19. Latitude-time plot of normalized dQ/dy at 165°E from RB8a where Q is the absolute vorticity calculated from the depth-averaged velocities.	60
Figure 20. Mean surface currents from the 1/16° nonlinear six-layer simulation with realistic bottom topography, RB16, superimposed on the bottom topography	61
Figure 21. Sea surface height variability obtained from (a) RB16 and (b) TOPEX/Poseidon altimeter data.....	63
Figure 22. Mean surface layer eddy kinetic energy (EKE) of (a) RB8a and (b) RB16 and abyssal layer EKE of (c) RB8a and (d) RB16.....	65
Figure 23. Average velocities of the surface jet associated with the Tasman Front from RB16 at 165°E.	67
Figure 24. Latitude-time plot of normalized dQ/dy at 165°E from RB16 where Q is the absolute vorticity calculated from the depth-averaged velocities.	68
Figure 25a. Mean abyssal layer currents (black arrows) from the 1/16° nonlinear six-layer simulation with realistic bottom topography, RB16, superimposed on sea surface height in the vicinity of the Tasman Front.....	70
Figure 25b. Mean abyssal layer currents (black arrows) from 1/16° nonlinear six-layer simulation with realistic bottom topography, RB16, superimposed on sea surface height southeast of New Zealand	73

Figure 25c. Mean abyssal layer currents (black arrows) from $1/16^\circ$ nonlinear six-layer simulation with realistic bottom topography, RB16, superimposed on bottom topography.	74
Figure 26. Mean surface currents from the $1/8^\circ$ nonlinear six-layer simulation with realistic bottom topography and New Zealand removed, RB8b, superimposed on the bottom topography.....	76
Figure 27. Abyssal layer currents (black arrows) from nonlinear two-layer simulation superimposed on the bottom topography	78
Figure 28. Surface transport streamfunctions from two-layer simulation at a) $T = 0$ years (no abyssal flow), b) $T = 3$ years, c) $T = 7$ years, d) $T = 80$ years.	79

ABSTRACT

The dynamics of the flow field surrounding New Zealand is investigated using a series of global ocean models. The physical mechanisms governing the direction, magnitude, and location of the East Australian Current (EAC), the Tasman Front, the East Auckland Current (EAUC), the East Cape Current (ECC), and the Southland Current are studied using numerical simulations whose complexity is systematically increased. As new dynamics are added to each successive simulation, their direct and indirect effects on the flow field are examined. The simulations contain horizontal resolutions of $1/8^\circ$ or $1/16^\circ$ for each variable and vertical resolutions ranging from 1.5 layer reduced gravity to six-layer finite depth with realistic bottom topography. All simulations are forced by the Hellerman and Rosenstein monthly wind stress climatology. Global simulations are used to fully investigate the effect of global scale circulation on local currents and their governing dynamics. Analysis of these simulations shows several factors play a critical role in governing the behavior of the examined currents. These factors include (1) mass balance of water pathways through the area, (2) gradients in the wind stress curl, (3) nonlinear flow instabilities, and (4) upper ocean - topographic coupling due to mixed baroclinic and barotropic instabilities. Transport streamfunctions of a linear reduced gravity model reproduce the large-scale features well but produce an EAUC and

Southland Current flowing in the wrong direction. The residual of the mass balance of the transport through the Tasman Sea, the basinwide transport at 32°S, and the northward transport of the South Pacific subtropical gyre east of New Zealand determines the direction of the EAUC. The six-layer nonlinear model allows isopycnal outcropping which changes the transport through the Tasman Sea and produces an EAUC flowing in the observed direction. Gradients in the zonally integrated wind stress curl field determine the coastal separation points of the EAC, the EAUC, and the ECC, while a combination of nonlinear flow instabilities and upper ocean – topographic coupling contribute to the formation of meanders in the Tasman Front. Increased resolution increases the mixed baroclinic-barotropic instabilities and thus the upper ocean – topographic coupling and surface variability, giving a more accurate simulation of topographically controlled mean meanders in the Tasman Front. The location and direction of the Southland Current is due to the westward propagation of topographically influenced surface layer thicknesses.

1. INTRODUCTION

The East Australian Current is the western boundary current of the South Pacific subtropical gyre. The partial separation of this current from the coast of Australia and its subsequent eastward flow into the South Pacific creates one of the most complicated and dynamically interesting regions in the world's oceans (Godfrey et al., 1980). Extending from the Coral Sea to the Tasman Sea, the East Australian Current (hereafter called the EAC) system generates numerous eddies and has several branches including the Tasman Front, the East Auckland Current (EAUC), the East Cape Current (ECC), and the EAC extension. The Southland Current is a portion of the Southern Hemisphere Subtropical Front (STF) that extends along the eastern coast of South Island and separates from the coast near the Chatham Rise (Chiswell, 1996). A schematic of the flow field (Fig. 1) reveals a boundary current system that affects the flow along the entire eastern coasts of Australia and New Zealand. The region is highly variable due to eddy generation and extensive current meandering. Bottom-steering significantly affects the surface flow, and a large part of the complexity of the region can be attributed to the varied bottom topography (Fig. 2), which is dominated by the extensive New Zealand submarine platform.

Unlike other western boundary currents, such as the Kuroshio and the Gulf

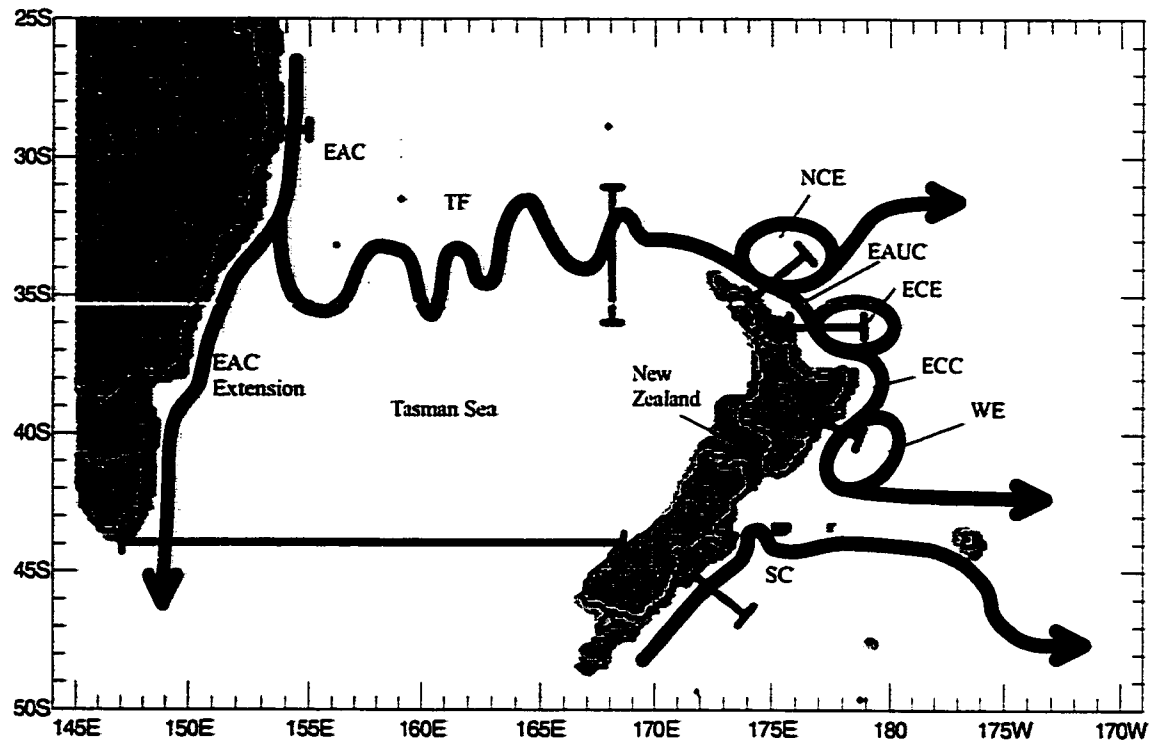


Figure 1. Schematic diagram of the major surface currents, features and transport sections (gray lines) in the Tasman Sea and the region surrounding New Zealand. EAC = East Australian Current, EAUC = East Auckland Current, ECC = East Cape Current, TF = Tasman Front, SC = Southland Current, NCE = North Cape Eddy, ECE = East Cape Eddy, WE = Wairarapa Eddy

CI = 500 m

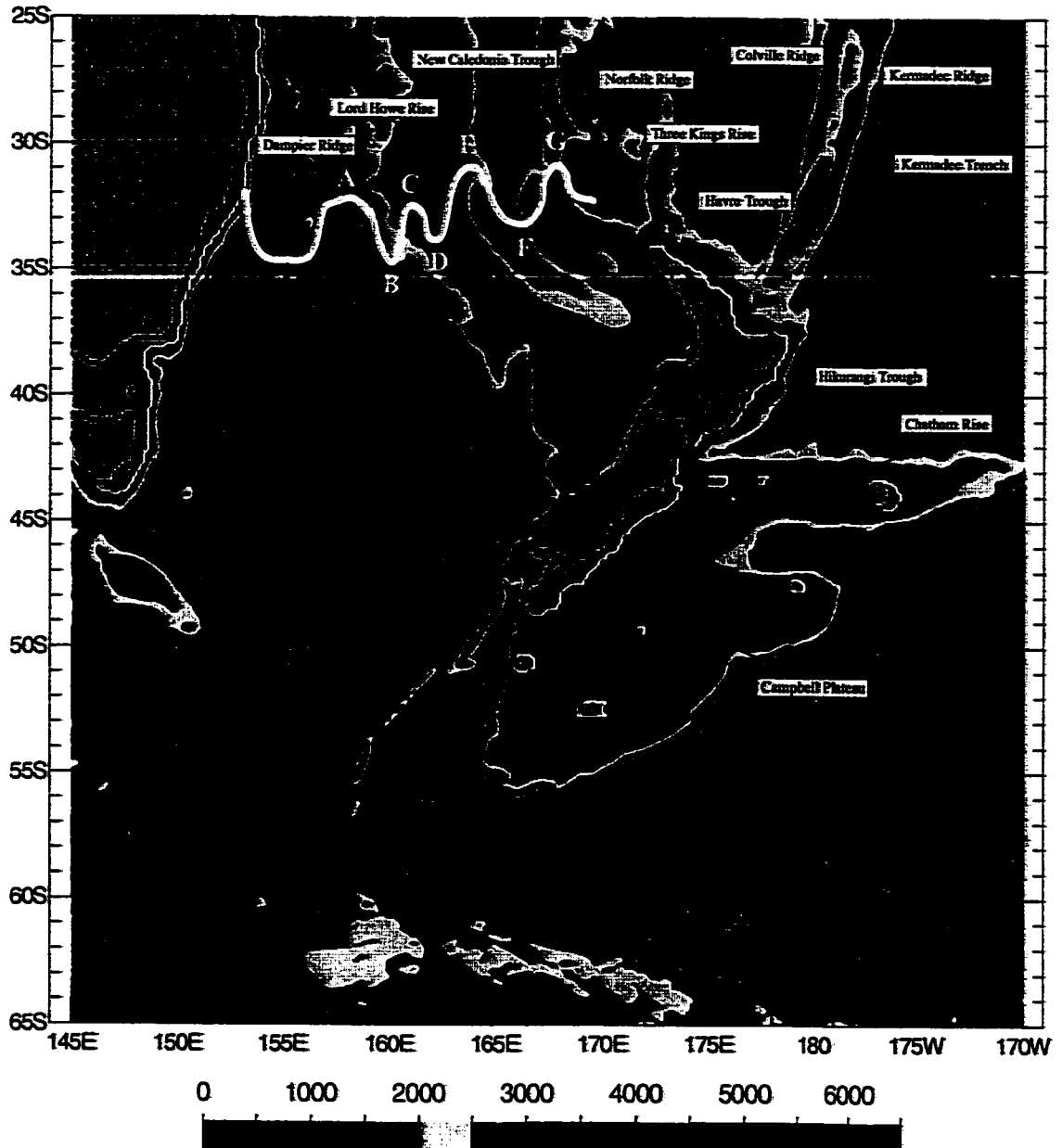


Figure 2. Sea floor topography surrounding New Zealand. Note the large New Zealand submarine platform and the extensive ridges and troughs throughout the area. The white line represents the most probable path of the Tasman Front adapted from a similar figure by Mulhearn (1987) and a compilation of observations by Stanton (1979). The letters (A-G) associated with the meanders are used to distinguish each meander for discussion in later sections.

Stream, the strength of the EAC varies substantially with time. The mass transport within eddies spawned by the EAC can be much larger than its mean flow (Ridgway and Godfrey, 1997). Composites of ship and satellite observations show that a portion of the EAC leaves the coast of Australia between 30°S and 34°S, while a weaker flow continues southward attached to the coast. Godfrey et al. (1980) demonstrated that, although the exact separation point varies seasonally, the mean behavior of the EAC flow field is significantly different on either side of a line extending south-southeast of Sugarloaf Point (32.5°S). Just south of Sugarloaf Point, northward shelf currents are common and eddies are essentially circular, while just north of this point the currents are southward and eddies are much more elongated. Although the majority of the EAC separates from the Australian coast and either proceeds eastward or recirculates, as much as 1/3 of the original EAC exits the southern edge of the Tasman Sea, trapped against the western boundary (Ridgway and Godfrey, 1997; Chiswell et al., 1997).

As the separated portion of the EAC proceeds eastward towards New Zealand, it crosses the northern edge of the Tasman Sea following a narrow, meandering pathway. Warren (1970) first suggested that this flow, associated with the Tasman Front, is a zonal jet connecting the EAC with the western boundary currents on the eastern coast of New Zealand. Stanton (1976) first identified a variable frontal jet near the Norfolk Ridge between 165°E and 169°E. Denham and Crook (1976) showed that the Tasman Front extends from the Norfolk Ridge to the Lord Howe Rise (~160°E). An oceanographic survey detailed by Andrews et al. (1980) described a front that exists along the entire northern edge of the Tasman Sea. Other investigations of the meanders and variability of

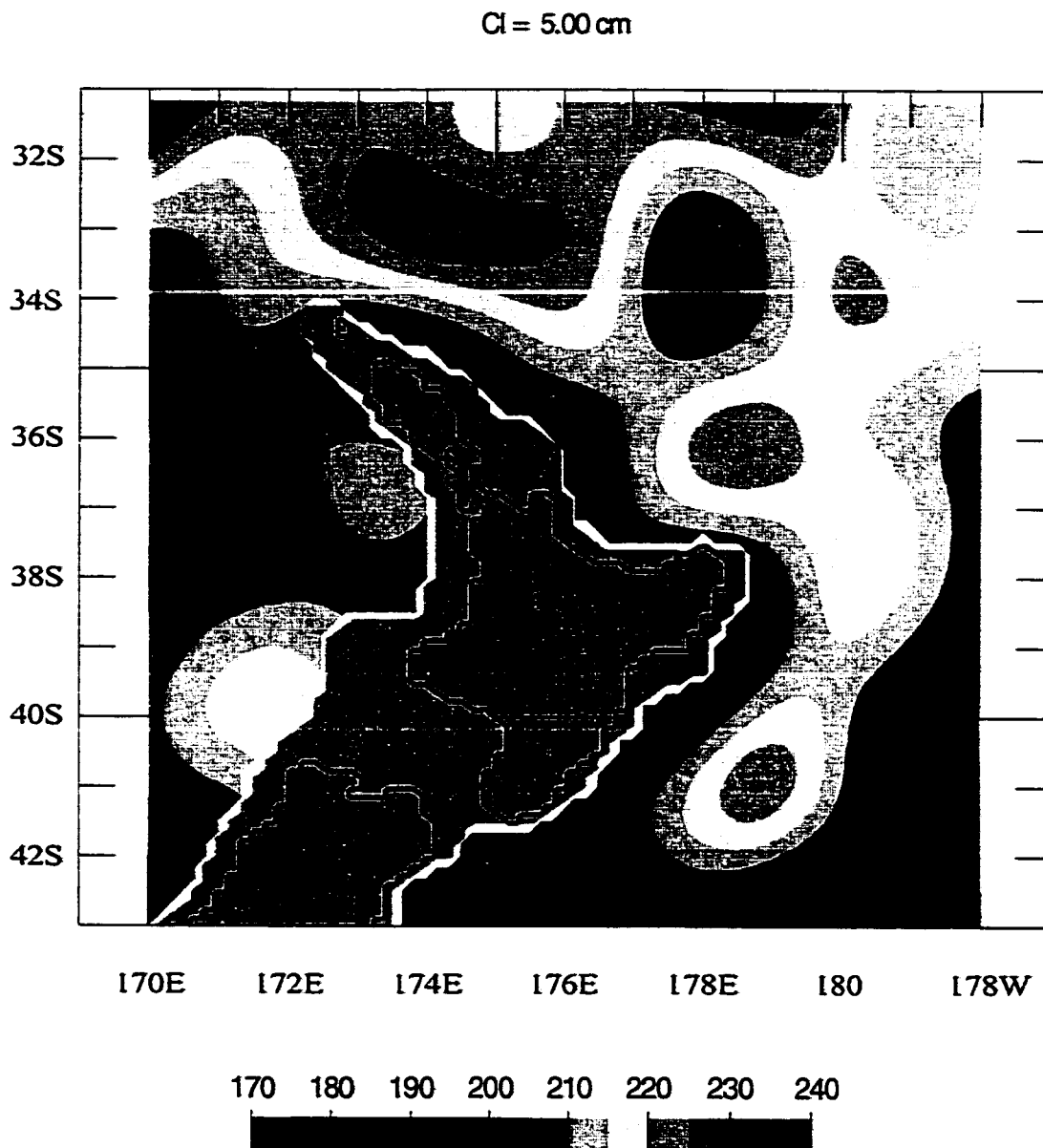
this front (Stanton 1979, 1981; Mulhearn, 1987) at different locations demonstrated that, although the Tasman Front is highly variable, its mean path follows meanders that are permanent features of the flow field. The most probable path (shown as white line in Fig. 2) was constructed by combining a similar diagram by Mulhearn (1987) and a mean frontal path obtained from a number of cruises described by Stanton (1979). Mulhearn (1987) used a series of satellite infrared images to determine the most probable path of the Tasman Front from 153°E to 164°E during 29 months from March 1982 to April 1985. Stanton (1979) showed the location of the Tasman Front between 166°E and 170°E for five different cruises from 1966 to 1975. Combining these observations reveals a most probable path of the Tasman Front that leaves the coast of Australia at 153°E, 33°S and meanders eastward between latitudes of 36°S and 32°S. Although the front shows substantial variability, the mean path includes several permanent meanders.

Heath (1985a) provided a thorough summary of the flow field surrounding New Zealand. Once the eastward flow along the Tasman Front reaches the northernmost point of New Zealand, it turns southeastward becoming the EAUC and following the northeast coastline of New Zealand's North Island. Although the majority of the flow gradually separates from the coast and continues eastward, a small portion remains attached to the coast and continues to the easternmost tip of North Island, East Cape. As the flow rounds East Cape, it becomes the East Cape Current (ECC). The ECC separates from North Island at approximately 42°S proceeds eastward slightly north of the Chatham Rise (Heath, 1985a,b). The Southland Current is actually a portion of the STF that extends northward along the eastern coast of South Island (Chiswell, 1996; Stramma et al., 1995).

eastward along the Chatham Rise, and southward to 47°S beyond 177°W (Uddstrom and Oien, 1999).

Although pathways of the EAUC and the ECC are highly variable (Laing et al., 1996), a mean dynamic height field (Fig. 3) presented by Roemmich and Sutton (1998) shows that three quasi-stationary eddies are present in the flow field. The North Cape Eddy (NCE) whose southern edge comprises the beginning of the EAUC is centered near 173.5°E, 33°S. The East Cape Eddy (ECE) whose southern edge comprises the end of the EAUC and the beginning of the ECC is centered near 178.5°E, 35.5°S. The Wairarapa Eddy (WE) whose western and southern edges comprise the majority of the ECC is centered near 178.5°E, 41°S. Also present in the dynamic height field is a relative low between NCE and ECE. Uddstrom and Oien (1999) using satellite derived sea surface temperatures (SST) were also able to identify the NCE and the WE although they did not find a robust ECE.

Although there have been relatively few numerical simulations of this region, both linear and nonlinear models have been used to study its dynamics. Godfrey (1973) presented a qualitative study of the EAC using results derived from the regional Bryan and Cox (1968) model, an idealized flat bottom six-level nonlinear simulation using annual wind stress and differential heating. He found that the simulated eddies and fluctuations were similar to observations, but that the model was unable to reproduce the observed vorticity balance or seasonality of the EAC due to its lack of bottom topography and use of annual wind stress climatology. Bye et al. (1979), using a diagnostic linear regional model driven by specified density, wind stress, and flow boundaries, obtained a



(From Roemmich and Sutton, 1998)

Figure 3. Climatological dynamic sea surface height with respect to 2000 db in the region north of New Zealand compiled by Roemmich and Sutton (1998). Note the presence of the three eddies labeled on Figure 1: NCE, ECE, and WE along with an unnamed low.

steady-state flow field around New Zealand, reproducing the EAUC, the ECC, and the Southland Current but were unable to resolve the quasi-stationary eddies surrounding New Zealand. De Szoeke (1987) used a linear reduced gravity 3.5 layer model driven by annual wind stress encompassing the South Pacific from 57°S to almost the equator. He reproduced the large scale features well, including the EAC separation and basin wide density surfaces. His model based on that of Luyten et al. (1983) did not incorporate cross-isopycnal flux, which he suspected was responsible for weaker than observed shallow currents.

Semtner and Chervin (1992) briefly examined this region in the context of their $\frac{1}{2}^\circ$ 20 level global model that incorporated realistic bottom topography and was driven by Hellerman and Rosenstein (1983) (HR) monthly wind stress climatology. They found a highly variable EAC ranging from 7 to 47 Sv ($10^6 \text{ m}^3\text{s}^{-1}$) flowing southward and a highly baroclinic transport through the Tasman Sea, ranging from 3 Sv northward to 10 Sv southward. The simulated surface flow within the Tasman Sea was northward while the deeper levels were southward. Examination of the surface flow field revealed the presence of the three observed eddies surrounding New Zealand, realistic meanders in the Tasman Front, and currents surrounding New Zealand flowing in the observed direction. Ridgway and Godfrey (1994) compared their observations to a simple linear Sverdrup-Munk model of the world ocean by Godfrey (1989), finding that the linear model produced the observed patterns of EAC separation and transport through the Tasman Sea. They noted that the southward transport through the Tasman Sea was higher than

observed and that the linear model was unable to reproduce the eddies or meanders of the observed flow. Moore and Wilkin (1998) examined the variability of the South Pacific deep western boundary current using the 20 level Los Alamos National Laboratories (LANL) model and current meter observations at 32.5°S east of the Kermadec Ridge. The nonlinear model contained 0.28° horizontal resolution and was forced by European Centre for Medium-Range Weather Forecasts (ECMWF) 3 day winds. Carter and Wilkin (1999) examined the abyssal circulation off eastern New Zealand using the LANL model, hydrographic measurements, and geological proxies.

This earlier work is expanded by using 1/8° and 1/16° multiple layered global ocean models to examine the dynamics governing the surface flow field encompassing the Tasman Front, EAUC, ECC, and Southland Current. Since the EAC and the flow around New Zealand are situated in one of the most diverse and interconnected regions of the world's oceans, influenced by the Antarctic Circumpolar Current (ACC), the Indo-Pacific Throughflow (IPT), and the global thermohaline circulation, a global model is necessary to capture the range of essential dynamics. Increasingly realistic and dynamically complex simulations are performed to determine which dynamics are most important in governing the different aspects of the flow field. The ocean model and numerical simulations used in this investigation are discussed in chapter 2. The results and dynamical interpretation of the different climatological simulations are discussed in chapter 3, while a summary and conclusions are given in chapter 4.

2. THE OCEAN MODEL

The numerical model used in these investigations is the Naval Research Laboratory Layered Ocean Model (NLOM), a primitive equation layered formulation whose equations have been integrated through each layer. This model is a descendent of the model detailed by Hurlburt and Thompson (1980) with greatly expanded capabilities (Wallcraft, 1991; Wallcraft and Moore, 1997; Moore and Wallcraft, 1998). The equations for the n -layer finite depth, hydrodynamic model are given below for layers $k=1 \dots n$ with $k=1$ for the top layer. In places where k is used to index model interfaces, $k=0$ is the surface and $k=n$ is the bottom.

$$\begin{aligned}
 & \frac{\partial U_k}{\partial t} + \frac{1}{a \cos \theta} \left[\frac{\partial(U_k u_k)}{\partial \phi} + \frac{\partial(V_k u_k \cos \theta)}{\partial \theta} - V_k (u_k \sin \theta + a \Omega \sin 2\theta) \right] = \\
 & + \max(0, -\omega_{k-1}) u_{k-1} + \max(0, \omega_k) u_{k+1} - (\max(0, -\omega_k) + \max(0, \omega_{k-1})) u_k \\
 & + \max(0, -C_M \omega_{k-1}) (u_{k-1} - u_k) + \max(0, C_M \omega_k) (u_{k+1} - u_k) \\
 & - \frac{h_k}{a \cos \theta} \sum_{j=1}^n G_{kj} \frac{\partial(h_j - H_j)}{\partial \phi} + (\tau_{\phi, k-1} - \tau_{\phi, k}) / \rho_o + \frac{A}{a^2 \cos^2 \theta} \left[\frac{\partial(h_k e_{\phi k} \cos \theta)}{\partial \phi} + \frac{\partial(h_k e_{\phi k} \cos^2 \theta)}{\partial \theta} \right]
 \end{aligned} \tag{1}$$

$$\begin{aligned}
& \frac{\partial V_k}{\partial t} + \frac{1}{a \cos \theta} \left[\frac{\partial (U_k v_k)}{\partial \phi} + \frac{\partial (V_k v_k \cos \theta)}{\partial \theta} + U_k (\mu_k \sin \theta + a \Omega \sin 2\theta) \right] = \\
& + \max(0, -\omega_{k-1}) v_{k-1} + \max(0, \omega_k) v_{k+1} - (\max(0, -\omega_k) + \max(0, \omega_{k-1})) v_k \\
& + \max(0, -C_M \omega_{k-1}) (v_{k-1} - v_k) + \max(0, C_M \omega_k) (v_{k+1} - v_k) \\
& - \frac{h_k}{a} \sum_{j=1}^n G_{kj} \frac{\partial (h_j - H_j)}{\partial \theta} + (\tau_{\theta_{k-1}} - \tau_{\theta_k}) / \rho_o + \frac{A}{a^2 \cos^2 \theta} \left[\frac{\partial (h_k e_{\phi\theta_k} \cos \theta)}{\partial \phi} + \frac{\partial (h_k e_{\theta\theta_k} \cos^2 \theta)}{\partial \theta} \right] \\
& \frac{\partial h_k}{\partial t} + \nabla \cdot \bar{V}_k = \omega_k - \omega_{k-1}
\end{aligned} \tag{2}$$

$$\tag{3}$$

Notation that is common in oceanography is used in the model equations. A full explanation of the parameters and notation used in these equations is given in Appendix A. The model boundary conditions are kinematic and no slip. The model equations are integrated on a C-grid (Mesinger and Arakawa, 1976) using a semi-implicit numerical scheme for the finite depth simulations and an explicit numerical scheme for reduced gravity simulations.

Although thermodynamic versions of the model exist (Metzger et al., 1992; Heburn, 1994; Metzger and Hurlburt, 1996), the versions used in this investigation are hydrodynamic with constant density in each layer. As a result, thermal forcing and steric anomalies due to seasonal heating and cooling are excluded. The model does permit

isopycnal outcropping via ventilation of model layer interfaces. This ventilation is achieved by a process known as “hydromixing” (Wallcraft, 1991), which is described below. When any layer’s thickness decreases to a certain minimum value (h_k^+), water is entrained from the layer below at a velocity (ω_k) needed to prevent negative layer thickness. Mass and volume are conserved within each layer by compensating domain wide diapycnal mixing. The pattern of vertical mixing is determined by isopycnal outcropping and observed oxygen saturation values as discussed in detail by Shriver and Hurlburt (1997). Isopycnal outcropping and vertical mixing permit overturning circulations in the vertical, such as the thermohaline circulation and meridional overturning and allow shallow layers on basin wide scales. Isopycnal outcropping and vertical mixing can also affect horizontal mass transports, which is an especially important mechanism in our region of interest, as will be seen in section 3b.

A modified version of the 1/12° ETOP05 bottom topography (National Oceanic and Atmospheric Administration, 1986) is used in the simulations requiring realistic bottom topography. The topography is first interpolated to the model grid and then smoothed twice with a nine-point smoother to reduce energy generation at smaller scales that are poorly resolved by the model. The maximum depth of the model is set at 6500 m. The minimum depth, set at 200 m, is used as the model boundary with a few exceptions where shallower depths are needed to connect semi-enclosed seas. The bottom topography is confined to the lowest layer (Hurlburt and Thompson, 1980) to prevent numerical difficulties arising when moving layer interfaces intersect with sloping topography and to greatly decrease the computer time/model year. Two of the main

reasons for including bottom topography, regulating baroclinic instabilities and forcing abyssal flow to follow f/h contours, are relatively unaffected by this modification of the bottom topography.

The simulations used in this investigation are defined in Table 1, and the model parameters are given in Tables 1 and 2. The density for each layer was obtained from Levitus (1982) ocean climatology. In the six-layer simulations, the depths of the two upper layers were chosen to represent a surface layer and a layer containing the equatorial undercurrent, while the mean fifth interface depth was chosen to represent the boundary between intermediate and abyssal water. The simulations were forced by the Hellerman and Rosenstein (1983) monthly wind stress climatology to statistical equilibration and were initialized from equilibrated lower resolution simulations. All means shown are calculated from the last four years of the simulation. The history plots are generated from the last two years of the simulations. Several model-data comparisons for different $1/8^\circ$ and $1/16^\circ$ simulations have been performed for a Pacific version of this model (e.g. Mitchum, 1995; Hurlburt et al., 1996; Mitchell et al., 1996; and Metzger and Hurlburt, 1996). Other studies have used variations of the global model to investigate the effect of the IPT on the global thermohaline circulation (Shriver and Hurlburt, 1997) and the role of Halmahera Island in the transport pathways of Pacific waters to the Indian Ocean (Morey et al., 1999).

Table 1. World Ocean Simulations

Experiment	A m^2/s	H m	Wind Forcing	Model Years Spanned	Comments
RG1	100	250/∞	Seasonal	250-325	Linear
RG2	100	250/∞	Seasonal	325-450	Linear. removed New Zealand
RG3	100	250/∞	Seasonal	325-518	Linear. friction patch in Tasman Sea
RG4	100	250/∞	Seasonal	325-578	Linear. Indo-Pacific Throughflow closed
FB	100	155/185/210/ 225/225/5500	Seasonal	282-299	Nonlinear, flat bottom
RB8a	100	155/185/260/ 375/525/variable	Seasonal	860-975	Nonlinear, realistic bottom topography
RB8b	100	155/185/260/ 375/525/variable	Seasonal	976-990	Nonlinear, realistic bottom topography – removed New Zealand
RB16	20	155/185/260/ 375/525/variable	Seasonal	847-899	Nonlinear, realistic bottom topography

In cases using realistic bottom topography, a scaling factor was used to restrict bottom topography features to layer 6. The model is run in linear mode by scaling the winds down by a factor of 1000. The model fields are then scaled up by a factor of 1000 to restore them to their proper magnitude.

Table 2. Additional Model Parameters

Parameters	Value	Simulations	Definition
C_b	0	1,2,3,4	bottom drag coefficient
	2×10^{-3}	5,6,7,8	
C_k	0	1,2,3,4,5,6,7,8	k th interfacial stress coefficient
g	9.8 m/s^2	1,2,3,4,5,6,7,8	acceleration due to gravity
h_{k*}	N/A	1,2,3,4	thickness of layer k at which entrainment starts
	50/40/40/40/40 m	5,6,7,8	
σ_k	25.45/27.55	1,2,3,4	density of layer k
	25.24/26.47/26.99/	5	
	27.23/27.39/27.77		
	25.25/26.59/27.03/	6,7,8	
$\Delta\theta$	$1/8^\circ$	1,2,3,4,5,6,7	latitudinal grid resolution
	$1/16^\circ$	8	
$\Delta\phi$	$45/256^\circ$	1,2,3,4,5,6,7	longitudinal grid resolution
	$45/512^\circ$	8	
ω_k	N/A	1,2,3,4	k th interface vertical reference mixing velocity
	0.02 m/s	5	
	0.04 m/s	6,7	
	0.05/0.06/0.05/	8	
	0.05/0.05 m/s		

The numbers 1 through 8 in the simulations column refer to the simulations as follows: 1, RG1; 2, RG2; 3, RG3; 4, RG4; 5, FB; 6, RB8a; 7, RB8b; 8, RB16. N/A indicates a model parameter that is not applicable for that simulation.

3. CLIMATOLOGICAL DYNAMICS

We rely on the modularity of NLOM, progressing from a simple linear reduced gravity $1/8^\circ$ model to highly realistic $1/16^\circ$ six-layer simulations incorporating nonlinear dynamics and realistic bottom topography to determine which dynamics govern specific behavior in the flow field. As the simulations increase in realism, they more closely reproduce the observed features, suggesting that the new dynamics introduced with the new simulation are responsible for the observed features. Qualitative and quantitative model-data comparisons are made throughout this discussion to determine how well each successive simulation reproduces the observed flow field.

a. Linear Dynamics

The lowest order estimate of the dynamics governing the flow around New Zealand is a linear reduced gravity model (labeled RG1, Table 1), whose dynamics are essentially those of a Sverdrup (1947) interior with Munk (1950) western boundary layers and globally applied horizontal friction. The flow and sea surface height are calculated using a global numerical model with realistic coastline geometry and monthly

climatological wind forcing. The model has one vertical mode and a bottom layer that is infinitely deep and at rest. Since the linear simulation reveals the lowest order response to external forcing, it can be used as a baseline for the more complicated simulations that incorporate nonlinearities, bottom topography, multiple vertical modes, flow instabilities, and isopycnal outcropping.

The transport streamfunctions of the 1.5 layer linear $1/8^\circ$ reduced gravity simulation (here after referred to as RG1) driven by the HR monthly wind stress climatology (Fig. 4a) reveal a system of nested anticyclonic gyres encompassing the Southern Hemisphere. Nested gyres were also identified numerically by De Szoeke (1987) and Godfrey (1989) and observationally by Davis (1998) using neutral buoyancy floats. A large supergyre extends through all three oceans following two different paths connecting the Pacific and Indian Oceans: one path extends through the IPT (purple, dark blue, and blue contours), while the other travels south of Australia (light blue and blue-green contours). Two smaller gyres comprise an inner nesting: one gyre occupies the South Atlantic and Indian Oceans (dark green to maroon contours) and the other occupies the South Pacific Ocean and extends south of Australia (dark green contour bounded on west by Australia). Three gyres, one bounded on the west by Australia (yellow, orange, and red contours), the other two bounded by New Zealand (light green contours), comprise the innermost nesting in our region of interest. Closer inspection of the region east of Australia (Fig. 4b) reveals how the currents of interest are connected to the larger flow field. The EAC and ECC are western boundary currents of the innermost nested gyres. The Tasman Front is the southern edge of the innermost gyre bounded by

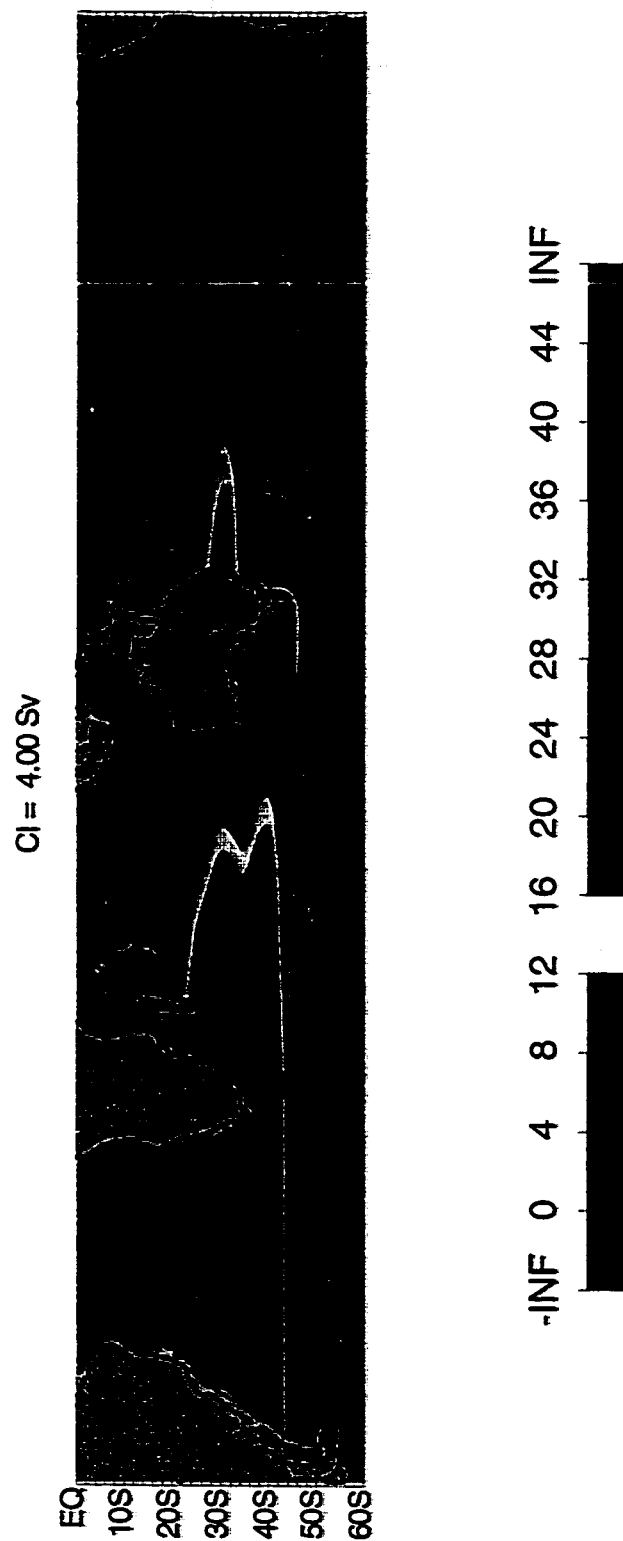


Figure 4a. Mean transport streamfunctions from the $1/8^\circ$ linear 1.5 layer simulation RG1 for the Southern Hemisphere depicting the interbasin supergyre and the nested intrabasin gyres. Note the location of the EAC, EAUC, ECC, and Tasman Front. The EAC and ECC separation points agree with observations. The contour interval is 4.0 Sv ($10^6 \text{ m}^3 \text{ s}^{-1}$). Flow proceeds with higher valued streamfunctions to the right. The streamfunctions are filled to ease the identification of separate gyres described in text.

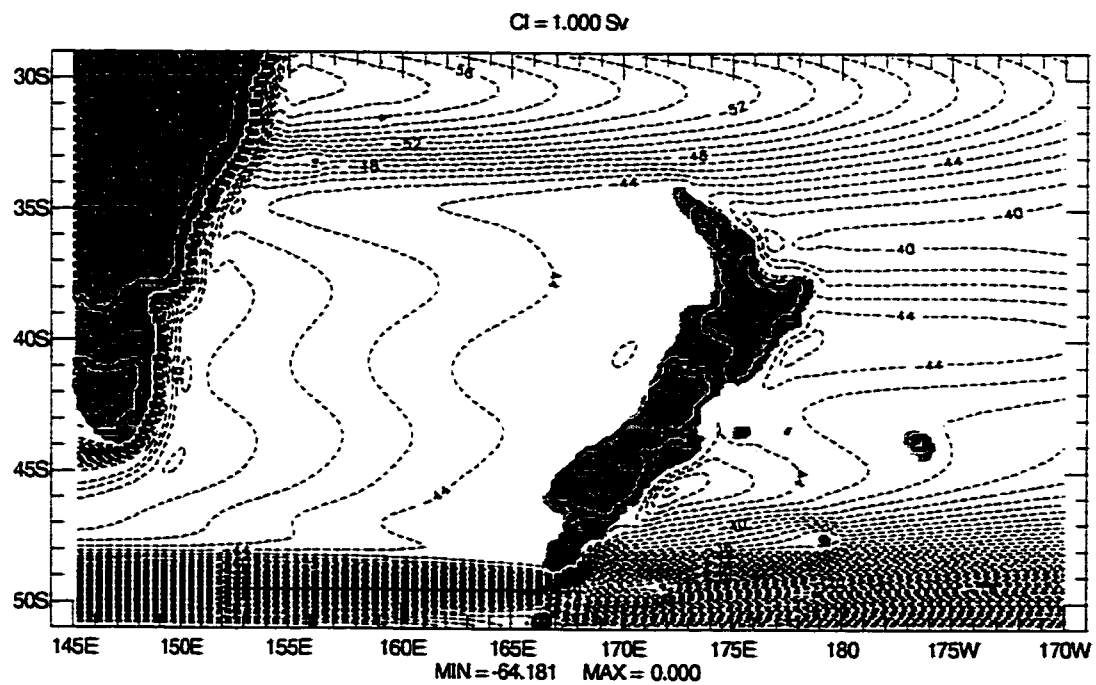


Figure 4b. Mean transport streamfunctions from the $1/8^\circ$ linear 1.5 layer simulation RG1 for the region surrounding New Zealand. Note the incorrect direction of the EAUC and the Southland Current.

Australia. The northern anticyclonic gyre east of New Zealand is bounded on the west by the ECC, but the southern one is unobserved. The southward western boundary current associated with this gyre disagrees with the observed northward Southland Current and its subsequent eastward flow at the Chatham Rise as described by Chiswell (1996), Stramma et al. (1995), and Uddstrom and Oien (1999). Likewise, the simulated EAUC, the western boundary current connecting the two northern inner gyres, flows opposite to the observed direction (northwestward in the linear simulation vs. southeastward observed). The simulated EAC and ECC both separate from the western boundaries at the observed locations (centered near 32°S on the east coast of Australia and near 42°S on the east coast of New Zealand, respectively), while the simulated Tasman Front appears in the correct geographic location.

Although observational values of the transports are sparse, a rudimentary model-data comparison can be made. The simulated linear EAC is 25.9 Sv, which agrees well with observational values. Ridgway and Godfrey (1997) estimated the flow of the EAC relative to 2000 db using steric heights derived from historical hydrography and expendable bathythermograph (XBT) data collected in the region and found that the EAC varies between 27.4 and 36.3 Sv seasonally. Chiswell et al. (1997), using CTD data gathered over five cruises between 1990 and 1994, estimated the geostrophic transport of the EAC relative to 2000 db to be between 22.2 and 42.2 Sv. The simulated linear transport associated with the Tasman Front, 10.6 Sv, also agrees well with observational values. Stanton (1979), using bathythermograph (BT) data, calculated geostrophic volume transport relative to 1000 db to be 7.6 – 8.5 Sv, which was slightly lower than his

previous observations of 9–12 Sv (Stanton, 1976). Andrews et al. (1980), using XBT data, estimated the net zonal transport to be approximately 15 Sv relative to 1300 db. More recent observations yielded integrated volume transports measured at 173°E ranging from –7.1 to 16.5 Sv over a four year time frame (Chiswell et al., 1997). However, the authors hypothesized that the negative transport value in the Tasman Front transport was due to an error in measurement and should not be considered evidence of a westward flow into the Tasman Sea (Chiswell et al., 1997). The simulated transports of RGI for selected sections (gray lines in Fig. 1) along with those from the subsequent simulations are shown in Table 3. As noted, there are some discrepancies between the linear simulation and observations. The simulated linear EAUC (3.1 Sv to the west-north-west) is opposite in direction to observations, which show part of the flow along the Tasman Front continuing along the northeast coast of New Zealand. Heath (1985b) describes an east-south-east flow of 2 – 10 Sv, while other observations (Stanton et al., 1997) describe larger transports of 11 to 34 Sv. The simulated net southward transport through the Tasman Sea (12.1 Sv) is higher than observed values of 7.1 Sv at 44°S (Ridgway and Godfrey, 1997) and 6.3 – 9.2 Sv at 43°S (Chiswell et al., 1997). The simulated boundary current along the eastern coast of South Island (–3.0 Sv) flows counter to observations of 3.5 Sv (Heath, 1972) and 10.4 Sv (Chiswell, 1996). These discrepancies suggest that linear dynamics are unable to explain some aspects of the flow field, and more complicated processes are necessary to fully describe this region.

Since the linear model does agree with observed locations of EAC separation, we are able to use linear theory to investigate the baseline dynamics behind this

Table 3. Mean Transport from Selected Sections

Experiment	Pacific Ocean ² at 32°S	Pacific Ocean ² at 39°S	Tasman Sea ³	East Australian Current ⁴	Tasman Front ⁵	EAUC (after separation) ⁶	EAUC (before separation) ⁷	East Cape Current ⁸	Southland Current ⁹
RG1	-16.5	25.5	-12.1	-25.9	10.6	3.1	-2.5	-2.1	-3.0
RG2	-16.5	-	-11.9	-25.9	13.4	-	-	-	-
RG3	-16.8	25.3	-7.6	-25.5	14.6	-0.9	-6.5	-6.5	-4.0
RG4	0.0	25.5	-28.7	-42.4	10.5	3.2	-2.4	-2.1	-3.0
FB	-11.7	21.1	5.3	-26.7	31.6	-13.5	-24.6	-14.9	-4.3
RB8a	-13.6	17.1	0.1	-27.2	23.1	-3.8	-31.0	-11.7	20.2
RB8b	-14.7	-	0.7	-26.1	16.4	-	-	-	-
RB16	-12.2	14.1	6.4	-28.0	27.5	-8.5	-36.8	-15.9	18.3
Observations ¹⁰	-5 -- -26	-	-6.3 -- -9.2	-22.2 -- -42.2	7.6 -- 16.5	-2 -- -11	-10 -- -34	-22	3.5 -- 10.4

Values are given in Sverdrups ($10^6 \text{ m}^3 \text{ s}^{-1}$). Negative means west or south. Positive means east or north. All transports of multi-layered simulations are for the top five layers of the simulation, corresponding to the simulated thermocline. These transport sections are shown in Fig. 1 as gray lines.

Table 3 – continued.

- 1 This transport corresponds to the basinwide equatorward movement out of the region of interest. Since the model excludes transport through the Bering Sea, this value can be used as a proxy for the IPT and compared to observations to validate the model.
- 2 This transport corresponds to the equatorward movement of the south Pacific subtropical gyre. For mass balance Pacific Ocean at 32°S + Tasman Sea + Pacific Ocean at 39°S + EAUC (after separation) must equal the vertical mixing between layers 5 and 6 over the latitude band separating the IPT and the other cross sections (which is very small).
- 3 Transport through the Tasman Sea at 44°S
- 4 Meridional transport between the coast of Australia and 154.8°E at 29°S.
- 5 Zonal transport between 31°S and 36°S at 168.2°E
- 6 Alongshore transport between coast and 178.9°E, 36.0°S. Positive corresponds to northwestward, negative to southeastward.
- 7 Alongshore transport between coast and 176.5°E, 33.6°S. Positive corresponds to northwestward, negative to southeastward.
- 8 Alongshore transport between coast and 178.6°E and 40.0°S. Positive corresponds to northward, negative to southward.
- 9 Alongshore transport between coast and 173.8°E and 46.5°S. Positive corresponds to northeastward, negative to southwestward.
- 10 Observations from all studies mentioned in text. Note the observed transport at 32°S entries are actually observations of IPT transport.

phenomenon. The unique position of New Zealand (directly in the path of a separating western boundary current) has fueled speculation concerning the role of the island in the separation of the EAC. Two main theories concerning its role focus on two different aspects of the flow. The first states that New Zealand blocks the westward propagating Rossby waves south of 34°S causing the EAC to separate at this latitude instead of much farther south (Warren, 1970). The second states that the coastline geometry of Australia (i.e. the bend in the coastline at Sugarloaf Point) causes the separation (Godfrey et al., 1980; Ou and De Ruijter, 1986) and the location of New Zealand is unimportant.

Transport streamfunctions from a simulation (Fig. 5) where New Zealand has been removed (RG2) demonstrate that the removal of the island does not alter the separation latitude of the EAC. In a linear simulation, complete separation of a western boundary current from the coast occurs at the latitude of the zero wind stress curl line integrated from the eastern boundary to the western boundary. This separation can be complicated by land masses that partially block gyres and by gradients in the wind stress that force zonal currents but do not act as outer gyre boundaries. There is no zero integrated wind stress curl line (Fig. 6) that would cause the EAC to completely separate from the coast of Australia. A gradient, however, exists in the zonally integrated wind stress curl (shown as white line in Fig. 6) that causes a zonal flow eastward at 34°S providing a southern boundary to a nested gyre within a larger gyre. The separation points of the EAUC (37°S) and the ECC (42°S) also correspond to gradients in the zonally integrated wind stress curl. Zonal currents at these latitudes are seen at the same latitudes even after New Zealand has been removed (Fig. 5). The gradients in zonally

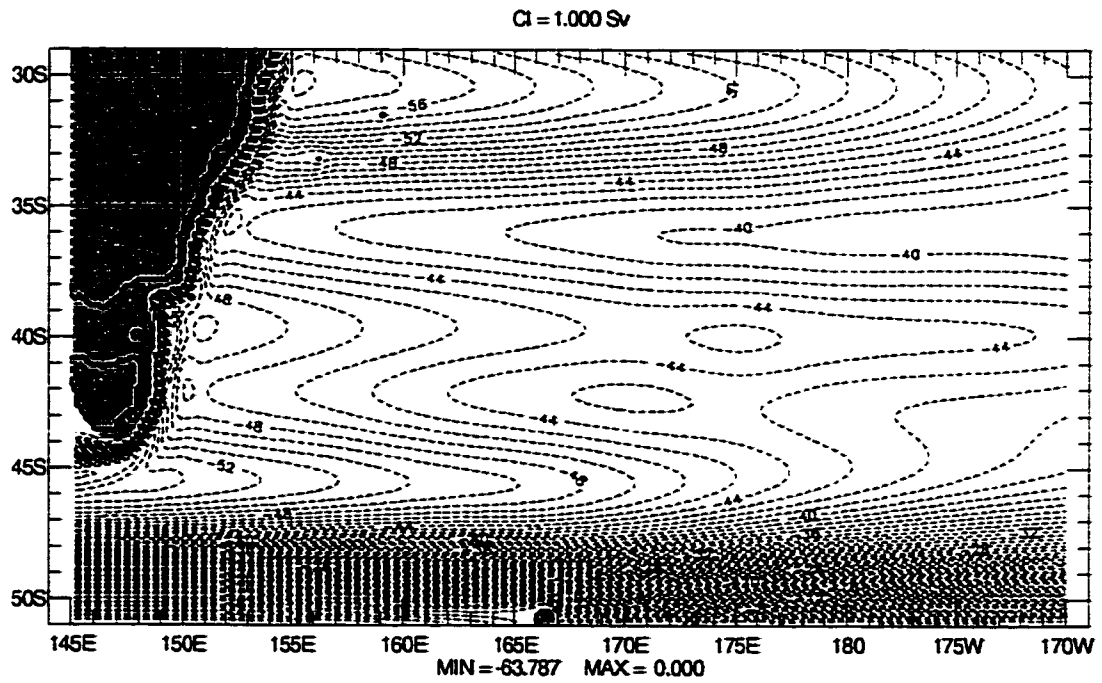


Figure 5. Mean transport streamfunctions from the $1/8^\circ$ linear 1.5 layer simulation RG2 with New Zealand removed from the flow field. Note that the EAC separation point is still between 30° and 34° S, in agreement with observations and RG1.

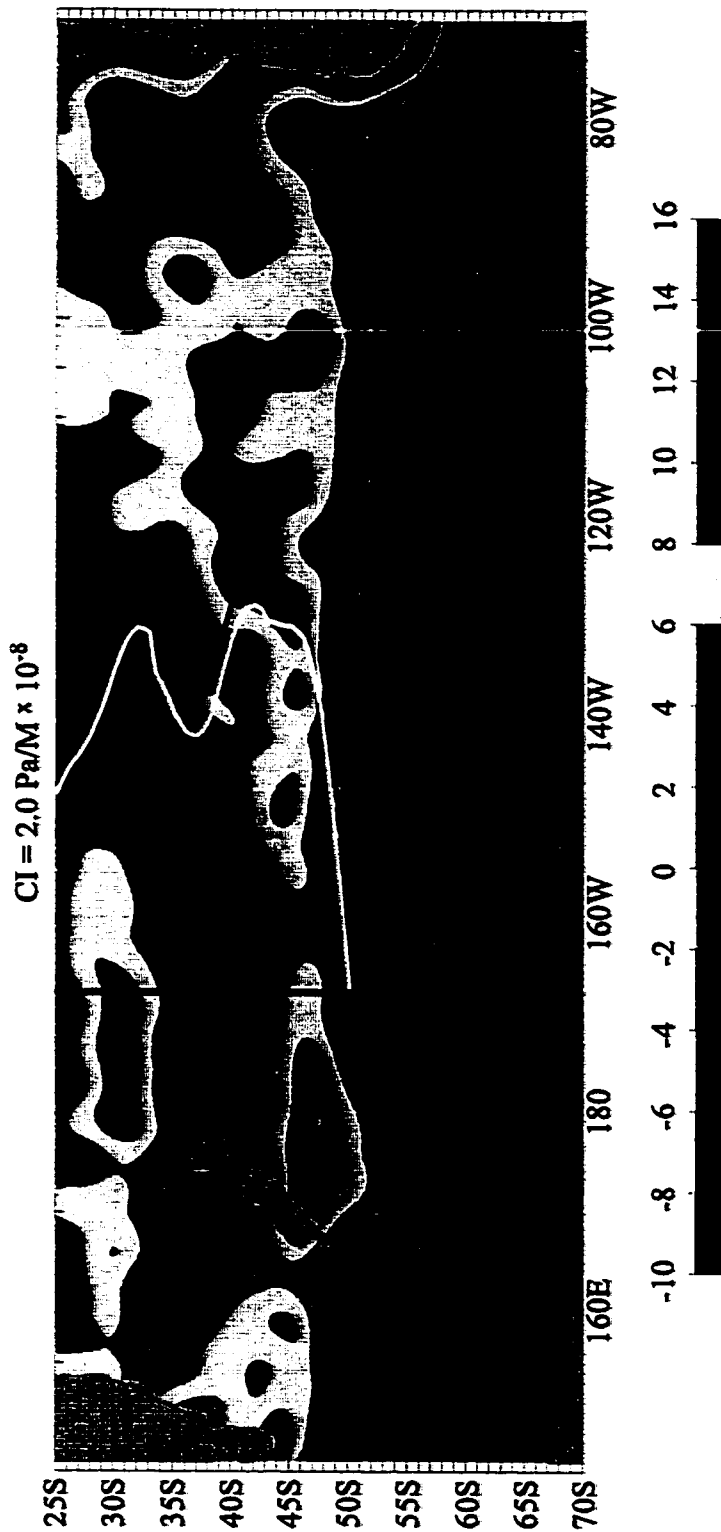


Figure 6. Annual mean wind stress curl field derived from Hellerman and Rosenstein (1983). Note the large negative curl in the Antarctic region. The white line represents the zonal wind stress curl integrated from the western coast of South America to the eastern coast of Australia or New Zealand. The gray line represents the zonal wind stress curl integrated from the western coast of South America to the eastern coast of Australia, assuming New Zealand has been removed. The black vertical line represents the zero of the integrated wind stress curl. Note that there is no zero windstress curl line at the latitude of the EAC separation.

integrated wind stress curl are still apparent when the winds are integrated from the western coast of South America to the coast of Australia (gray line in Fig. 6). The partial separation of the EAC can be explained by the wind field with New Zealand present or removed, suggesting that New Zealand does not affect the separation point, aside from the island's effect on the wind field itself.

The reversed direction of the EAUC in the linear simulation RGI can be linked to the higher than observed southward transport through the Tasman Sea. The simulated transport is slightly less than that of the linear model of Godfrey (1989), discussed in Ridgway and Godfrey (1994) (12.1 Sv vs. 15 Sv) but still larger than observations. Analysis of the mass balance of this region shows four pathways available for water to enter or exit the region (Fig. 7): the Tasman Sea, the basinwide transport at 32°S, the transport of the South Pacific subtropical gyre east of New Zealand at 39°S, and the western boundary current along New Zealand (i.e. the EAUC). Since net vertical mixing is small compared to the horizontal transports in this latitude band (32°S to 39°S, marked in Fig. 7), the residual of the mass balance of the transports along the three other pathways determines the direction of the EAUC. If the non-EAUC transport into the region (equatorward flow of the South Pacific subtropical gyre at 39°S) is larger than that out of the region (transport at 32°S + Tasman Sea) then the EAUC must flow southeastward (out of the latitude band) to achieve mass balance. If the transport into the region is less than the transport out, the EAUC must be northwestward (into the latitude band). From Table 3, we can see that, if the EAUC is to flow southeastward in RGI, the

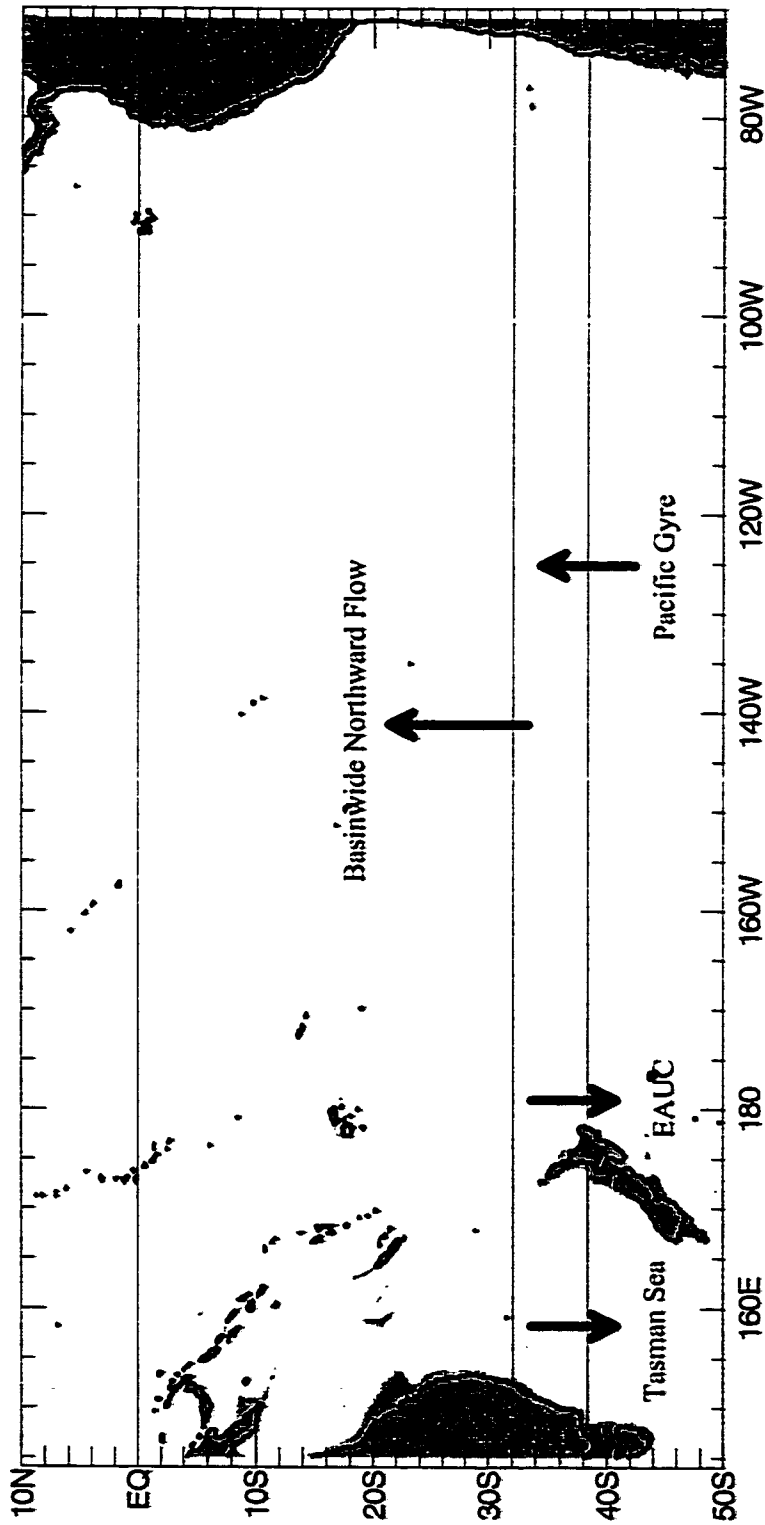


Figure 7. Illustration of the mass balance of the region from 32°S to 39°S. Since the North Pacific Ocean model has no transport through the Bering Sea, all of the mean net northward transport across the basin north of 32°S must leave the basin through the IPT in a fully spun up simulation.

southward flow through the Tasman Sea must be less than 9.0 Sv ($25.5[\text{transport at } 39^\circ\text{S}] - 16.5[\text{transport at } 32^\circ\text{S}] = 9.0 \text{ Sv}$). Since the simulated flow through the Tasman Sea in RG1 is larger than this value and the observed value, the simulated EAUC flows in the incorrect direction.

Decreasing the flow through the Tasman Sea in the linear simulation to agree with observed values by increasing the local horizontal friction within the Tasman Sea (RG3) (Fig. 8a), produces an EAUC that flows southeastward connecting the two northern inner gyres seen in Figure 4b. The EAUC can be divided into two flow regimes: (1) *before separation* and (2) *after separation*. *Before separation* corresponds to the alongshore transport passing between the northern tip of New Zealand and 176.5°E , 33.6°S . *After separation* corresponds to the alongshore transport passing between the eastern coast of New Zealand and 178.9°E , 36.0°S , after the majority of the EAUC has turned offshore leaving a much weaker flow attached to the coast (see Fig. 1). The linear EAUC from RG3 has a magnitude of 6.5 Sv *before separation* and 0.9 Sv *after separation*, in agreement with the lower bound of observations. The weaker attached flow continues around the East Cape and joins with a westward onshore flow to produce an ECC of 6.5 Sv. The separation point of the EAUC agrees well with observations and is situated at a sharp gradient in the zonally integrated wind stress curl (Fig. 6).

Since the model domain has no transport through the Bering Sea, all of the northward transport across the basin at 32°S must leave the basin through the IPT. Since estimates of the transport through the IPT vary from $<5 \text{ Sv}$ to $18.6 \pm 7 \text{ Sv}$ (Godfrey, 1996), an incorrect choice of the simulated IPT might conceivably affect the mass balance of our

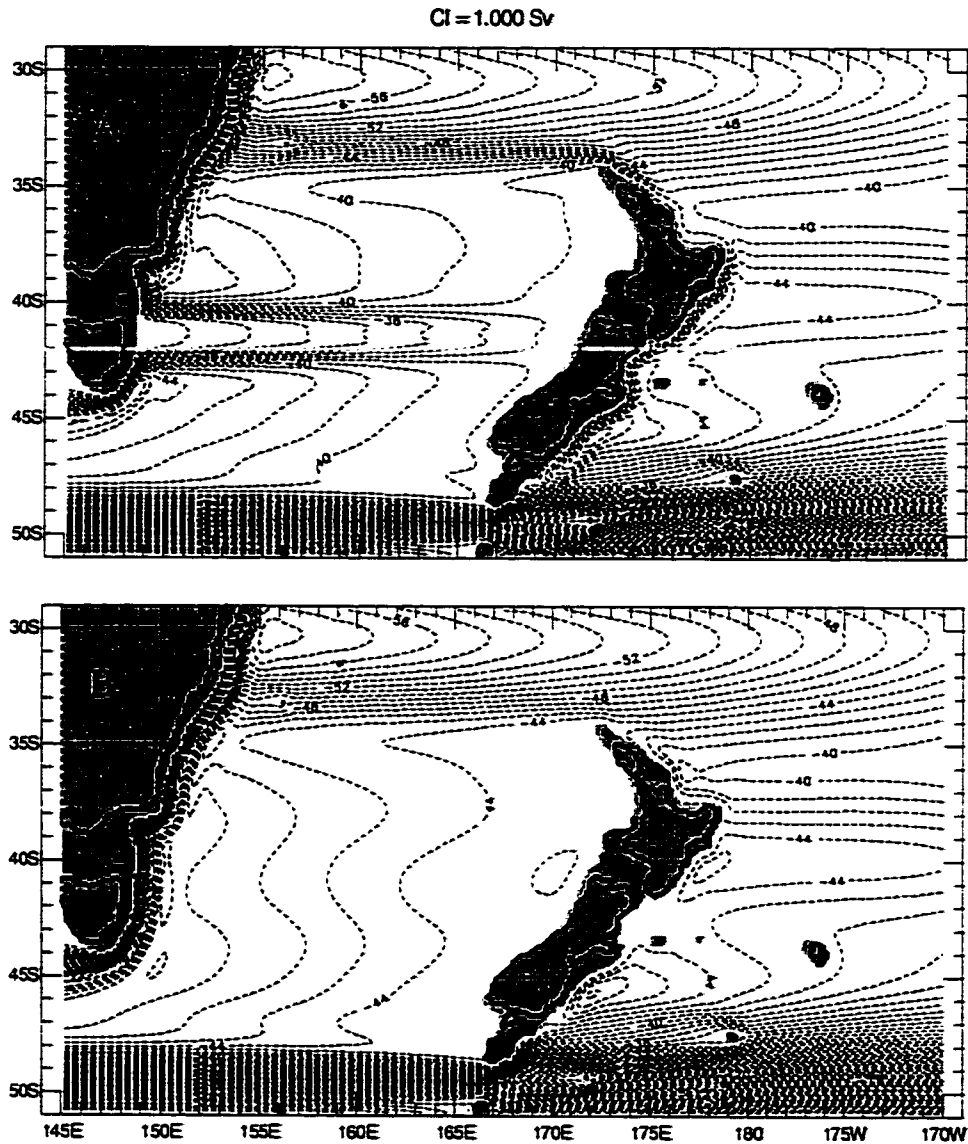


Figure 8. Mean transport streamfunctions from the $1/8^\circ$ linear 1.5 layer simulations of (a) RG3 and (b) RG4. RG3 has the increased friction in the Tasman Sea. Note the correct flow direction of the EAUC and correct separation points of all currents, except for the unobserved southward flow along the east coast of South Island. The small perturbation in the southern Tasman Sea is an effect of the friction patch and not of any changes in the winds. RG4 has the Indo-Pacific Throughflow closed off. Note the increased transport through the Tasman Sea and the continued northwestward direction of the EAUC.

region. However, varying the magnitude of the IPT and therefore the transport through 32°S has no effect on the EAUC or ECC. Shutting off the flow through the IPT (RG4) does not change the total flow out of the region (Fig. 8b). It merely diverts the flow through the Tasman Sea via an increased EAC (42.4 Sv vs. 25.9 Sv) with no change in the EAUC or the ECC.

The failure of the linear model to produce the correct direction of the EAUC may be in part due to its inability to simulate isopycnal outcropping, which is discussed in the next section. Although linear dynamics can be used to explain the direction and separation of most of the major currents in this area, it fails to reproduce the complicated flow field to the north of New Zealand, the meanders in the Tasman Front, or the observed direction of the Southland Current. It also must be modified to reproduce the correct direction of the EAUC. More complex dynamics are needed to fully describe this area.

b. Nonlinear Dynamics: Flat Bottom and Reduced Gravity Cases

A six-layer nonlinear 1/8° simulation with a flat bottom (FB) driven by HR winds is employed to incorporate nonlinear dynamics and vertical structure to the simulated flow field. Simulated four year mean surface currents (Fig. 9a) reveal flow meanders and eddies, including the relatively persistent eddies observed by Roemmich and Sutton (1998) north and east of New Zealand. The simulated surface currents reveal an

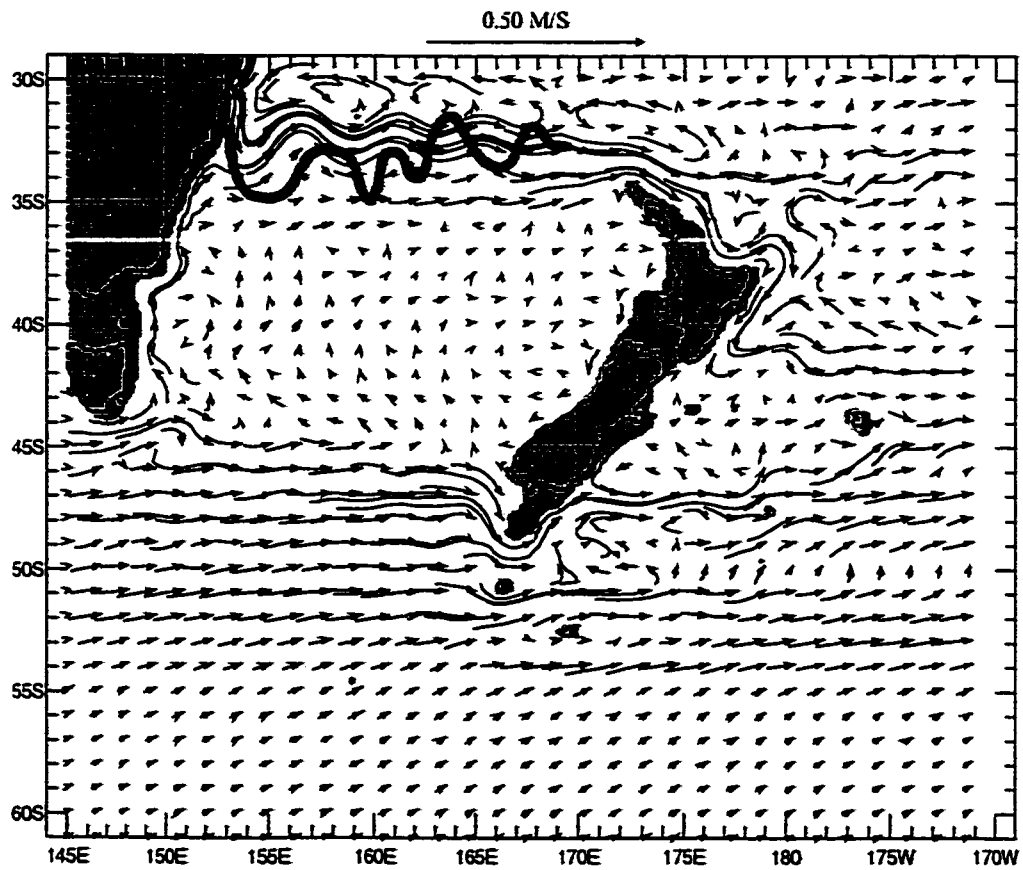


Figure 9a. Mean surface currents from the $1/8^\circ$ nonlinear six-layer simulation with a flat bottom, FB. The most probable Tasman Front pathway described in Figure 2 is represented by the gray line. Note the mean meanders in the Tasman Front in FB and the eddies north of New Zealand. The simulated meanders show poor agreement in phase with those observed and decrease in amplitude eastward along the Tasman Front contrary to observations. The ECC separates just north of the Chatham Rise as observed, even though there is no bottom topography to guide the flow.

elongated eddy corresponding to the observed NCE and eddies to the north and east of East Cape corresponding to the ECE and WE. The simulated mean meanders in the Tasman Front have wavelengths (410 km) that agree with the observational values of 300 – 500 km (Stanton, 1979; Andrews et al., 1980; and Mulhearn, 1987), but their amplitude and phase do not.

Several authors have attempted to explain the meanders within the Tasman Front. Stanton (1976) postulated that the wavelengths of the meanders over the Norfolk Ridge might correspond to those of a westward propagating Rossby wave, although he did note that there was not sufficient data for a definite conclusion. Andrews et al. (1980) found that the wavelengths required for a Rossby wave with the observed propagation speed of the meanders were much larger than those observed and suggested that nonlinearities were affecting the flow. Both Stanton (1979, 1981) and Mulhearn (1987) mention the possibility of topographic influences on the meanders, although Mulhearn (1987) notes that he was unable to find a clear indication of the mechanism.

Other authors have examined the dynamics behind stationary meanders associated with a separating western boundary current using both numerical and analytical arguments. Ou and De Ruijter (1986) argued that the separation point and behavior afterward of a western boundary current was a function of the transport within the current and the shape of the coastline. When the coastline slopes away from the separation point (similar to the orientation of the Australian coastline), the boundary current continues southward after separation and then retroflects to return to the latitude of initial

separation, forming meanders that are then governed by conservation of absolute vorticity. Campos and Olson (1991) were able to produce mean meanders in a zonal separation jet in both barotropic and baroclinic nonlinear general circulation models. The meanders produced in the baroclinic model were subject to some propagation and temporal growth, producing eddies at regular time intervals. Da Silveira et al. (1999) using a $1\frac{1}{2}$ layer model were able to reproduce a quasi-stationary wave pattern formed by the convergence of two boundary currents. Both Campos and Olson (1991) and Da Silveira et al. (1999) also found that the separation point and amplitude of the meanders were greatly influenced by the shape of the coastline. Holland (1978) using a quasi-geostrophic two-layer model with a straight western boundary did not reproduce meanders, demonstrating that some sort of asymmetry such as sloped coastline is required to produce meanders.

The simulated meanders of the flat bottom model (Fig. 9a) are approximately stationary, with the first meander extending southward and retroflecting northward, consistent with Ou and De Ruijter (1986), Campos and Olson (1991), and Da Silveira et al. (1999). As mentioned earlier, the wavelengths correspond to the most probable path discussed by Mulhearn (1987) and Stanton (1979) but the amplitudes and phases do not. The amplitudes of the simulated meanders decrease as the flow proceeds away from the western boundary as would be expected in an inertial flow, but in direct disagreement with observations. The wavelengths of both simulated (~ 410 km) and observed meanders (300 – 500 km) are less than those of a stationary Rossby wave pattern (Andrews et al., 1980) or constant absolute vorticity (CAV) trajectory (Haltiner and

Martin, 1957). For trajectories with small amplitude meanders, stationary wavelengths in CAV trajectories are related to the characteristic velocity of the flow by

$$\lambda = 2\pi \sqrt{\frac{v_c}{\beta}} \quad (4)$$

where

v_c is the characteristic velocity at the core of the current and

λ is the stationary wavelength.

Since the simulated meander wavelengths are less than the stationary wavelength (600 km) predicted from the depth averaged velocity of the top five layers of FB (0.17 m/s), the simulated meanders should propagate eastward to be consistent with CAV theory, not remain stationary as observed. When the bottom layer is constrained to be at rest, creating a 5.5 layer reduced gravity simulation (RG5.5, Fig. 9b), the resulting simulated meanders are no longer stationary, but propagate westward. This propagation obscures the presence of wavelengths in the mean and shows instead a flow field with irregularly sized meanders. The majority of the simulated meanders from RG5.5 (460 km – 750 km, obtained from snapshots of the simulation) are larger than the stationary wavelength (530 km) corresponding to the simulated core velocity (0.15 m/s), so their westward propagation is consistent with CAV theory. Interestingly, the simulated EAC in RG5.5 separates farther south and retroflects northward to a larger degree than FB. The propagation in RG5.5 and the stationarity in FB are clearly seen in a longitude time plot of sea surface height deviation (Fig. 10). These differences suggest that, while the

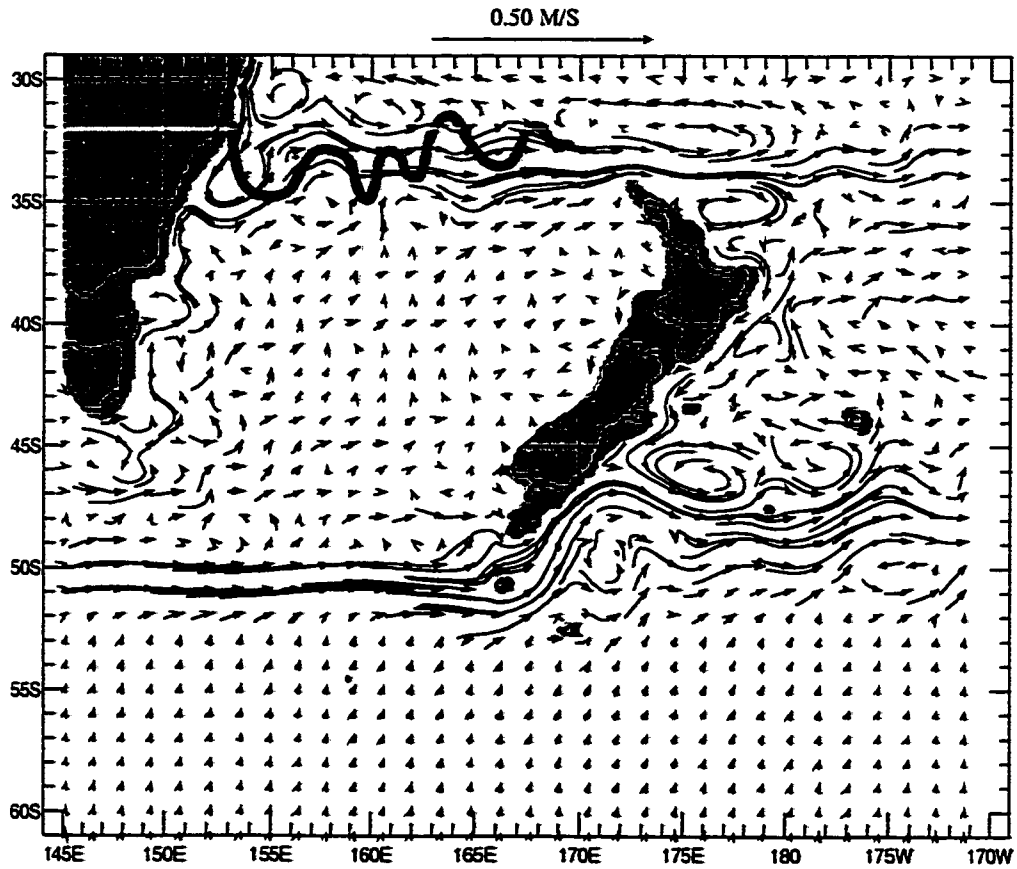


Figure 9b. Mean surface currents from the $1/8^\circ$ nonlinear 5.5 layer reduced gravity simulation, RG5.5. The most probable Tasman Front pathway described in Figure 2 is represented by the gray line. Note the lack of regular meanders, such as found in FB, in the Tasman Front.

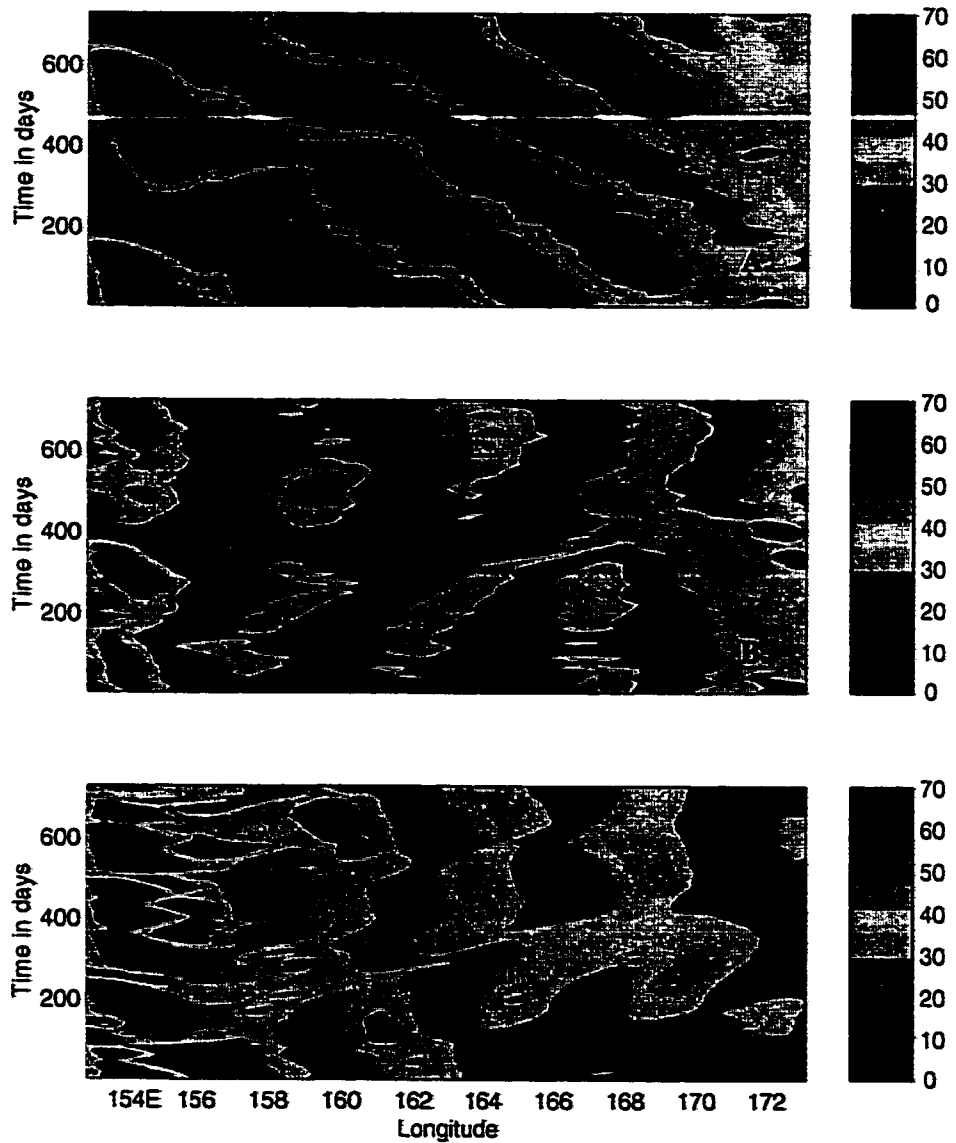


Figure 10. Longitude-time plots of sea surface height deviations at 33°S from (a) RG5.5, (b) FB, and (c) RB8a. Note the westward propagation of the signal in the reduced gravity simulation and the stationarity of the two finite depth simulations.

meanders within RG5.5 can be explained by CAV theory, other dynamics must be present in FB.

Two types of instabilities can result in meanders in a zonal flow: barotropic and baroclinic instabilities. Both instabilities are due to disturbances that are introduced to the flow field and then proceed to grow, drawing energy from the mean flow field. Barotropic instabilities are due to disturbances whose energy is supplied by the horizontal shear flow of the current. Baroclinic instabilities are due to disturbances whose energy is supplied by the available potential energy from the sloping interfaces of isopycnals. In a baroclinic zonal jet with latitudinal dependence both instabilities may be present. To determine the wavelengths of disturbances generated from a combination of these two mechanisms is exceeding difficult, if not impossible, for an arbitrary baroclinic flow. Instead we will determine the susceptibility of the flow field to the two instabilities separately, realizing that the actual flow field is most probably a combination of both instabilities.

We first investigate the susceptibility of the flow field to baroclinic instabilities. The inclusion of the bottom boundary and, therefore the barotropic mode, allows the formation of baroclinic instabilities involving the barotropic mode within the model. The appearance in FB of stationary meanders whose wavelengths are shorter than those predicted by CAV theory indicates that instabilities are responsible for shortening their wavelengths via vortex stretching and stopping their propagation. Surface layer pressures overlaid on abyssal layer pressures (Fig. 11) show a phase difference between the two layers in the vicinity of the Tasman Front, the EAC, and the ECC, which is a classic

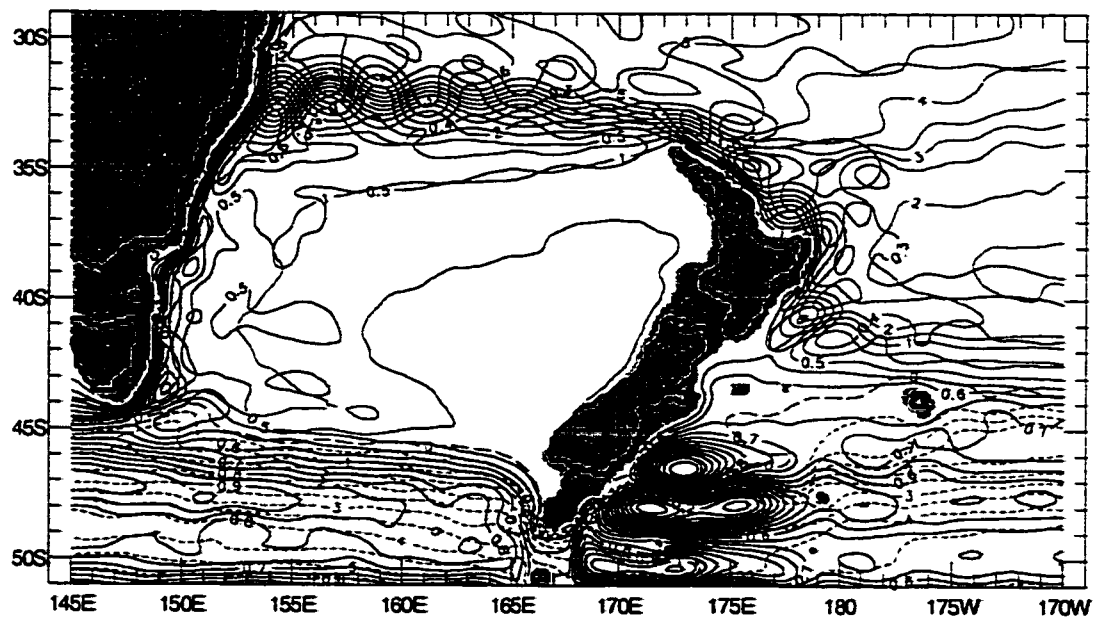


Figure 11. Mean surface layer pressures (red) of FB overlaid on abyssal layer pressures (black). Note the phase lag and difference in flow direction between the two layers.

signature of baroclinic instability. Further evidence of baroclinic instabilities can be obtained by inspection of eddies formed from the meanders within the Tasman Front. The beta Rossby number of an eddy, $R_b = v/\beta r^2$, is the ratio of relative to planetary vorticity advection (where v = maximum swirl velocity within the eddy and r = mean radius of the eddy) and can be used to determine the physical processes responsible for generation of the eddy. R_b of order 1 suggests that the eddy was formed by barotropic instabilities involving the first baroclinic mode, while an R_b of order 10 suggests that it was formed by baroclinic instabilities involving the barotropic mode (McWilliams and Flierl, 1979; Hurlburt and Thompson, 1982, 1984; Murphy et al., 1999). Eddies formed during the last two years of the simulation (not shown) are characterized by $v \approx 35$ cm/s and $r \approx 47$ km, resulting in $R_b \approx 7.9$, suggesting that the eddies and, therefore, the meanders were formed by baroclinic instabilities.

Baroclinic instabilities may also be identified by the wavelength of the meanders within the flow field, since the growth rates of disturbances due to baroclinic instabilities are functions of the disturbance wavelength. Although the flow field is constantly exposed to disturbances of different wavelengths, it is predisposed to the propagation and growth of a limited range of wavelengths. Within a long-term mean of the flow field, those stationary wavelengths with large growth rates will dominate. Mean meanders produced by baroclinic instabilities will most likely exhibit this favored wavelength.

Phillips (1954) first introduced a linear stability analysis that provides the propagation and growth rate of a baroclinic disturbance as a function of wave number for a zonal, two-layer system assuming a flat bottom and the absence of friction. Haidvogel

and Holland (1978) showed that this instability analysis can lead to meaningful results such as wave number and growth rates of the dominant waves. Talley (1983) used the two-layer analysis to examine radiating instabilities in baroclinic jets. The instability analysis is based on the solution of the layered vorticity equations into which a disturbance has been introduced. A disturbance $\varphi_n(x, y, t)$ to the zonal stream function, $\psi_n(y)$, is introduced into the vorticity equation, so that the new stream function is

$$\Psi_n(x, y, t) = \psi_n(y) + \varphi_n(x, y, t) \quad (5)$$

where

$$\varphi_n(x, y, t) = \text{Re}[\phi_n(y)e^{ik(x-ct)}] \quad (6)$$

$n = 1..N$ (corresponding to each layer).

The equations are then solved making several simplifying assumptions and an equation for kc in equation (6) is formulated. The growth rate of the disturbance is $\text{Im}(kc)$, while the propagation rate of the disturbance is $\text{Re}(kc)$. When the imaginary component is negative, the disturbance grows exponentially with time and is considered a baroclinic instability. The solution of the linear system of equations involving equation (6) reveals that the phase speed, c , is an eigen value, which may be complex. Since complex eigen values of systems of equations appear as pairs of complex conjugates, any appearance of complex eigen values guarantees baroclinic instability. Obviously, the growing disturbance will reach a point where the linear analysis is no longer valid and nonlinear dynamics prevail. The initial growth rate, however, determined by the linear analysis can

still be used to investigate which wavelengths will dominate the growth of the disturbance.

A full discussion of the development of the six-layer baroclinic instability analysis neglecting bottom topography, friction, nonlinearities, and dependence of the layer velocities on latitude is included in Appendix B. The six-layer system does involve a much more complicated reaction to disturbances than the two-layer system, since the multiple baroclinic modes in the system can cause non-unique growth and propagation rates for each wave number. The velocity profile associated with the Tasman Front is dominated by the barotropic and first baroclinic modes (as seen when the velocity profile (Fig. 12a) is separated into its natural modes (Fig. 12b) using the method developed by Lighthill (1969)). Although the two barotropic and first baroclinic modes dominate the flow field, the growing disturbances are not confined to these modes.

Three distinct disturbance regimes are present in the system. The imaginary components of the phase speed, c_i , of initial disturbances as functions of non-dimensionalized wave number ($K=kL$, where $L = 100$ km) (Fig. 13a) show two regimes corresponding to exponential growth rates (blue and red lines) and one regime corresponding to a stable but propagating disturbance (green line). The largest peak (blue line) corresponds well with c_i as a function of wave number for a two-layer system whose internal radius of deformation equals the first baroclinic radius of deformation of FB. However, the presence of the second regime demonstrates that the system has significant potential for growing disturbances related to other modes. The mean wavelength of the Tasman Front from FB is 410 km whose wave number is $K = 1.53$ ($K^2 = 2.35$). This wave

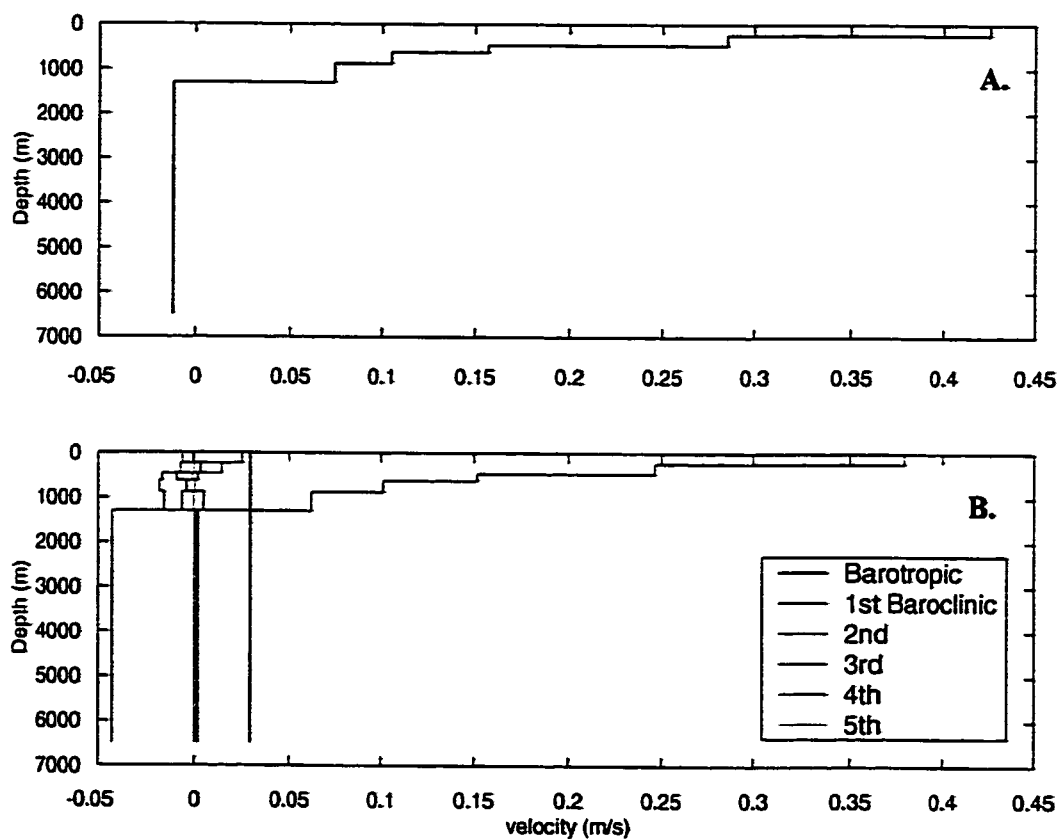


Figure 12. a) Velocity within the simulated Tasman Front (FB) as a function of depth. b) Velocity of FB separated into the barotropic mode and five baroclinic modes. Note the barotropic and first baroclinic modes dominate the velocity field.

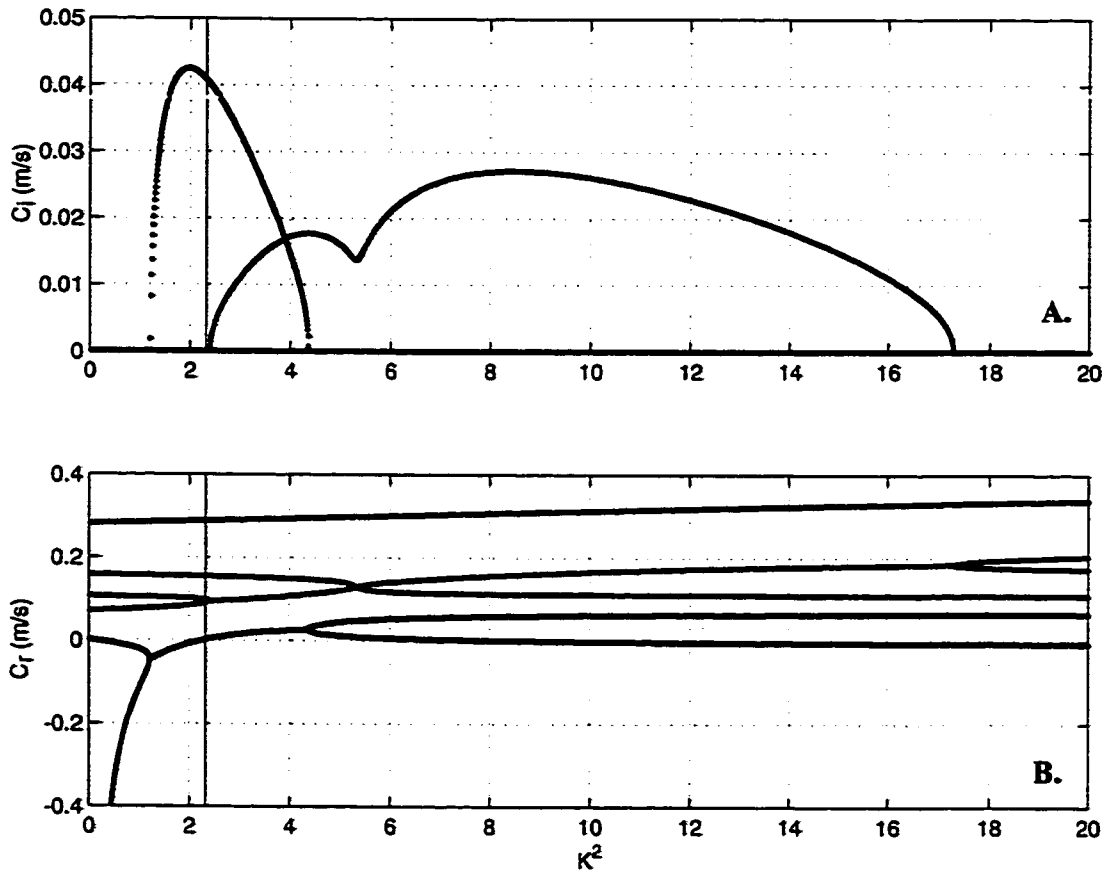


Figure 13. a) Imaginary component of phase speed of the disturbance as a function of wave number for FB. The vertical line at approximately $K^2 = 2.4$ corresponds to the simulated meanders. b) Real component of phase speed of the disturbance as a function of wave number for FB. The three different disturbance regimes are represented by different colors. Note that the wavelength of the observed meanders corresponds to that of a stationary disturbance.

number corresponds to a stationary disturbance with a large growth rate, as can be seen from the real components of the phase speed, c_r , of the disturbances as functions of wave number (Fig. 13b). The other unstable regime (red line) is not associated with stationary disturbances, so meanders with wave numbers corresponding to this regime are unobserved in a long term mean. As expected, the mean wavelength corresponds well with the stationary disturbances within the longitude-time plot (Fig. 10). Although there is propagation evident, the flow is dominated by the stationary meanders whose wavelengths correspond to those created by baroclinic instabilities.

The large horizontal shear due to the zonal surface jet associated with the Tasman Front provides an opportunity for barotropic instabilities (Fig. 14). Again assuming zonal flow, the barotropic equivalent of equations (5) and (6) can be inserted into the vorticity equation and the growth rate for instabilities in the barotropic current can be determined. Since the solution of kc for an arbitrary velocity profile is extremely difficult, necessary but not sufficient criteria have been developed (Cushman-Roisin, 1994) to determine the susceptibility of the flow field to barotropic instabilities. A more detailed explanation can be found in Appendix C. A necessary condition for barotropic instability is that the derivative of the absolute vorticity:

$$\frac{d}{dy} \left(f_o + \beta_o y + \frac{d\bar{v}}{dx} - \frac{d\bar{u}}{dy} \right) = \frac{dQ}{dy} \quad (7)$$

must change sign within the confines of the domain. Since the first baroclinic mode contains the largest velocities (Fig. 12b), it is most likely to contain instabilities due to horizontal shear. A somewhat conservative proxy for the first baroclinic mode is the

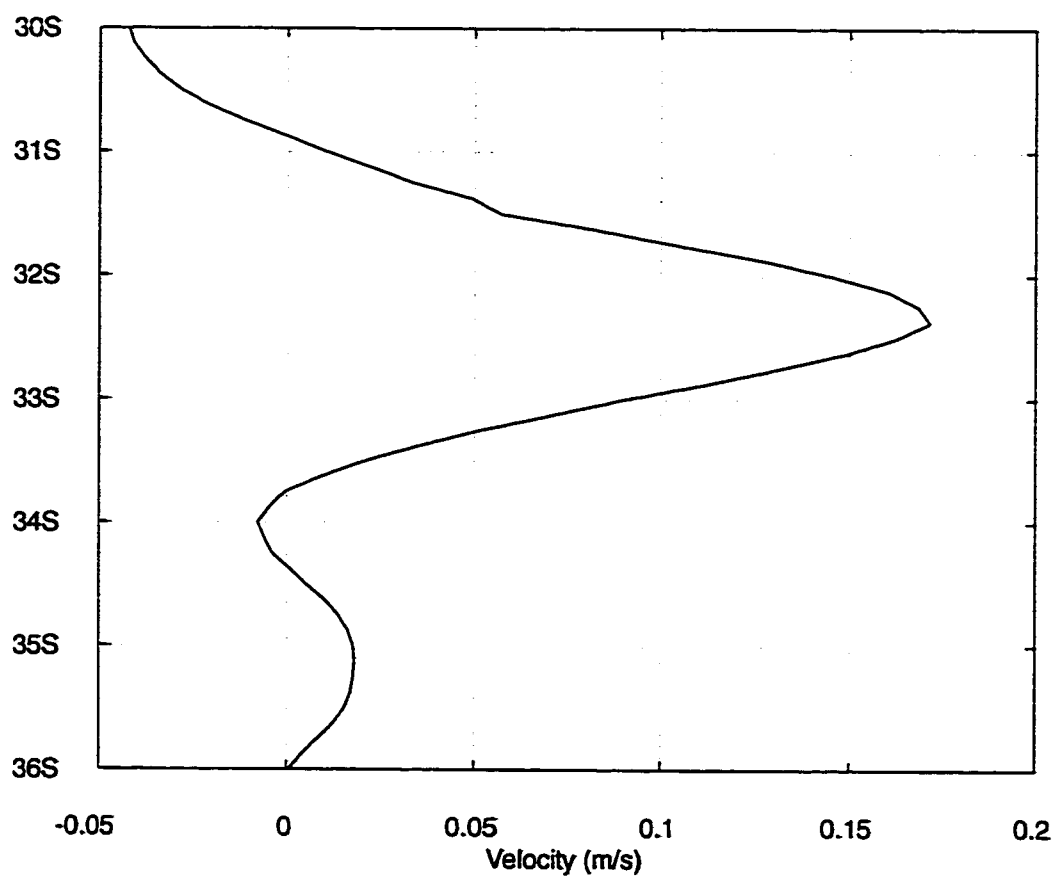


Figure 14. Average velocities of the surface jet associated with the Tasman Front from FB at 165°E. The velocities were depth-averaged through the top five layers.

depth-averaged velocity obtained from the top five layers. A latitude-time plot of the dQ/dy calculated from the depth-averaged velocity of the upper five layers shows that it changes sign at different points in the simulation (Fig. 15). Although the change in sign of equation (7) is not a sufficient condition for barotropic instability, the latitude-time plot suggests that instabilities due to the horizontal shear may modify the wavelengths generated by baroclinic instabilities. Since the beta Rossby number of eddies generated in meanders is 7.9 and the mean simulated wavelengths correspond extremely well to those predicted from only baroclinic instability analysis, the effect of the horizontal shear probably contributes little to the formation of the simulated meanders in the Tasman Front.

The simulated directions and separation points of the investigated currents in FB agree with observations with the exception of the Southland Current. Notably, the EAUC flows in the correct direction, while the ECC separates at 42°S and forms a broad band of eastward flow. However, the simulated flow off the eastern coast of South Island is southward in direct disagreement with observations; the simulated STF flowing south of New Zealand continues on its eastward path at 50°S instead of following the coastline. Also, the flow through the Tasman Sea in FB is mostly confined to the western boundary and travels northward with a transport of 5.3 Sv, not southward as observed by Chiswell et al. (1997) and Ridgway and Godfrey (1997). The northward flow through the Tasman Sea combines with the EAC as it separates from the coast of Australia and flows eastward, producing significantly larger transports along the Tasman Front (31.6 Sv) than the linear simulations or observations. Although some transports greater than 30 Sv have

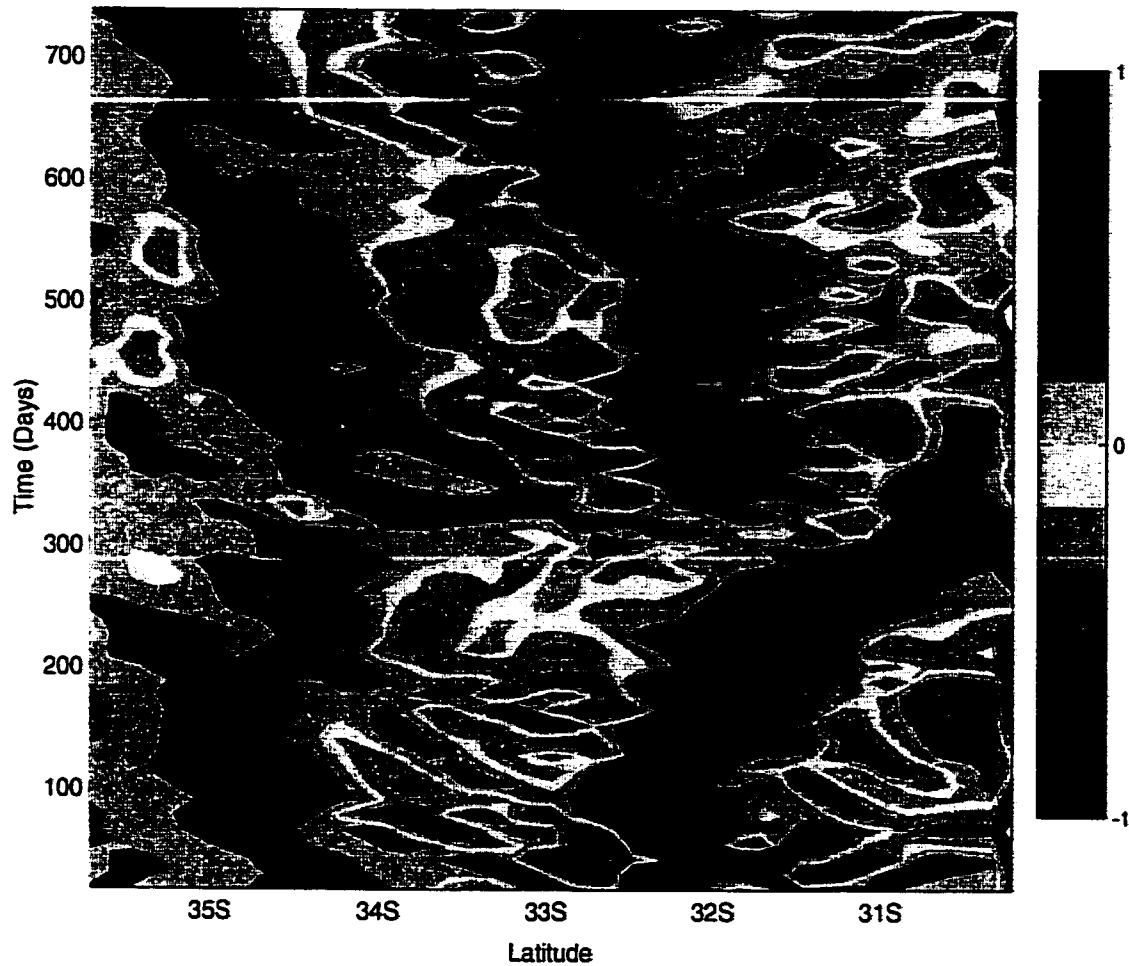


Figure 15. Latitude-time plot of normalized dQ/dy at 165°E from FB where Q is the absolute vorticity calculated from the depth-averaged velocities. Note the change in sign of dQ/dy , a necessary condition for barotropic instabilities.

been observed along the Tasman Front due to recirculation of the flow by eddies, time-averaged transports are much smaller (Stanton, 1981). This exaggerated zonal flow associated with the Tasman Front may be responsible for unrealistically large instabilities.

Two mechanisms may contribute to the simulated northward transport through the Tasman Sea: unrealistically large IPT transport and exaggeration of the effect of isopycnal outcropping in reducing eastward baroclinic transport south of New Zealand. Returning to the linear simulation of the triple nested subtropical gyre system (Fig. 4a), we see that transport within the supergyre (purple to blue-green contours) follows two pathways between the Pacific Ocean and the Indian Ocean: through the IPT (purple, dark blue, and blue contours) and south of Australia (light blue and blue-green contours). Any change in the transport through the IPT directly affects the transport through the other pathway, the Tasman Sea via the western boundary current. An increased IPT would reduce the southward (or increase the northward) transport through the Tasman Sea but have little effect on the EAUC or the ECC.

The introduction of nonlinearities, increased vertical resolution, and isopycnal outcropping significantly alters the nested gyres seen in the linear simulations. Isopycnal outcropping in the Antarctic region in response to the large negative windstress curl (Fig. 6) reduces the transport south of New Zealand and Australia (Fig. 9a). The depths of the mean interfaces south of Australia and New Zealand (Table 4) are at a minimum along the coast of Antarctica, indicating significant outcropping. Within NLOM, an outcropped layer does not result in a zero thickness, but instead a minimum thickness (50 m for layer

1, 40 m for layers 2-5). When all five upper layers in the hydrodynamic model outcrop (as is the case for the majority of the Antarctic region), only the non-steric contribution to the barotropic transport remains, resulting in drastically reduced transport. The mean interface depths at the coast of New Zealand are much shallower than those at the coast of Australia (Table 4) indicating greater outcropping, which allows less transport south of New Zealand than south of Australia and forces transport northward through the Tasman Sea.

Again, returning to the linear simulation of the triple nested subtropical gyre system of the South Pacific (Fig. 4a), we can see the impact of this reduced transport on other current systems. Focusing on the middle-nested gyre (outlined in dark green in Fig. 4a) we see flow associated with this gyre passing south of New Zealand. As this flow is reduced, more of it must pass north of New Zealand, impacting the transport through the Tasman Sea and the current system comprising the Tasman Front, the EAUC, and the ECC. Since in FB the net transport through the Tasman Sea is northward, a portion of the supergyre transport feeding the IPT no longer passes south of New Zealand but instead flows north through the Tasman Sea and along the Tasman Front. To achieve mass balance in the latitudinal band described in Figure 7, the EAUC now flows southeastward along the coast of North Island. The EAUC has a mean magnitude of 24.6 Sv *before separation* and 13.5 Sv *after separation*, whose values are significantly larger than the modified linear case (RG3) although still within the range of observational values.

Table 4. Mean interface depths (m) at land boundaries south of Australia and New Zealand

Experiment	Interface	Antarctica at 167.84°E	New Zealand at 167.84°E	Antarctica at 146.92°E	Australia at 146.92°E
FB	1	51	107	51	212
	2	91	268	91	383
	3	131	515	130	647
	4	170	785	170	951
	5	210	1140	210	1171
RB8a	1	51	157	52	231
	2	92	363	92	375
	3	132	711	132	719
	4	172	1234	172	1143
	5	212	1718	212	1701
RB16	1	52	137	52	227
	2	93	300	93	371
	3	135	679	133	724
	4	176	1143	174	1150
	5	218	1581	214	1676

Note the interface depths at the coast of Australia are greater than those at New Zealand, providing greater transport south of Australia than New Zealand and forcing northward transport through the Tasman Sea. The initial depths of the mean interfaces of RB8a and RB16 are different from those of FB (i.e. interface 5 for FB is 1000 m, while interface 5 for RB8a and RB16 is 1500 m). These differences affect the extent of isopycnal outcropping on the interfaces and, therefore, the available transport south of New Zealand and Australia.

Clearly the model overestimates the effect of isopycnal outcropping in this region but does reproduce the correct direction of the EAUC, suggesting that the dynamics of isopycnal outcropping, if not the magnitude of its simulated effect, are correct. The exaggerated effect of this outcropping on the transport of ACC has been noted earlier. Shriver and Hurlburt (1997) using a lower resolution version of this model found that the simulated transport of the ACC through the Drake Passage was much less than observed values and attributed this difference to the effect of the modeled isopycnal outcropping.

The linear model RG1 does not reproduce isopycnal outcropping and therefore must be modified to reproduce the reduced flow (RG3) through the Tasman Sea and the observed direction of the EAUC. A model that incorporates isopycnal outcropping (FB) does reproduce the observed direction of the EAUC, although the exaggeration of this effect causes unrealistically large transports associated with the Tasman Front. The flat bottom simulation also produces meanders whose wavelengths agree with observations revealing the probable presence of mixed barotropic/baroclinic instabilities. The simulation fails, however, to produce Tasman Front meanders whose phases and amplitudes agree with observations or a realistic Southland Current. These failures lead to the incorporation of the next step in realism, the inclusion of bottom topography.

c. *Nonlinear Dynamics: Realistic Bottom Topography Case*

A six-layer nonlinear $1/8^\circ$ simulation with realistic bottom topography (RB8a) is used to investigate the role of upper ocean - topographic coupling in this region. Four year mean surface currents superimposed on bottom topography (Fig. 16) show that the simulation reproduces stationary meanders (Fig. 10) in the eastern portion of the Tasman Front (Meanders E, F, and G, labeled in Fig. 2) whose phase more closely agrees with observations, revealing the importance of upper ocean - topographic coupling. The simulated EAC separates farther south than FB (35°S vs. 32°S) and creates a large retroflection similar to RG5.5. RB8a also reproduces all three quasi-stationary eddies and the low observed by Roemmich and Sutton (1998) north and east of North Island. In RB8a, the simulated surface ECC separates from the coast of New Zealand and flows eastward south of the Chatham Rise rather than north of the rise as seen in observations and the other simulations. A summation of the 5 top layers (not shown) shows a zonal current at the observed latitude of 42°S , revealing the baroclinic nature of the flow and depth-integrated agreement with observations. The introduction of the bottom topography greatly reduces the northward transport through the Tasman Sea (0.1 Sv vs. 5.3 Sv), while increasing the IPT transport (13.7 Sv vs. 10.5 Sv). These changes combine to produce a reduced transport in the Tasman Front (23.1 Sv vs. 31.6 Sv). Although mass balance of the region still requires the EAUC and ECC to proceed southward, the decrease in the Tasman Sea transport gives a smaller transport in both the *after separation* EAUC (3.8 Sv vs. 13.5 Sv) and the ECC (11.7 Sv vs. 14.9 Sv). The simulated

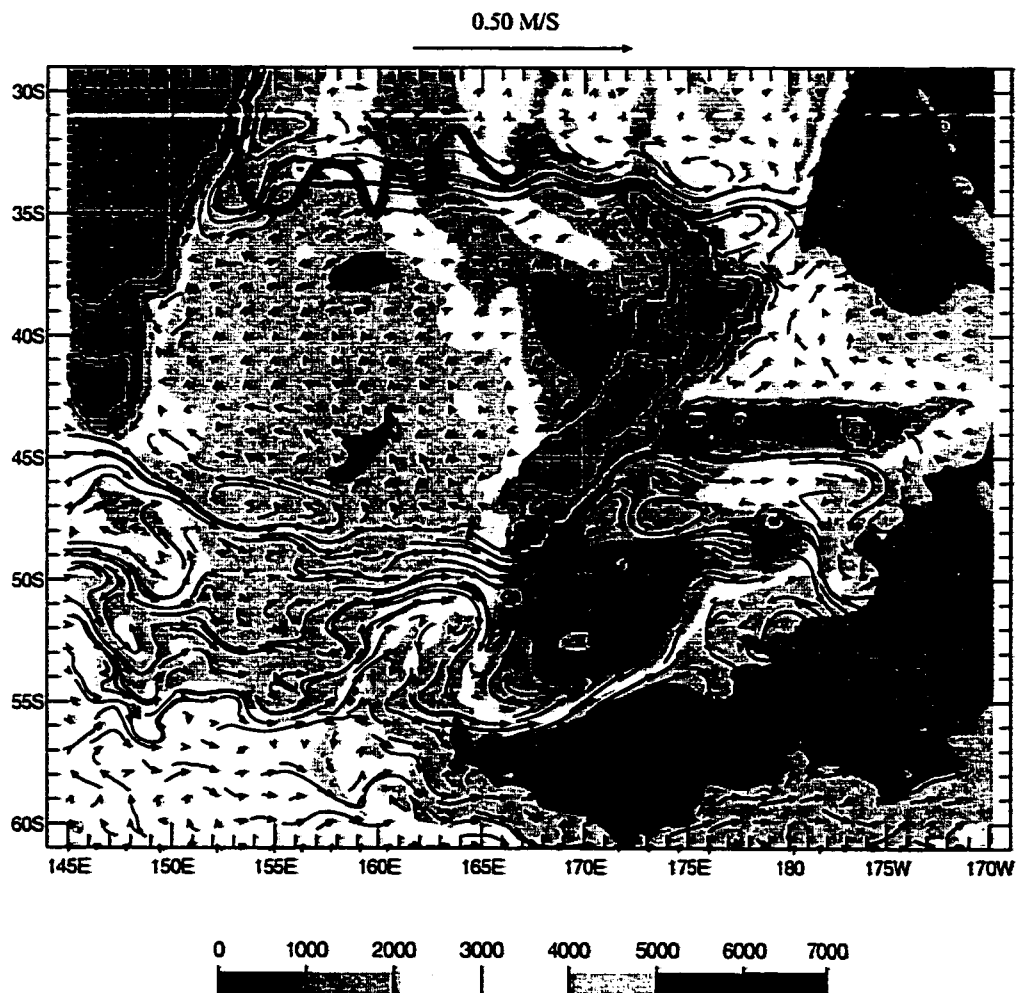


Figure 16. Mean surface currents from the 1/8° nonlinear six-layer simulation with realistic bottom topography, RB8a, superimposed on the bottom topography. Note the correct placement of the meanders in the eastern portion of the Tasman Front and the presence of the eddies north of New Zealand as well as reduced flow through the Tasman Sea compared to FB

Southland Current flows (20.2 Sv vs. -4.3 Sv) in the observed direction, revealing that its location is determined by bottom topography.

The major differences between FB and RB8a are the incorporation of bottom topography, which introduces a bottom layer flow that is constrained to follow f/h contours, and the change in the initial depth of interface 5. The introduction of bottom topography has two major ramifications: (1) reduction of baroclinic instabilities and (2) bottom steering. When the bottom layer flow is constrained by topography, it cannot freely adjust to perturbations and become out of phase with the surface layer. This restriction reduces the distribution of baroclinic instabilities and their potential for occurrence. Since baroclinic instabilities convert potential energy of the mean flow to eddy potential energy, they effectively flatten mean isopycnals. This flattening restricts the transport south of New Zealand since transport is related to the change in depth of isopycnals via the thermal wind relation. The greater depth of the original interfaces in RB8a (1500 m for interface 5) compared to FB (1000 m for interface 5) mitigates the effect of isopycnal outcropping and provides greater potential for transport south of New Zealand and Australia. The decrease of baroclinic instabilities and the increase in initial interface depth result in much deeper isopycnals south of Australia and New Zealand in RB8a than FB (Table 4). The relative deepening of the isopycnals allows more transport south of New Zealand, and, consequently, decreases the northward flow through the Tasman Sea.

The inclusion of bottom topography can substantially affect surface currents that do not directly impinge on the topography. Hurlburt and Metzger (1998) found

indications of the Shatsky Rise topography affecting the bifurcation of the Kuroshio. This steering is due to the abyssal currents advecting upper layer thickness gradients and, therefore, surface currents. Conservation of potential vorticity is a sufficient constraint to allow even deep low amplitude topographic features to steer the abyssal flow. Hurlburt and Thompson (1980, 1982, and 1984) used the continuity equation to demonstrate how upper ocean currents can be influenced by abyssal flow. In a two-layer model it can be shown that the two layer velocities are linked by:

$$\bar{v}_{1g} \cdot \nabla h_1 = \bar{v}_{2g} \cdot \nabla h_1 \quad (8)$$

where \bar{v}_{kg} is the geostrophic velocity in layer k . The left-hand side of (8) is the geostrophic contribution to the advective term in the continuity equation (3) for layer 1. Additionally the geostrophic balance of the internal mode in a two-layer model is given by:

$$\hat{k} \times f(\bar{v}_{1g} - \bar{v}_{2g}) = -g' \nabla h_1 \quad (9)$$

where $g' = g(\rho_2 - \rho_1)/\rho_0$. When the surface currents are much larger than the abyssal currents ($|\bar{v}_{1g}| \gg |\bar{v}_{2g}|$), which is typically the case in a two layer model, equation (9)

indicates that ∇h_1 can be used as an approximate measure of \bar{v}_{1g} . From this observation and the combined effects of (8) and (9), we see that the abyssal currents can advect upper layer thickness gradients and, therefore, steer upper layer currents. Hurlburt et al. (1996) showed that, although this theory formally breaks down in the multi-layer case, this steering effect remains when the first baroclinic and barotropic modes dominate the flow regime. The separation of the simulated Tasman Front in RB8a into its natural modes

(Fig. 17) reveals that the first baroclinic and barotropic modes do indeed dominate the flow regime. A comparison of the velocities within the surface jet from FB and RB8a (Fig. 14 and Fig.18) indicates the presence of bottom topography in the simulation greatly decreases the surface velocities associated with the Tasman Front. This decrease in surface velocities translates into less vigorous changes in sign of dQ/dy (Fig. 19) and less tendency for horizontal shear instabilities.

As discussed in the previous section, the presence of mixed barotropic/baroclinic instabilities in FB determines the wavelength of the simulated meanders in the Tasman Front. The effect on the meander wavelength by the decrease of baroclinic instabilities due to the inclusion of bottom topography in RB8a is compensated by bottom steering, resulting in meanders that are similar in wavelength to those in FB but whose phase now agrees more closely with observations. Inspection of the bottom topography (Fig. 2) beneath the Tasman Front reveals a series of ridges and valleys which constrain the abyssal flow and affect the surface flow. As discussed earlier in this section, the presence of bottom topography does not allow the abyssal layer to freely adjust and create meanders solely due to baroclinic instabilities. The wavelengths of the meanders are not directly determined by the presence of the instabilities themselves, although the instabilities may provide a length scale for the meanders. Instead, the barotropic and baroclinic instabilities contribute energy to the abyssal layer providing greater bottom steering, which determines the wavelengths.

Increasing the resolution of RB8a to $1/16^\circ$ (RB16) (Fig. 20) significantly strengthens the amplitudes of the meanders in the eastern half Tasman Front and

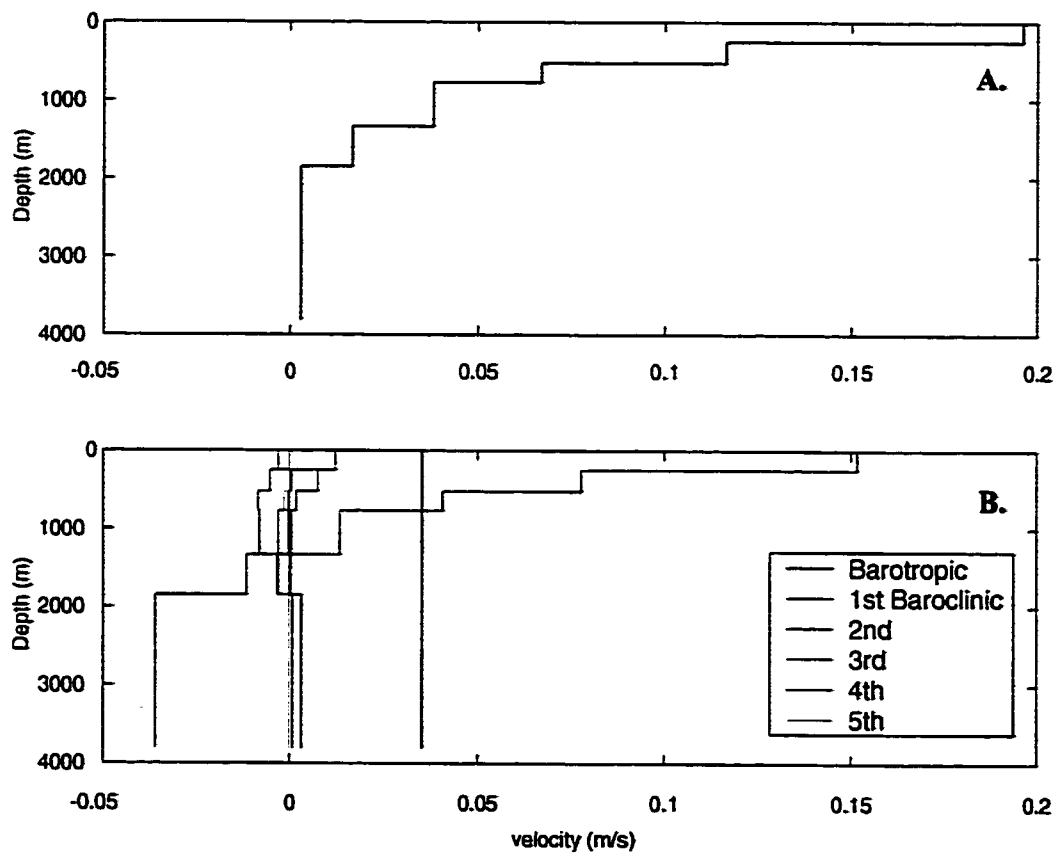


Figure 17. a) Velocity within the simulated Tasman Front (RB8a) as a function of depth. b) Velocity of RB8a separated into the barotropic mode and five baroclinic modes. Note that although the barotropic and firstbaroclinic modes dominate the velocity field, one of the higher modes is still significant.

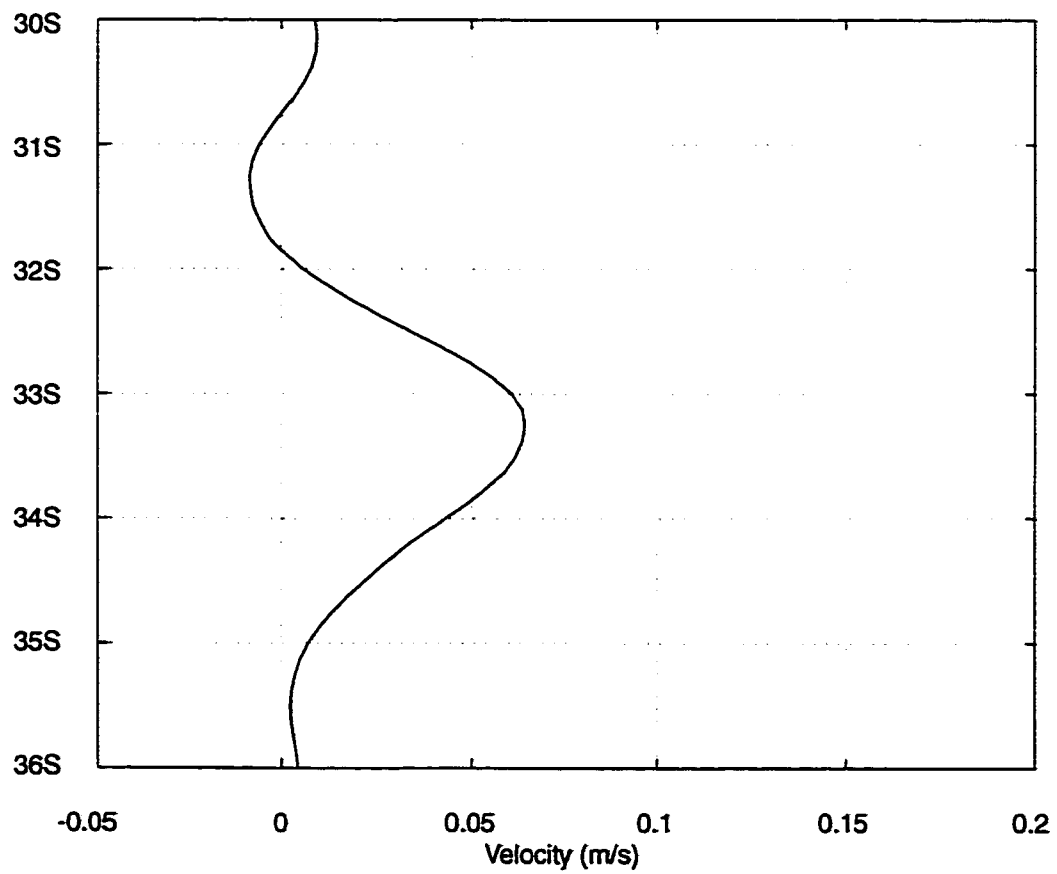


Figure 18. Average velocities of the surface jet associated with the Tasman Front from RB8a at 165°E. The velocities were depth-averaged through the top five layers.

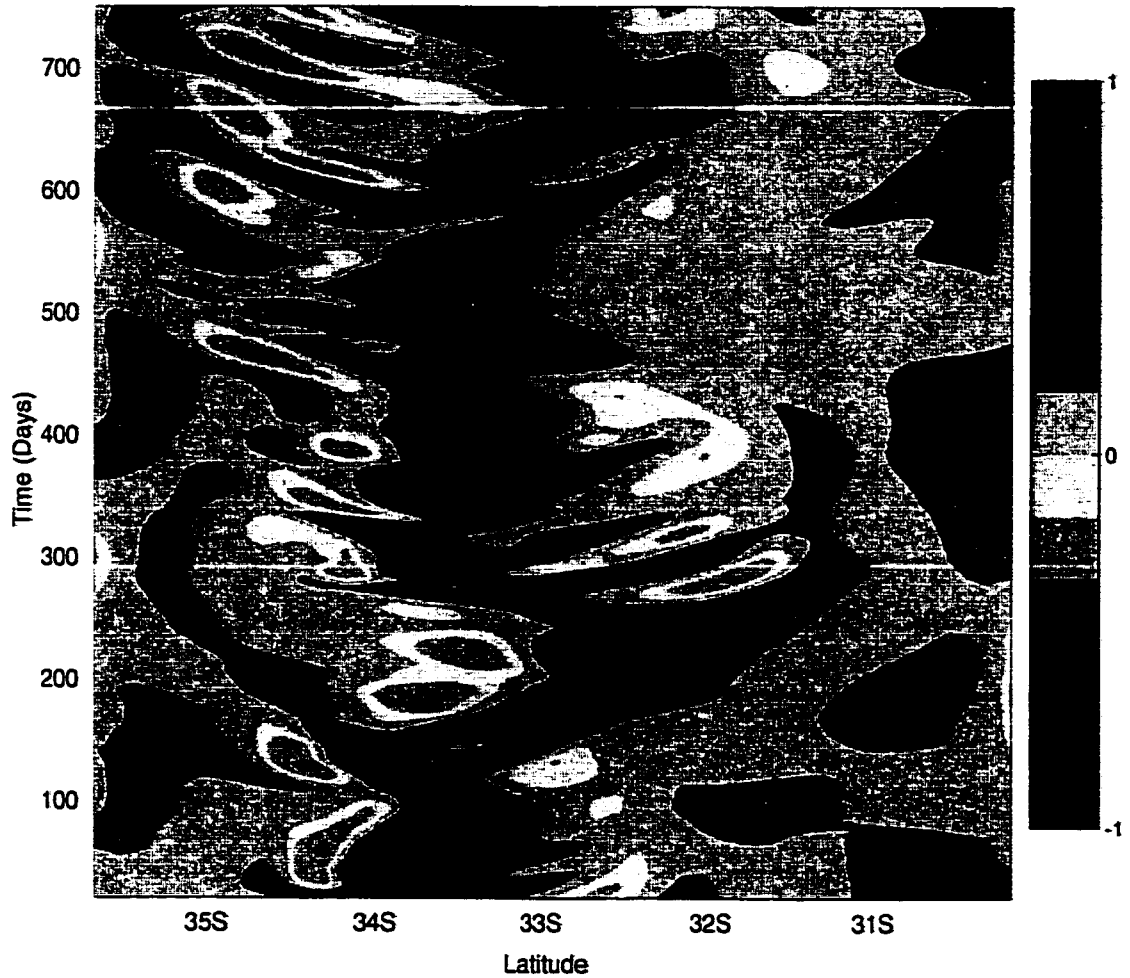


Figure 19. Latitude-time plot of normalized dQ/dy at 165°E from RB8a where Q is the absolute vorticity calculated from the depth-averaged velocities. Note the change in sign of dQ/dy , a necessary condition for barotropic instabilities.

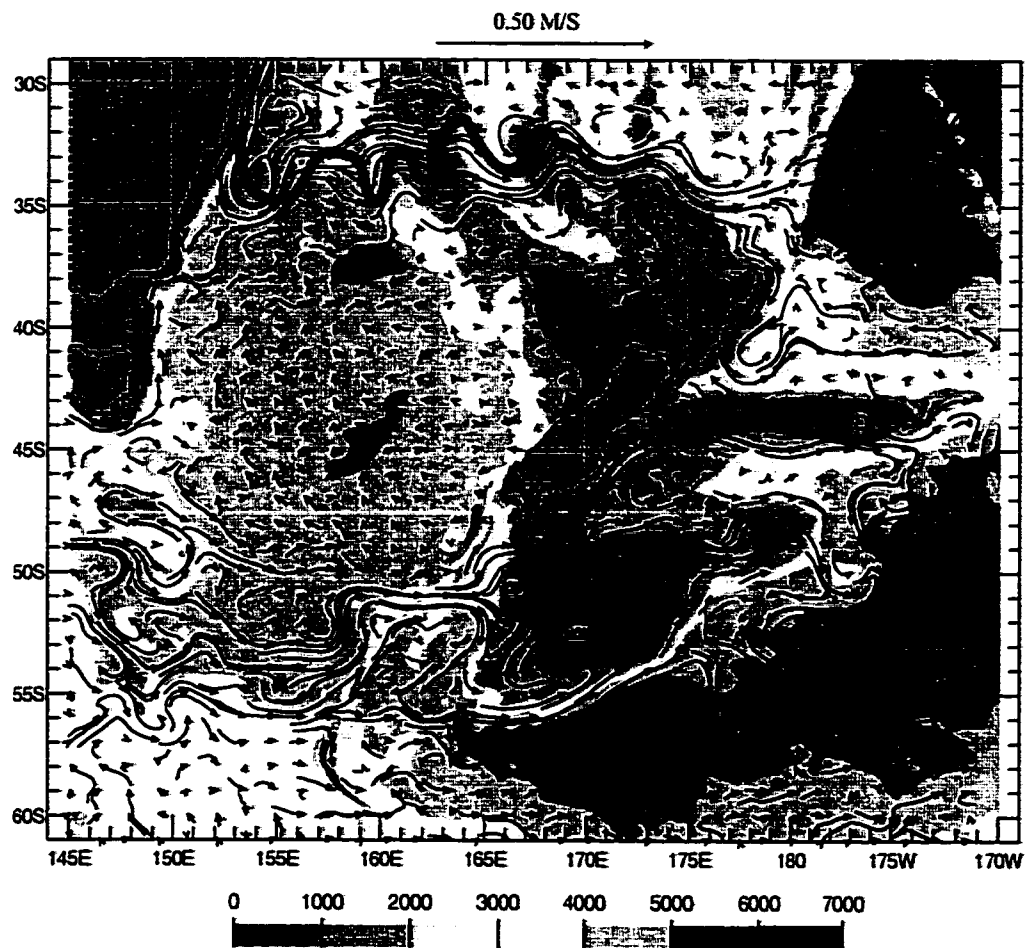


Figure 20. Mean surface currents from the 1/16° nonlinear six-layer simulation with realistic bottom topography, RB16, superimposed on the bottom topography. Note the larger meanders in the Tasman Front and the presence of the NCE and WE. The ECE has merged with the low, obscuring both features.

produces meanders in the western portion of the Tasman Front (Meanders A, B, C, and D, labeled on Fig. 2). Although located slightly south of the observed meanders, the simulated meanders in the western portion agree quite well in phase, amplitude, and wavelength. The closer agreement of the simulated meanders with observations suggests stronger upper ocean - topographic coupling in RB16 than in RB8a.

The increased resolution also strengthens the northward transport through the Tasman Sea (6.4 Sv vs. 0.1 Sv) and, therefore, the eastern transport associated with the Tasman Front (27.5 Sv vs. 23.1 Sv). These increases are felt downstream of the current system in the EAUC (8.5 Sv vs. 3.8 Sv) and the ECC (15.9 Sv vs. 11.7 Sv) but have less effect on the Southland Current (18.3 Sv vs. 20.2 Sv) or the IPT (12.2 Sv vs. 13.6 Sv). The quasi-stationary eddies corresponding to the Wairarapa Eddy and the NCE are evident, but in the mean the ECE and the low have merged. Uddstrom and Oien (1999) were also unable to detect a robust ECE in their SST fields, indicating a high amount of variability in this region.

The simulated sea surface height variability of RB16 qualitatively agrees with Topex/Poseidon altimeter data (Fig. 21). The peak values of variability in the EAC and New Zealand region (the separation point of the EAC, along the Tasman Front, and directly north and east of North Island) are co-located in the simulations and the observations and can be directly linked to physical phenomena. The large variability in the region of the EAC separation is due to both the seasonal migration of the separation point and eddy shedding, while the large amount of variability along the Tasman Front indicates significant movement of the meanders. The large variability north and east of

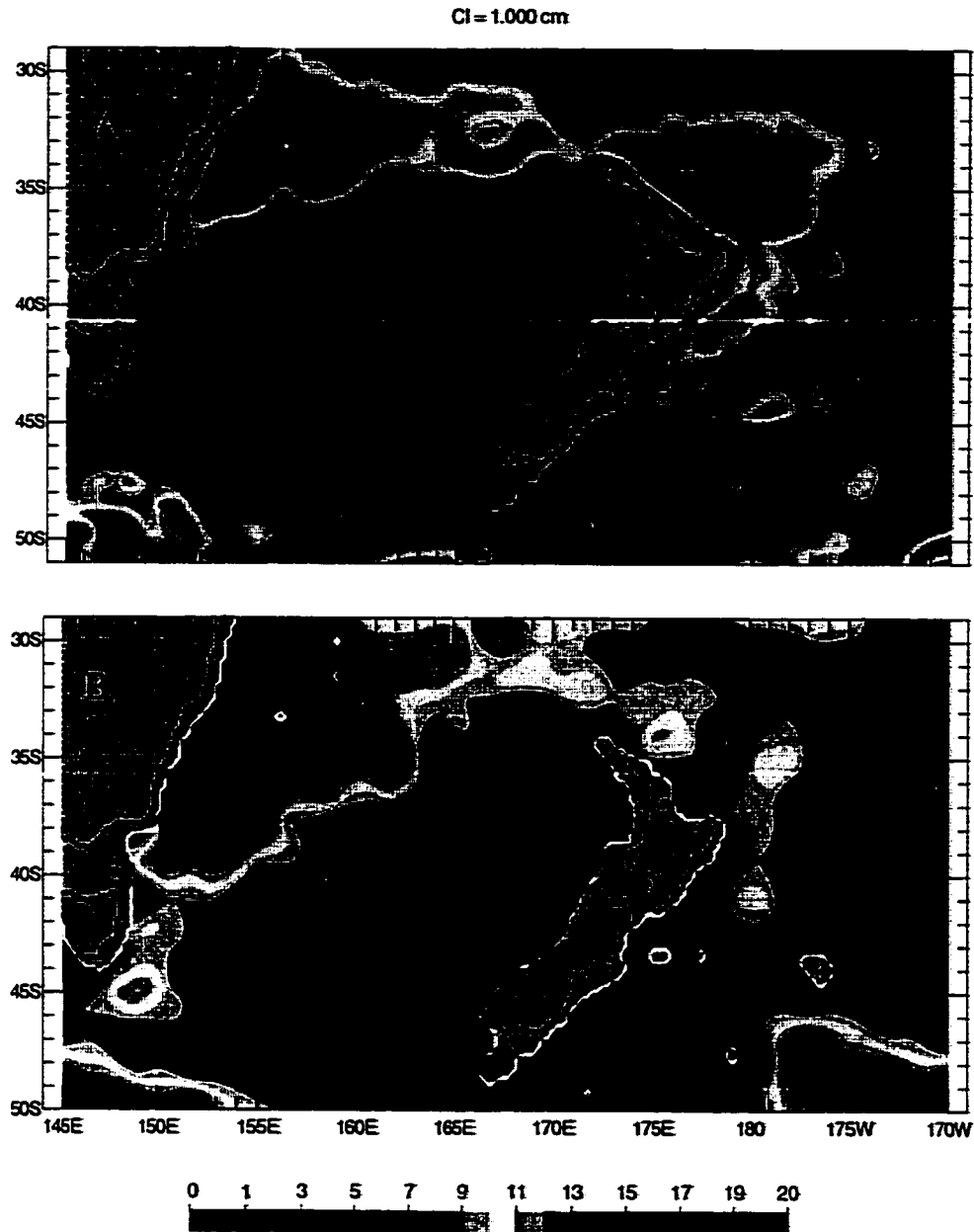


Figure 21. Sea surface height variability obtained from (a) RB16 and (b) Topex/Poseidon altimeter data. Both show large variability at the EAC separation point. RB16 exhibits large variability of the flow field north and east of North Island. While the observed data show qualitative agreement in the variability pattern of the SSH around North Island, it is much lower in amplitude.

North Island can be linked to the presence of the quasi-stationary eddies and meandering of the EAUC and ECC.

Since the model is hydrodynamic and forced by monthly windstress climatology and the actual ocean is subject to seasonal thermal forcing and higher frequency winds, the overall variability of the model is less than that measured by TOPEX/POSEIDON. Lower modeled SSH variability in locations such as east of Tasmania and within the southern section of our region of interest is expected. However, while the simulated variability north of New Zealand agrees qualitatively with observations, it is significantly higher than observations. The disagreement between the model and observations can be linked to the model's inability to adequately resolve the transport south of New Zealand and Australia. As discussed in section 3b, the reduction of flow south of New Zealand forces northward flow through the Tasman Sea, resulting in an unrealistically large current associated with the Tasman Front and therefore the EAUC. Instabilities in these currents result in larger than observed SSH variability. The location of the observed ECE is a region of extremely high variability in the model and observations, providing a possible explanation for the mixing of the low and the ECE in the simulation.

Maps of surface and abyssal eddy kinetic energy (EKE) of RB8a and RB16 (Fig. 22) demonstrate that the energy in both the surface and abyssal layers increases with grid resolution. The increased resolution in RB16 allows greater flow instabilities and an increased rate of energy transfer to the abyssal layers via mixed baroclinic-barotropic instabilities. Hogan and Hurlburt (2000) provide a discussion and illustration of the vertical transfer of energy. A mean value of R_b for eddies produced by RB16 is 6.9,

$C = 0.250 \text{ m}^2 \text{ s}^{-2} (\text{Log})$

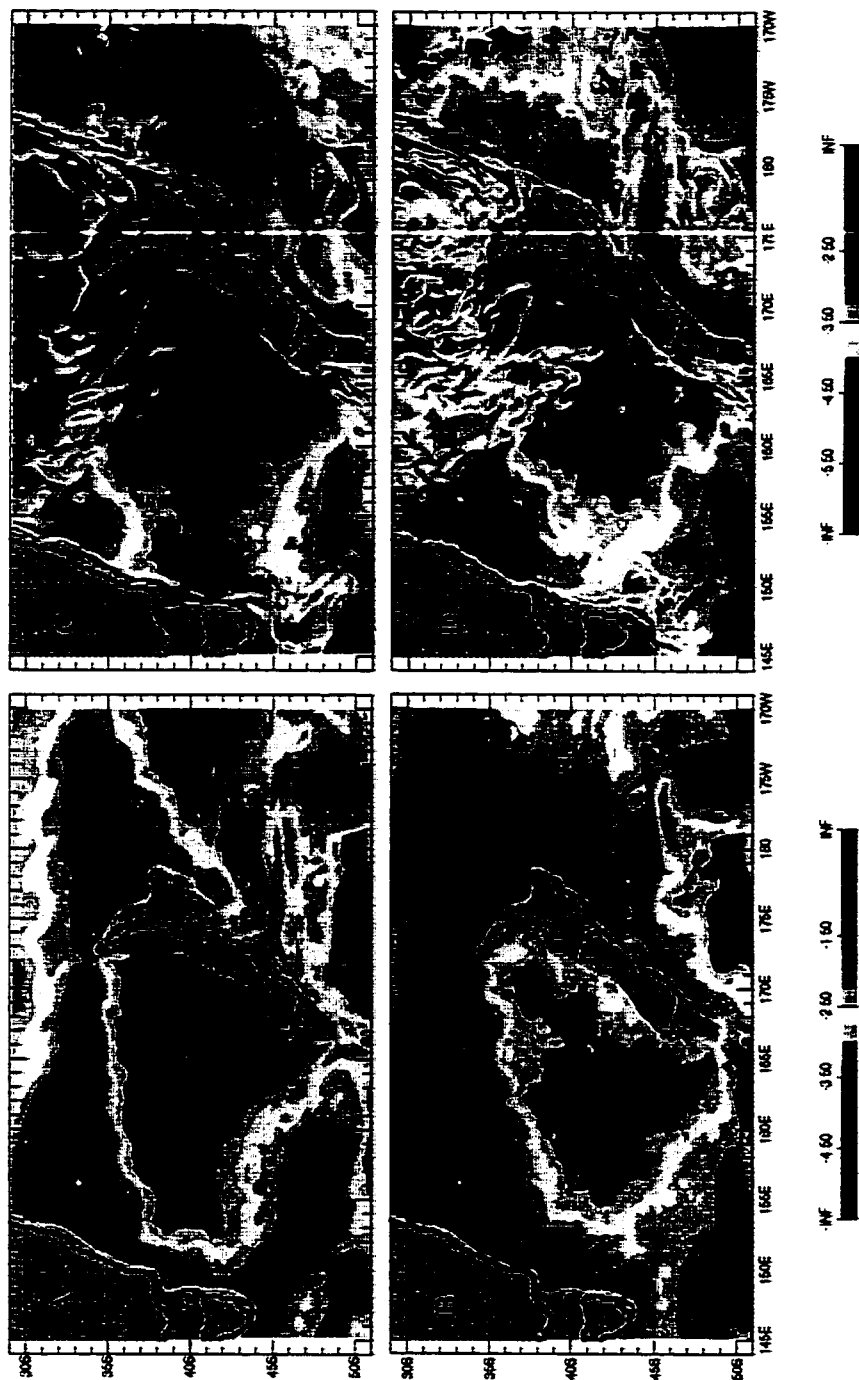


Figure 22. Mean surface layer eddy kinetic energy (EKE) of (a) RB8a and (b) RB16 and abyssal layer EKE of (c) RB8a and (d) RB16. The contour interval is $0.25 \text{ m}^2/\text{s}^2$ (Log). Note the change in color bar between surface and abyssal layers. The energies of both layers increase as the resolution increases and the surface and abyssal layer EKE are co-located, both signs of baroclinic instabilities.

which is slightly lower than FB, suggesting that the eddies' formation may be due to mixed barotropic/baroclinic instabilities. A comparison of the surface jet velocities in RB16 and RB8a (Fig.18 and Fig. 23) demonstrate that the increased resolution results in a much more variable current associated with the Tasman Front. A latitude-time plot of the derivative of the depth-averaged absolute vorticity (dQ/dy) at 165°E (Fig. 24) shows that the derivative changes sign more frequently than either FB or RB8a, suggesting a greater susceptibility to barotropic instabilities.

Although baroclinic and barotropic instabilities are very efficient mechanisms for transferring energy from the surface layers to the abyssal layers, other mechanisms may also drive abyssal EKE, such as vertical mixing or direct barotropic forcing by temporal variations in the wind stress. Very little vertical mixing between the surface and abyssal layers occurs in the area of the Tasman Front and New Zealand, although a significant amount does occur south of New Zealand, a fact that affects the location of the Southland Current. The co-location of EKE maxima in the surface and abyssal layers combined with the increase in variability and tendency for instabilities with resolution is clear evidence that mixed barotropic/baroclinic instabilities are present (Holland and Lin, 1975) and that they, and not a barotropic response to the seasonal wind variations, are the major source of abyssal EKE (Hurlburt and Metzger, 1998). This increase in instabilities acts to create more isopycnal outcropping in the Antarctic region (Table 4) in RB16 than in RB8a, which results in a greater northward transport through the Tasman Sea and a larger transport associated with the Tasman Front.

The link between abyssal energy and upper ocean – topographic coupling can be

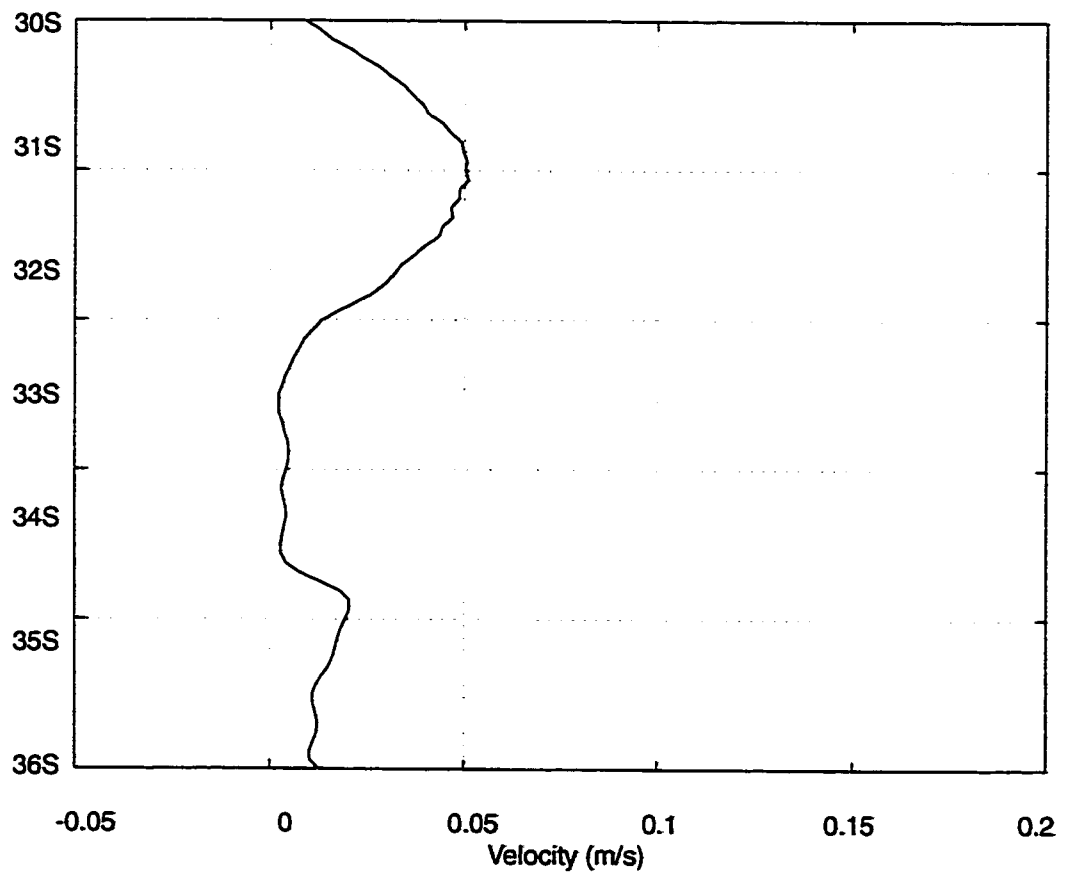


Figure 23. Average velocities of the surface jet associated with the Tasman Front from RB16 at 165°E. The velocities were depth-averaged through the top five layers.

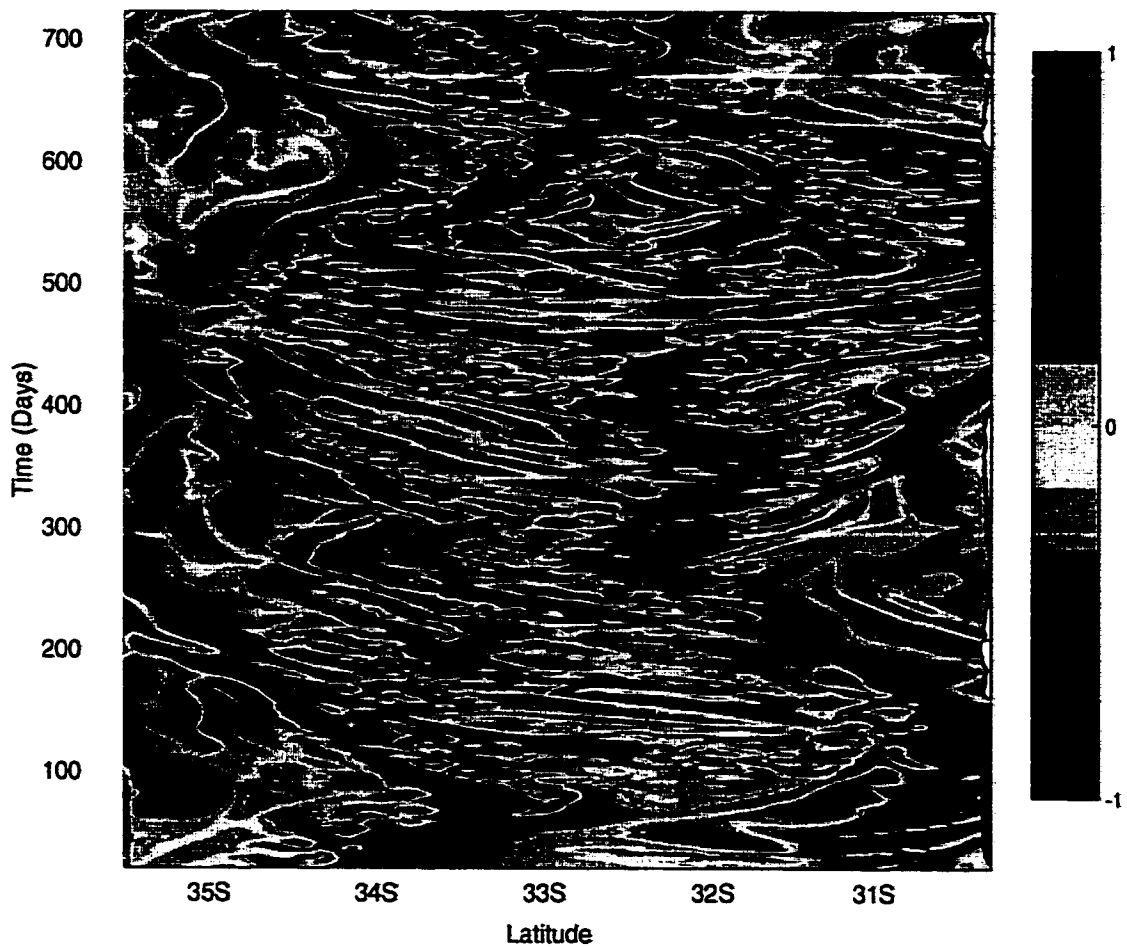


Figure 24. Latitude-time plot of normalized dQ/dy at 165°E from RB16 where Q is the absolute vorticity calculated from the depth-averaged velocities. Note the change in sign of dQ/dy , a necessary condition for barotropic instabilities.

clearly seen. Large amounts of abyssal energy, indicating strong abyssal currents, are co-located with bottom-steering of upper ocean currents such as the meanders in the Tasman Front (Figs. 16, 20 and 22). RB16 with a larger amount of abyssal energy and, therefore, more energetic abyssal currents, produces more bottom steering and larger meanders than RB8a. The increased variability and barotropic/baroclinic instability enable more upper ocean – topographic coupling in the higher resolution simulation. For this reason, we use these simulations to investigate in detail the role of several topographic features in steering the surface flow field. Three separate areas merit discussion: the meanders of the Tasman Front, the apparent bottom-steering of the ECC over the Hikurangi Trench, and the location of the Southland Current. As seen in Figure 20, many surface features appear to be coupled with particular topographic features. Topographically driven abyssal currents intersecting surface currents at large angles force the surface currents to be displaced in the direction of the abyssal flow where the flows overlay. The surface currents tend to return to the same latitude after the perturbation by the abyssal currents, consistent with potential vorticity conservation. Abyssal flow superimposed over sea surface height contours (Fig. 25a) show that each meander, with the exception of the very first, of the Tasman Front is associated with meridional abyssal flow on the side of a ridge or a trough. The first meander is due to a separation overshoot and retroflexion as described by Ou and De Ruijter (1986). Two meanders discussed by Stanton (1979), the large southward meander located at the New Caledonia Trough (166°E , Meander F) and the northward meander over Norfolk Ridge (167°E , Meander G) are both driven by meridional flows along ridges. Abyssal currents also drive meanders documented by

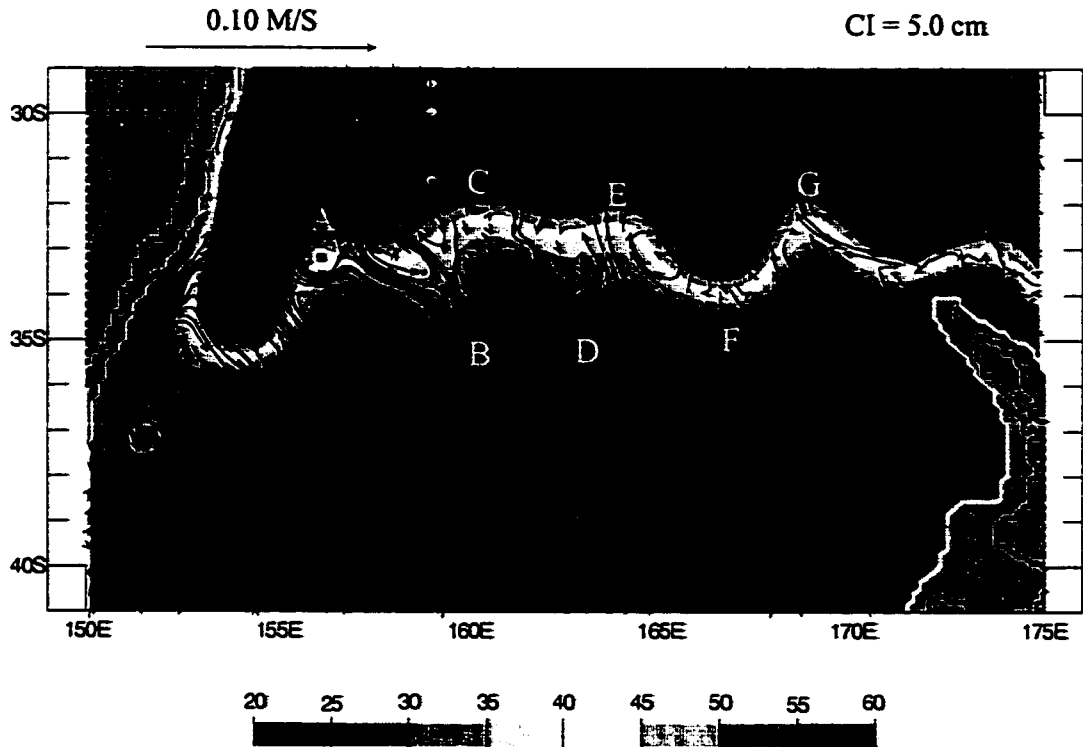


Figure 25a. Mean abyssal layer currents (black arrows) from the $1/16^\circ$ nonlinear six-layer simulation with realistic bottom topography, RB16, superimposed on sea surface height in the vicinity of the Tasman Front. The letters on the simulated meanders correspond to the observed meanders in Figure 2. Note the steering of the surface layer meanders by the abyssal flow following f/h contours.

Mulhearn (1987) that are associated with the Dampier Ridge (159°E, Meander B) and Lord Howe Rise (161°E, Meander E). While the directions of meanders A, C, E, F, and G are consistent with movements due to conservation of potential vorticity of a barotropic flow, Stanton (1979) clearly shows that the flow associated with the Tasman Front is highly baroclinic. Also the southward meanders located directly east of Dampier Ridge (Meander B) and on the west side of the Lord Howe Rise (Meander D) are opposite in direction to those predicted by conservation of potential vorticity. However, the corresponding simulated meanders are directly above southward abyssal flow along the ridge, which force the surface flow to form southward meanders.

At first glance, the flow of the ECC appears to be governed by the Hikurangi Trough. It separates very near the location of the Chatham Rise and apparently follows this ridge line. In fact, the separation point in the realistic bottom topography simulations is the same as the flat bottom model. As mentioned in Section 3a, the separation is governed by the integrated wind stress curl and not bottom topography.

A unique combination of bottom steering and westward propagation of the steered surface layer thickness gradients governs the Southland Current. While a flat bottom simulation does not produce a realistic Southland Current, the inclusion of bottom topography does, revealing that bottom steering controls the location of the current. Inspection of the surface currents in RB8a and RB16 (Fig. 16 and Fig. 20) show a strong northeastward flow along the coast of South Island, that turns eastward near the Chatham Rise, and proceeds southward after ~175°W. These strong currents coincide with a strong front that can be seen in the sea surface height of the simulation (roughly

corresponding to the white contour interval in Fig. 25b) extending across the southern edge of the Tasman Sea and east of New Zealand. This current system is associated with the Southern Hemisphere STF that extends through the entire South Pacific. The abyssal current flowing northeastward along the eastern coast of New Zealand is extremely small (Fig. 25b); however, there is a strong meridional deep western boundary current (DWBC) off the eastern edge of the Campbell Plateau ($\sim 56^{\circ}\text{S}$, 165°E to $\sim 45^{\circ}\text{S}$, 173°W), identified by Warren (1981). This DWBC stems from the eastward current associated with the STF, which has sufficient vertical structure in some locations to affect abyssal currents, as can be seen by the co-location of abyssal flow and SSH contours (Fig. 25b) between 51°S and 56°S in the Tasman Sea. Gordon (1975) using current meters placed 100 meters above the sea floor recorded a velocity of 29 cm/s at approximately 5000 m at 56°S , 170°E , directly south of the Campbell Plateau. These strong abyssal currents flow relatively unimpeded through the southern edge of the Tasman Sea, but at 165°E they encounter the Campbell Plateau. Since abyssal flow is constrained to follow f/h contours, the abyssal currents separate from the surface flow and are directed northeastward along the eastern edge of Campbell Plateau and become a DWBC (Fig. 25c).

As the surface zonal flow of the subtropical front encounters this now meridional abyssal flow at $\sim 178^{\circ}\text{E}$, a portion of the surface flow is advected northward. The northward displacement of the water parcels associated with the eastward flowing STF creates an imbalance in potential vorticity. Since there is nothing to constrain this now meridional surface flow, the surface layer thickness gradients associated with it propagate westward in an attempt to conserve potential vorticity and appears as a western boundary

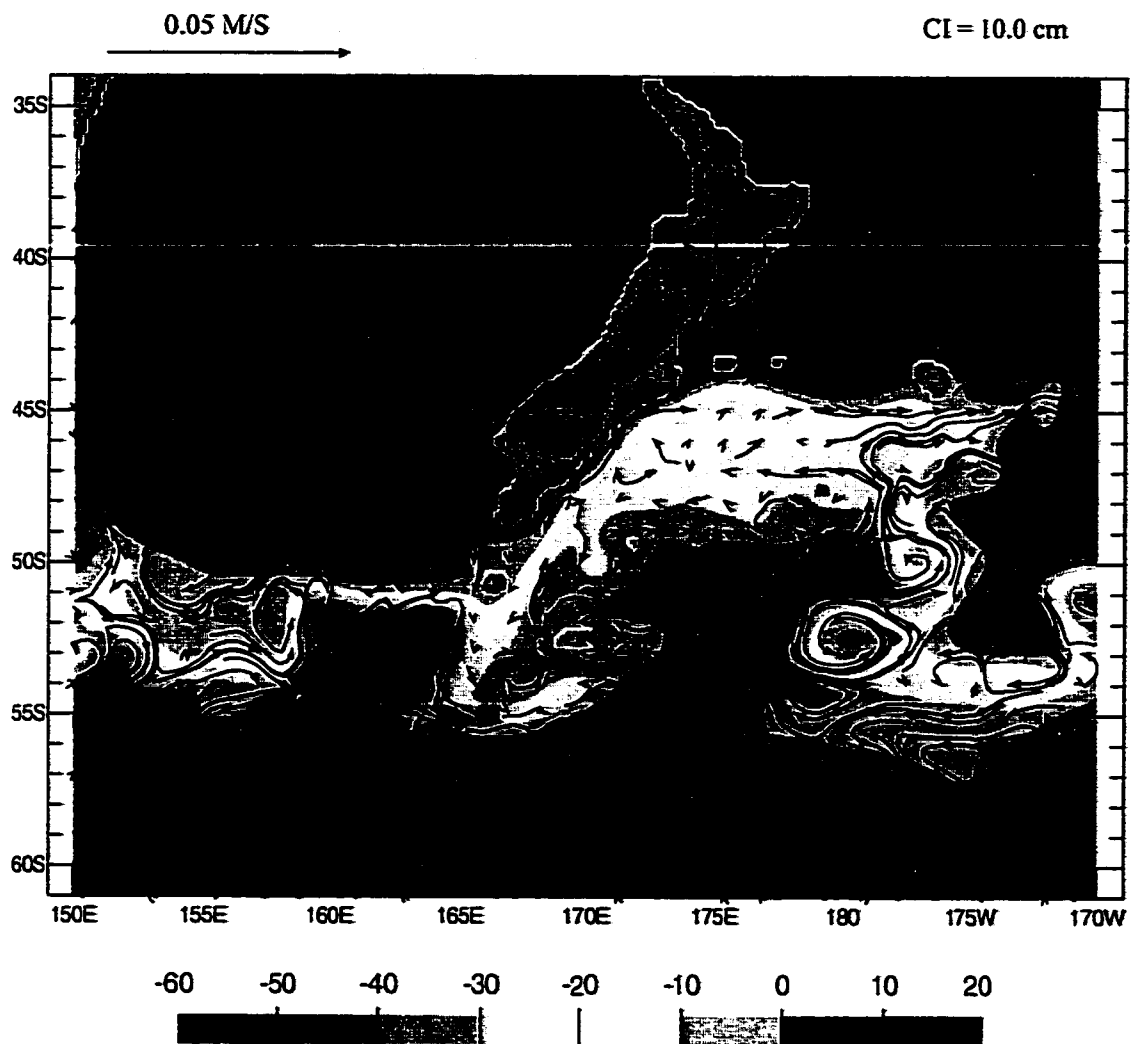


Figure 25b. Mean abyssal layer currents (black arrows) from 1/16° nonlinear six-layer simulation with realistic bottom topography, RB16, superimposed on sea surface height southeast of New Zealand. The white contour corresponds to the Subtropical Front/Southland Current. Note the lack of a strong abyssal current directly beneath the Southland Current and the extremely strong current east of the Campbell plateau.

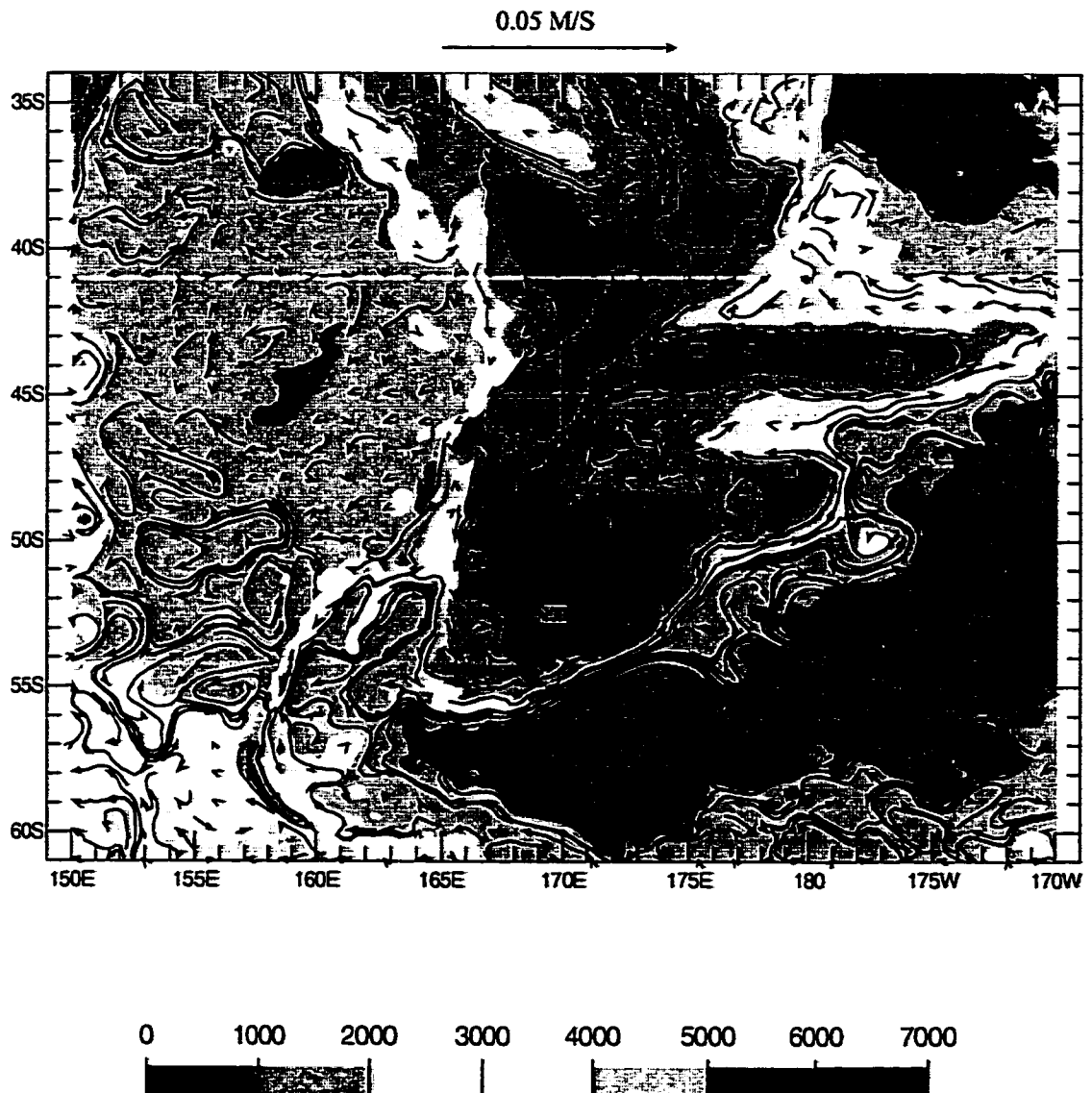


Figure 25c. Mean abyssal layer currents (black arrows) from 1/16° nonlinear six-layer simulation with realistic bottom topography, RB16, superimposed on bottom topography. Note the topographically constrained DWBC east of the Campbell Plateau.

current off the eastern coast of South Island. After the STF passes east of this meridional DWBC, it returns to its original latitude as expected by conservation of potential vorticity. Removal of New Zealand from the $1/8^\circ$ simulation (RB8b, Fig. 26) reveals that the meridional surface structure continues to propagate westward until it encounters a relative high in the mean sea surface height at 155°E caused by eddies that originate on the eastern coast of Tasmania and are advected eastward by the current associated with the STF. (These eddies are apparent in animations of the simulations and the high EKE in the surface layer of RB8a (Fig. 22a)).

The northward movement of the STF is not a barotropic response of a fluid column to a large change in bottom topography (ocean depth decreases from 5000 m to less than 1500 m at 166°E) and therefore change in potential vorticity. If the northward movement were due to conservation of potential vorticity, then the meridional structure would not propagate westward when New Zealand is removed.

The dynamics behind this combination of bottom steering and westward propagation can be illustrated by a simple example. A two-layer system simulated using NLOM consisting of a surface zonal flow (representing the STF) and an abyssal meridional flow (representing the DWBC) is examined. The domain is rectangular with zonal (165°E to 105°W) and meridional (55°S to 15°S) dimensions that roughly correspond to the South Pacific Ocean east of New Zealand. Boundary conditions are no slip and closed on all sides except for two ports in each layer. The surface flow is generated by 2° wide meridional ports in layer 1 at 45°S on the east and west boundaries. These ports correspond to flow south of New Zealand (western inflow port) and flow

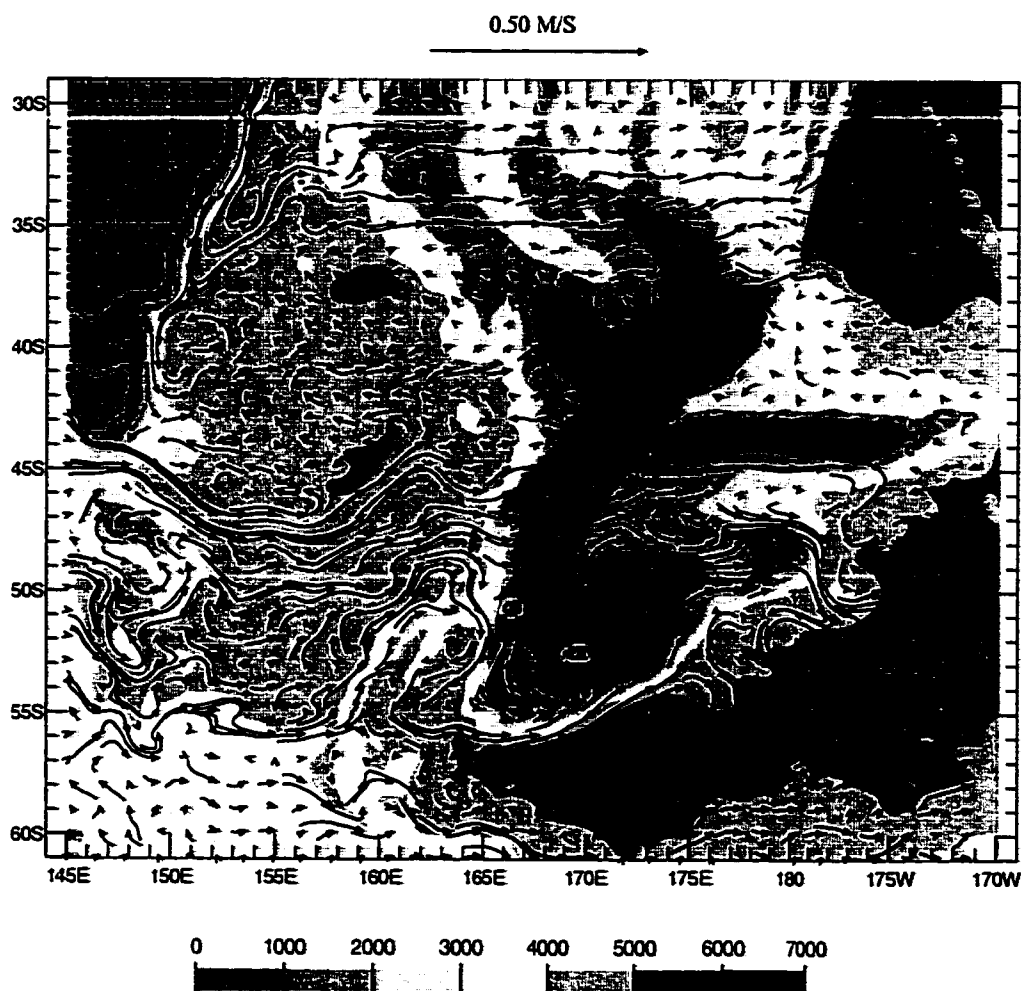


Figure 26. Mean surface currents from the $1/8^\circ$ nonlinear six-layer simulation with realistic bottom topography and New Zealand removed, RB8b, superimposed on the bottom topography. Note that the meridional structure corresponding to the Southland Current has propagated westward until it encounters a high in the mean sea surface height caused by eddies formed off the eastern coast of Tasmania, which acts as a western boundary.

through the Drake Passage (eastern outflow port). The abyssal flow is constrained to flow roughly northward by a sharp gradient in bottom topography (Fig. 27) and is generated by 2° wide zonal ports in layer 2 at 177°E on the north (outflow) and south (inflow) boundaries. Although the flow field has reached a statistical equilibrium in the global models previously examined, transient simulations are instructive in the investigation of the dynamics of the Southland Current. Examination of several snapshots of the transient simulation reveals westward propagation of the meridional Southland Current. First, the simulation is allowed to run until equilibrium with a zonal surface flow but no abyssal flow (Fig. 28a). Due to the baroclinic nature of the flow structure, the surface flow field is unaffected by the change in topography and proceeds throughout the domain as a zonal flow. This equilibrium state is designated as $T = 0$ years. At $T = 0$ years, the meridional abyssal flow is turned on, which over time produces a displacement of the surface flow, shown here at $T = 3$ years (Fig. 28b). A snapshot of the flow field at $T = 7$ years (Fig. 28c) shows the meridional structure has begun to propagate westward as a Rossby wave. When this meridional flow encounters the western boundary, it forms a northward boundary current. At $T = 80$ years, or the extent of the simulation, the surface flow has formed a strong western boundary current due solely to the meridional abyssal flow (Fig. 28d). As the surface flow passes directly over the abyssal flow, it returns to its previous latitude, creating a southward flow as seen by Uddstrom and Oien (1999).

From examination of the simulations we are able to determine the governing dynamics behind several features of the flow field surrounding New Zealand. Upper

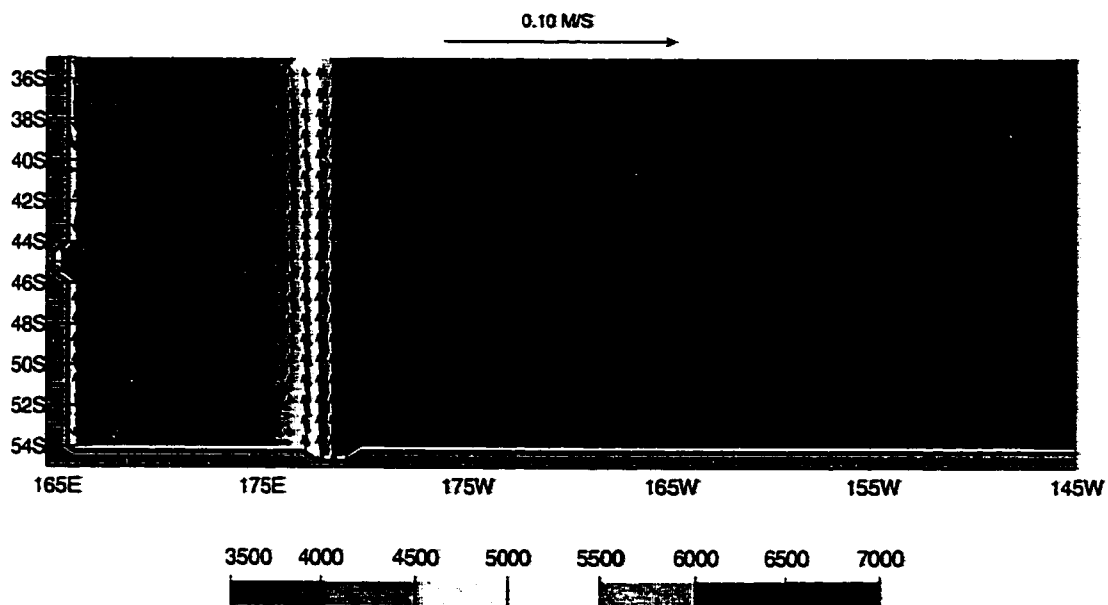


Figure 27. Abyssal layer currents (black arrows) from nonlinear two-layer simulation superimposed on the bottom topography

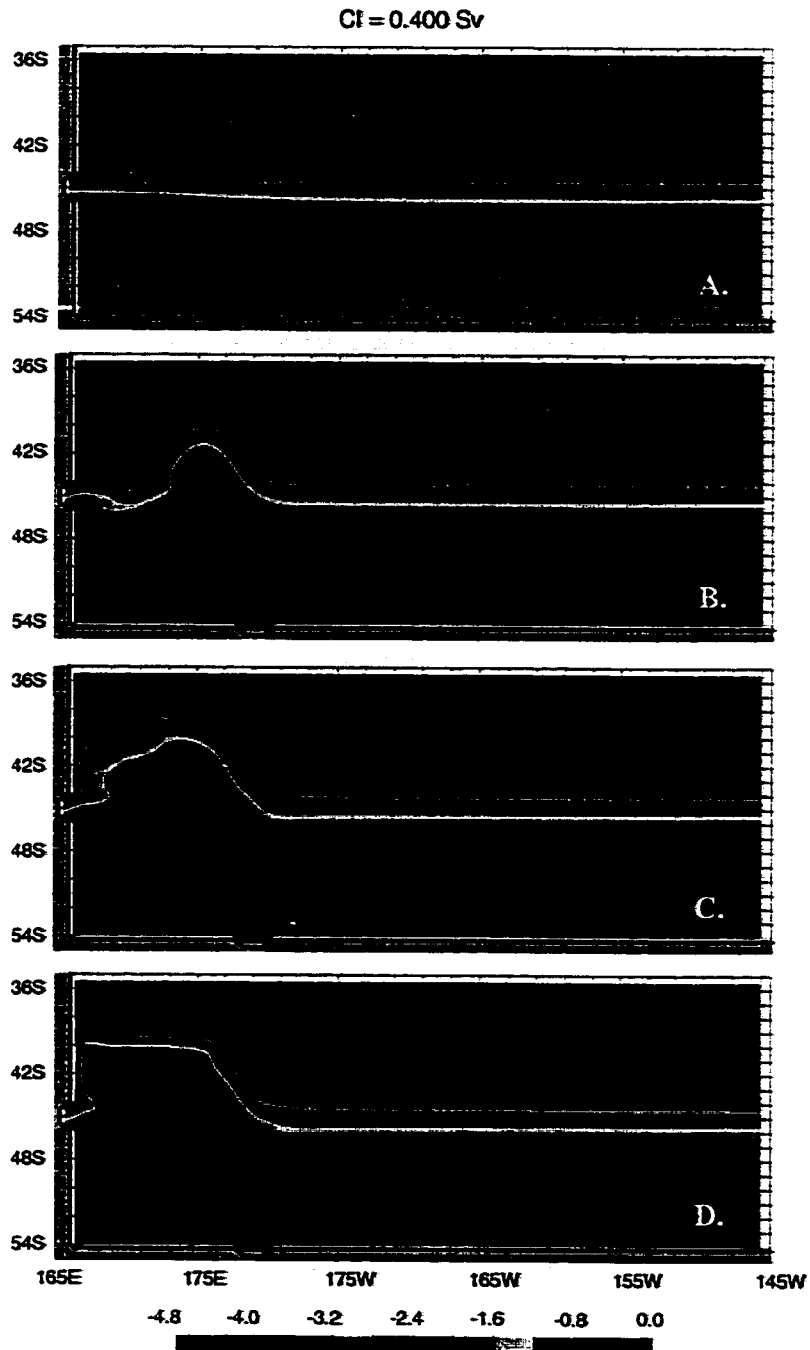


Figure 28. Surface transport streamfunctions from two-layer simulation at a) $T = 0$ years (no abyssal flow), b) $T = 3$ years, c) $T = 7$ years, d) $T = 80$ years. Note the beginning of a western boundary current at $T = 7$ years and a fully formed current at 80 years.

ocean - topographic coupling via mixed barotropic/baroclinic instabilities governs the phase and amplitude of the mean meanders in the Tasman Front. The flat bottom nonlinear model and even the linear model with the added friction patch produce the correct directions and separation points for all examined currents except the Southland Current. The wind stress curl and not bottom topography determine the separation points and direction of the EAC and ECC, while the presence of isopycnal outcropping determine the direction of the EAUC. A combination of bottom-steering and westward propagation of surface layer thickness gradients associated with meridional surface currents governs the location and direction of the Southland Current.

4. SUMMARY AND CONCLUSIONS

Global ocean models with increasing dynamical complexity are used to investigate the dynamics of the East Australian Current, the Tasman Front, and the flow field directly north and east of New Zealand. The simulations have horizontal resolutions of $1/8^\circ$ or $1/16^\circ$ for each variable and vertical resolutions ranging from 1.5 layer reduced gravity to six-layer finite depth with realistic bottom topography. All simulations are forced by the Hellerman and Rosenstein (1983) monthly wind stress climatology and were spun up to statistical equilibrium at $1/2^\circ$ and $1/4^\circ$ resolutions before continuing at $1/8^\circ$ and $1/16^\circ$.

Analysis of these simulations demonstrates that several factors play a critical role in governing the behavior of the EAC, the Tasman Front, the EAUC, the ECC, and the Southland Current. These factors include (1) mass balance of water pathways through the area, (2) gradients in the wind stress curl field, (3) nonlinear flow instabilities, and (4) upper ocean - topographic coupling due to mixed baroclinic and barotropic instabilities. The increased variability of the higher resolution simulation contributes greatly to topographic steering of surface currents that do not directly impinge on the bottom topography.

The transport streamfunctions for a linear reduced gravity model show a series of nested gyres: a supergyre that spans the entire Southern Hemisphere, a smaller gyre that encompasses the South Pacific Ocean, and three smaller gyres that are bounded on the west by Australia and New Zealand. The EAC and ECC are western boundary currents of the gyres, while the EAUC provides non-Sverdrup mass transport between two gyres defined by Sverdrup flow. The Tasman Front is the southern arm of the innermost gyre bounded on the west by Australia. Although the linear model reproduces the large-scale features well, it overestimates the southward transport through the Tasman Sea and produces a Southland Current and EAUC flowing opposite to those observed. The flow through the Tasman Sea is directly linked to the direction of the EAUC. Mass balance in our region of interest shows that the southward flow through the Tasman Sea must be smaller than the difference between the flow through the IPT and the northward flow of the south Pacific subtropical gyre to simulate an EAUC flowing in the observed direction. Decreasing the flow through the Tasman Sea by increasing the local horizontal friction produces a linear solution EAUC flowing in the correct direction. With this decrease all examined currents, with the exception of the Southland Current, flow in the correct direction and separate from the coastlines at the observed locations. However, a nonlinear model is required to investigate the actual dynamics that modify the transport through the Tasman Sea.

A nonlinear six-layer flat bottom simulation produces all currents with the exception of the Southland Current flowing in the observed direction and separating from the coastlines at the observed latitudes. It also produces stationary meanders in the

Tasman Front, the observed quasi-stationary eddies north and east of New Zealand, and isopycnal outcropping. The wavelengths of the simulated meanders in the Tasman Front agree well with observations but their phase and amplitude do not. The wavelengths are shorter than those predicted by constant absolute vorticity theory but correspond well to stationary wavelengths formed by baroclinic instabilities. A beta Rossby number of 7.9 and the wavelength analysis suggests that, although there is significant meridional shear in the surface jet associated with the Tasman Front, the simulated meanders are primarily due to baroclinic instabilities of the barotropic mode. The disagreement in phase and amplitude indicates that bottom-steering is needed to fully reproduce the correct meanders. The simulated transport through the Tasman Sea is northward, in disagreement with observations, resulting in a transport associated with the Tasman Front that is larger than observed. This northward flow occurs because isopycnal outcropping in the ACC reduces the transport that passes south of New Zealand and Australia. Although the model seems to overestimate this effect on eastward transport south of New Zealand, isopycnal outcropping changes the mass transport budget of the region and contributes to a simulated EAUC that flows in the observed direction. An increase in vertical resolution of the flow by the addition of more layers to the model may mitigate the decrease in ACC transport.

Including bottom topography in the $1/8^\circ$ model produces meanders in the eastern portion of the Tasman Front whose phases agree well with observations. Bottom topography prevents the abyssal layer from freely adjusting to the surface layers and creating meanders that agree with flat bottom theory. Instead, bottom steering fueled by

mixed barotropic/baroclinic instabilities creates the meanders of the Tasman Front. All meanders in the Tasman Front, with the exception of the very first, are associated with abyssal flows along the ridges and valleys of the topography. The decrease in baroclinic instabilities south of New Zealand results in less outcropping and, therefore, less northward transport in the surface layers of the Tasman Sea and less associated with the Tasman Front. This simulation reproduces all observed eddies north and east of New Zealand. It also reproduces all examined currents, including the Southland Current.

Increasing the resolution of the simulation to $1/16^\circ$ increases the surface variability and the amount of energy generated in each layer. The geographical co-location of peaks in surface and abyssal EKE coupled with increased energy with increased resolution suggests that instabilities are responsible for the downward transport of energy. The presence of more frequent changes in sign of dQ/dy and a lower beta Rossby number indicate that the instabilities are most likely mixed barotropic/baroclinic instabilities. The increased variability results in more energetic abyssal currents and, therefore, greater upper ocean - topographic coupling, resulting in larger meanders in the Tasman Front. These meanders agree well with observed wavelengths, phases, and amplitudes but the ECE has merged with an observed low in the mean and the northward transport through the Tasman Sea is increased. The separation of the ECC just north of the Chatham Rise seems at first glance to be a result of bottom-steering, since it follows the eastward extension of bottom topography. In fact, the separation of the ECC is due to the wind stress curl field. Bottom topography determines the direction and location of the Southland Current, which is a portion of the Southern Hemisphere STF. Steering of the

STF by a meridional deep western boundary current causes the zonal flow to become meridional. This structure then propagates westward until it encounters New Zealand, forming a western boundary current: the Southland Current.

APPENDIX A

EXPLANATION OF SYMBOLS AND NOTATIONS

$$\nabla \cdot \bar{F} = \frac{1}{a \cos \theta} \frac{\partial F_\phi}{\partial \phi} + \frac{1}{a \cos \theta} \frac{\partial (F_\theta \cos \theta)}{\partial \theta}$$

$$\nabla^2 \Phi = \frac{1}{a^2 \cos^2 \theta} \frac{\partial^2 \Phi}{\partial \phi^2} + \frac{1}{a^2 \cos^2 \theta} \frac{\partial}{\partial \theta} \left(\frac{\partial \Phi}{\partial \theta} \cos \theta \right)$$

A = coefficient of isopycnal eddy viscosity

a = radius of the Earth (6371 km)

C_b = coefficient of bottom friction

C_k = coefficient of interfacial friction

C_M = coefficient of additional interfacial friction associated with entrainment

$D(\phi, \theta)$ = total depth of the ocean at rest

\bar{e}_k = angular deformation tensor

$$e_{\phi\theta_k} = \frac{\partial}{\partial \phi} \left(\frac{u_k}{\cos \theta} \right) - \cos \theta \frac{\partial}{\partial \theta} \left(\frac{v_k}{\cos \theta} \right) = -e_{\theta\theta_k}$$

$$e_{\theta\phi_k} = \frac{\partial}{\partial \phi} \left(\frac{v_k}{\cos \theta} \right) + \cos \theta \frac{\partial}{\partial \theta} \left(\frac{u_k}{\cos \theta} \right) = e_{\theta\phi_k}$$

$$G_{kj} = g \quad j \geq k$$

$$G_{kj} = g - g(\rho_k - \rho_j) / \rho_0 \quad j < k$$

g = acceleration due to gravity

H_k = k -th layer thickness at rest

h_k = k -th layer thickness

h_k^+ = k -th layer thickness at which entrainment starts

h_k^- = k -th layer thickness at which detrainment starts

$$H_n = D(\phi, \theta) - \sum_{j=1}^{n-1} H_j$$

ϕ = longitude

ρ_0 = constant reference density

ρ_k = k -th layer density, constant in space and time

$\bar{\tau}_w$ = wind stress

$$\bar{\tau}_k = \begin{cases} \bar{\tau}_w & \text{for } k=0 \\ C_k \rho_o |\bar{v}_k - \bar{v}_{k+1}| (\bar{v}_k - \bar{v}_{k+1}) & \text{for } k=1 \dots n-1 \\ C_b \rho_o |\bar{v}_n| \bar{v}_n & \text{for } k=n \end{cases}$$

t = time

θ = latitude

\bar{v}_k = k -th layer velocity = $\bar{e}_\phi u_k + \bar{e}_\theta v_k$

$$\bar{V}_k = h_k \bar{v}_k = \bar{e}_\phi U_k + \bar{e}_\theta V_k$$

$$\omega_k = \begin{cases} 0 & \text{for } k=0, n \\ \omega_k^+ - \omega_k^- - W_k \hat{\omega}_k & \text{for } k=1 \dots n-1 \end{cases}$$

$$\omega_k^+ = \tilde{\omega}_k [\max(0, h_k^+ - h_k) / h_k^+]^p$$

$$\omega_k^- = \tilde{\omega}_k [\max(0, h_k - h_k^-) / h_k^+]^p$$

$$\hat{\omega}_k = (\overline{\omega_k^+ - \omega_k^-}) / \bar{W}_k$$

$\tilde{\omega}_k = k$ -th interface reference diapycnal mixing velocity

$W_k(\phi, \theta) = k$ -th interface weighting factor for global diapycnal mixing designed to conserve mass within a layer in compensation for explicit diapycnal mixing due to $h_k < h_k^+$ (i.e., $\omega_k^+ - \omega_k^-$), and net transport through the lateral boundaries of layer k .

$\overline{X(\phi, \theta)}$ = region wide area average of X

A hydrodynamic reduced-gravity model with n active layers has the lowest layer infinitely deep and at rest, i.e., $\bar{v}_{n+1} = 0$, $h_{n+1} = \infty$, and $\nabla h_{n+1} = 0$. The model equations for the active layers are identical to those for n layer hydrodynamic finite depth model, except that

$$G_{kl} = g(\rho_{n+1} - \rho_k) / \rho_0 \quad l \leq k$$

$$G_{kl} = g(\rho_{n+1} - \rho_l) / \rho_0 \quad l > k$$

$$H_n = \text{constant}$$

$$\bar{\tau}_k = \bar{\tau}_w \quad k = 0$$

$$\bar{\tau}_k = C_k \rho_0 |\bar{v}_k - \bar{v}_{k+1}| (\bar{v}_k - \bar{v}_{k+1}) \quad k = 1 \dots n$$

$$\omega_k = 0 \quad k = 0$$

$$\omega_k = \max(0, \omega_k^+) - \max(0, \omega_k^-) - h_k \hat{\omega}_k \quad k = 1 \dots n$$

APPENDIX B

EXPLANATION OF BAROCLINIC INSTABILITY ANALYSIS

Baroclinic instability analysis involving layers was first discussed by Philips (1954). The basic approach is to introduce to the layered vorticity equations a disturbance stream function with a given wavelength and then solve for the growth and propagation rates of that disturbance. If the disturbance grows with time, then the flow field is baroclinically unstable. The solution of the growth and propagation rates can be difficult or impossible without several simplifying assumptions. In this analysis, bottom topography, friction, and nonlinear effects are neglected at different points. Also the transport in each layer is assumed to be independent of latitude in the region of interest. Since the following appendix deals with instabilities resulting from meridional changes in velocity, the two taken together represent an attempt at describing the instabilities present in an arbitrary, baroclinic zonal flow.

Assuming the absence of friction, it can be shown that the vorticity equation,

$$\frac{d}{dt} \left[\nabla^2 \psi + \beta y + \frac{1}{\rho} \frac{\partial}{\partial z} \left(\frac{\rho}{S} \frac{\partial \psi}{\partial z} \right) \right] = 0 \quad (\text{B1})$$

where

ψ = stream function

$$S = \frac{N^2 D^2}{f^2 L^2}$$

$$N^2 = -\frac{g}{\rho} \frac{\partial \rho}{\partial z}$$

$$D = \text{total depth of fluid column}$$

$$L = \text{representative length scale}$$

can be described for an N layered quasi-geostrophic model (Pedlosky, 1987) by:

$$\frac{d}{dt} \left[\nabla^2 \psi_n + \beta y - \frac{DF}{D_n} \left\{ \frac{\psi_n - \psi_{n-1}}{(\rho_n - \rho_{n-1}) / \rho_o} - \frac{\psi_{n+1} - \psi_n}{(\rho_{n+1} - \rho_n) / \rho_o} \right\} \right] = 0 \quad (n \neq 1, N) \quad (B2)$$

$$\frac{d}{dt} \left[\nabla^2 \psi_1 + \beta y - \frac{DF}{D_1} \left\{ \frac{\psi_1 - \psi_2}{(\rho_2 - \rho_1) / \rho_o} \right\} \right] = 0 \quad (n = 1) \quad (B3)$$

$$\frac{d}{dt} \left[\nabla^2 \psi_N + \beta y - \frac{DF}{D_N} \left\{ \frac{\psi_N - \psi_{N-1}}{(\rho_N - \rho_{N-1}) / \rho_o} \right\} + \eta_B(x, y) \right] = 0 \quad (n = N) \quad (B4)$$

where

$$n = \text{layer number}$$

$$D_n = \text{depth of layer } n$$

$$\rho_n = \text{density of layer } n$$

$$\psi_n = \text{stream function in layer } n$$

$$F = \frac{f^2 L^2}{gD}$$

$$\eta_B = \text{bottom topography.}$$

If we consider a purely zonal flow, so that in each layer

$$\psi_n = \Psi_n(y) \quad (B5)$$

and

$$U_n(y) = -\frac{\partial \Psi_n}{\partial y} \quad (B6)$$

the sloping interface between layers is a source of available potential energy for a disturbance, while the horizontal shear of the zonal flow is a source of kinetic energy. If we let the disturbance stream function, $\varphi(x, y, t)$, be introduced into the flow field, we have

$$\psi_n = \Psi_n(y) + \varphi_n(x, y, t) \quad (B7)$$

Assuming no bottom topography, inserting equation (B7) into equations (B2)-(B4) results in

$$\left[\frac{\partial}{\partial t} + U_n \frac{\partial}{\partial x} \right] q_n + \frac{\partial \varphi_n}{\partial x} \frac{\partial \Pi_n}{\partial y} + \left[\frac{\partial \varphi_n}{\partial x} \frac{\partial q_n}{\partial y} - \frac{\partial \varphi_n}{\partial y} \frac{\partial q_n}{\partial x} \right] = 0 \quad (B8)$$

where

$$q_n = \nabla^2 \varphi_n - \frac{DF}{D_n} \left\{ \frac{\varphi_n - \varphi_{n-1}}{(\rho_n - \rho_{n-1})/\rho_o} - \frac{\varphi_{n+1} - \varphi_n}{(\rho_{n+1} - \rho_n)/\rho_o} \right\} \quad (n \neq 1, N) \quad (B9)$$

$$q_1 = \nabla^2 \varphi_1 - \frac{DF}{D_1} \left\{ \frac{\varphi_1 - \varphi_2}{(\rho_2 - \rho_1)/\rho_o} \right\} \quad (n = 1) \quad (B10)$$

$$q_N = \nabla^2 \varphi_N - \frac{DF}{D_N} \left\{ \frac{\varphi_N - \varphi_{N-1}}{(\rho_N - \rho_{N-1})/\rho_o} \right\} \quad (n = N) \quad (B11)$$

and

$$\frac{\partial \Pi_n}{\partial y} = \beta - \frac{\partial^2 U_n}{\partial y^2} + \frac{DF}{D_n} \left\{ \frac{U_n - U_{n-1}}{(\rho_n - \rho_{n-1})/\rho_o} - \frac{U_{n+1} - U_n}{(\rho_{n+1} - \rho_n)/\rho_o} \right\} \quad (n \neq 1, N) \quad (B12)$$

$$\frac{\partial \Pi_1}{\partial y} = \beta - \frac{\partial^2 U_1}{\partial y^2} - \frac{DF}{D_1} \left\{ \frac{U_2 - U_1}{(\rho_2 - \rho_1)/\rho_o} \right\} \quad (n = 1) \quad (B13)$$

$$\frac{\partial \Pi_N}{\partial y} = \beta - \frac{\partial^2 U_N}{\partial y^2} - \frac{DF}{D_N} \left\{ \frac{U_{N-1} - U_N}{(\rho_N - \rho_{N-1})/\rho_o} \right\} \quad (n = N) \quad (B14)$$

Neglecting terms of $O(\varphi_n^2)$ in equation (B8) yields

$$\left[\frac{\partial}{\partial t} + U_n \frac{\partial}{\partial x} \right] q_n + \frac{\partial \varphi_n}{\partial x} \frac{\partial \Pi_n}{\partial y} = 0 \quad (B15)$$

with lateral boundary conditions of

$$\frac{\partial \varphi_n}{\partial x} = 0, \quad y = \pm 1. \quad (B16)$$

If we seek solutions to equation (B15) in the form

$$\varphi_n = \text{Re}[\phi_n(y)e^{ik(x-ct)}] \quad (B17)$$

equation (B15) becomes

$$(U_n - c) \left[\frac{d^2 \phi_n}{dy^2} - k^2 \phi_n - \frac{DF}{D_n} \left\{ \frac{\phi_n - \phi_{n-1}}{(\rho_n - \rho_{n-1})/\rho_o} - \frac{\phi_{n+1} - \phi_n}{(\rho_{n+1} - \rho_n)/\rho_o} \right\} \right] + \phi_n \frac{\partial \Pi_n}{\partial y} = 0 \quad (B18)$$

$$(U_1 - c) \left[\frac{d^2 \phi_1}{dy^2} - k^2 \phi_1 - \frac{DF}{D_1} \left\{ \frac{\phi_1 - \phi_2}{(\rho_2 - \rho_1)/\rho_o} \right\} \right] + \phi_1 \frac{\partial \Pi_1}{\partial y} = 0 \quad (B19)$$

$$(U_N - c) \left[\frac{d^2 \phi_N}{dy^2} - k^2 \phi_N - \frac{DF}{D_N} \left\{ \frac{\phi_N - \phi_{N-1}}{(\rho_N - \rho_{N-1})/\rho_o} \right\} \right] + \phi_N \frac{\partial \Pi_N}{\partial y} = 0 \quad (B20)$$

with the boundary condition

$$\phi_n = 0 \quad y = \pm 1, \quad (\text{B21})$$

If we assume that the velocities within each layer are independent of y , then the coefficients of equations (B18)-(B20) are constant, and solutions that satisfy equation (B21) can be sought in the form

$$\phi_n = A_n \cos(l_j y) \quad (\text{B22})$$

where

$$l_j = (j + \frac{1}{2})\pi \quad j = 0, 1, 2, \dots \quad (\text{B23})$$

Inserting equation (B22) into equations (B18)-(B20) results in

$$\begin{aligned} (c) & \left[-A_{n-1} \left(\frac{DF}{D_n} \left\{ \frac{1}{(\rho_n - \rho_{n-1})/\rho_o} \right\} \right) - A_{n+1} \left(\frac{DF}{D_n} \left\{ \frac{1}{(\rho_{n+1} - \rho_n)/\rho_o} \right\} \right) \right. \\ & + A_n \left(K^2 + \frac{DF}{D_n} \left\{ \frac{1}{(\rho_n - \rho_{n-1})/\rho_o} + \frac{1}{(\rho_{n+1} - \rho_n)/\rho_o} \right\} \right) \Big] \\ & + \left[A_{n-1} \frac{DF}{D_n} \left\{ \frac{U_n}{(\rho_n - \rho_{n-1})/\rho_o} \right\} + A_{n+1} \left(\frac{DF}{D_n} \left\{ \frac{U_n}{(\rho_{n+1} - \rho_n)/\rho_o} \right\} \right) \right. \\ & \left. + A_n \left(\beta - \frac{DF}{D_n} \left\{ \frac{U_{n-1}}{(\rho_n - \rho_{n-1})/\rho_o} + \frac{U_{n+1}}{(\rho_{n+1} - \rho_n)/\rho_o} \right\} - U_n K^2 \right) \right] = 0 \end{aligned} \quad (\text{B24})$$

$$\begin{aligned} (c) & \left[A_1 \left(K^2 + \frac{DF}{D_1} \left\{ \frac{1}{(\rho_2 - \rho_1)/\rho_o} \right\} \right) - A_2 \left(\frac{DF}{D_1} \left\{ \frac{1}{(\rho_2 - \rho_1)/\rho_o} \right\} \right) \right] \\ & + \left[A_1 \left(\beta - \frac{DF}{D_1} \left\{ \frac{U_2}{(\rho_2 - \rho_1)/\rho_o} \right\} - U_1 K^2 \right) + A_2 \left(\frac{DF}{D_1} \left\{ \frac{U_1}{(\rho_2 - \rho_1)/\rho_o} \right\} \right) \right] = 0 \end{aligned} \quad (\text{B25})$$

$$\begin{aligned}
(c) & \left[A_N \left(K^2 + \frac{DF}{D_N} \left\{ \frac{1}{(\rho_N - \rho_{N-1}) / \rho_o} \right\} \right) - A_{N-1} \left(\frac{DF}{D_N} \left\{ \frac{1}{(\rho_N - \rho_{N-1}) / \rho_o} \right\} \right) \right] \\
& + \left[A_N \left(\beta - \frac{DF}{D_N} \left\{ \frac{U_{N-1}}{(\rho_N - \rho_{N-1}) / \rho_o} \right\} - U_N K^2 \right) + A_{N-1} \left(\frac{DF}{D_N} \left\{ \frac{U_N}{(\rho_N - \rho_{N-1}) / \rho_o} \right\} \right) \right] = 0
\end{aligned} \tag{B26}$$

where

$$K^2 = k^2 + l_j^2. \tag{B27}$$

Equations (B24)–(B26) can be combined to form the matrix equation

$$[c\mathbf{E} + \mathbf{B}] \mathbf{A} = 0 \tag{B28}$$

where \mathbf{A} is vector containing the coefficients, A_n , in equation (B22), c is defined in equation (B17) and \mathbf{E} and \mathbf{B} are matrices defined by equations (B24) - (B26) and are functions of the disturbance wave number, K . Nontrivial solutions for \mathbf{A} are possible only if

$$\det[c\mathbf{E} + \mathbf{B}] = 0 \tag{B29}$$

Some matrix manipulation yields

$$\det[c\mathbf{E} + \mathbf{E}^{-1}\mathbf{B}\mathbf{E}] = 0 \tag{B30}$$

$$\det[(c\mathbf{I} + \mathbf{E}^{-1}\mathbf{B})\mathbf{E}] = 0 \tag{B31}$$

$$\det[c\mathbf{I} + \mathbf{E}^{-1}\mathbf{B}] \det[\mathbf{E}] = 0 \tag{B32}$$

Equation (B32) will be satisfied if either $\det[\mathbf{E}]$ is zero, or the more interesting

$$\det[c\mathbf{I} + \mathbf{E}^{-1}\mathbf{B}] = 0 \tag{B33}$$

The values of the phase speed, c , are the opposite of the eigen values of the matrix $\mathbf{E}^{-1}\mathbf{B}$. According to equation (B17), the disturbance will propagate at a rate of $\text{Re}[kc]$ and grow at the rate of $-\text{Im}[kc]$. So growth and propagation rates as functions of wave number can be determined by solving for the eigen values of the matrix $\mathbf{E}^{-1}\mathbf{B}$ as a function of K . Since complex eigen values of a matrix exist as complex conjugate pairs, the appearance of any complex values of c guarantees both a negative and positive value of c_i and, therefore, exponential growth of the disturbance.

The solution of the growth rate is non-unique. Since there are N eigen values for each wave number, there will be N possible growth and propagation rates. Since the growth rates will be of different magnitudes and correspond to different propagation speeds, the fastest growing stationary disturbance will dominate the mean flow field.

APPENDIX C

EXPLANATION OF BAROTROPIC INSTABILITY ANALYSIS

Barotropic instability analysis was first discussed by Kuo (1949). The basic approach is to introduce to the barotropic vorticity equation a disturbance stream function with a given wavelength and then solve for the growth and propagation rates of that disturbance. If the disturbance grows with time, then the flow field is barotropically unstable. Several simplifying assumptions make the problem tractable. Here we will follow the same procedure as Appendix B.

If we consider a purely zonal barotropic flow, so that

$$\psi = \Psi(y) \tag{C1}$$

and

$$U(y) = -\frac{\partial \Psi}{\partial y} \tag{C2}$$

and let the barotropic disturbance stream function, $\phi(x,y,t)$, be introduced into the flow field, the horizontal shear of the zonal flow is a source of energy for the disturbance.

The new stream function is

$$\psi = \Psi(y) + \phi(x, y, t) \tag{C3}$$

The barotropic equivalent to (B8) is

$$\left[\frac{\partial}{\partial t} + U \frac{\partial}{\partial x} \right] q + \frac{\partial \varphi}{\partial x} \frac{\partial \Pi}{\partial y} + \left[\frac{\partial \varphi}{\partial x} \frac{\partial q}{\partial y} - \frac{\partial \varphi}{\partial y} \frac{\partial q}{\partial x} \right] = 0 \quad (C4)$$

where

$$q = \nabla^2 \varphi \quad (C5)$$

$$\frac{\partial \Pi}{\partial y} = \beta - \frac{\partial^2 U}{\partial y^2} \quad (C6)$$

with lateral boundary conditions of

$$\frac{\partial \varphi}{\partial x} = 0, \quad y = \pm 1. \quad (C7)$$

If we seek solutions to equation (C4) in the form

$$\varphi = \text{Re}[\phi(y)e^{ik(x-ct)}] \quad (C8)$$

equation (C4) becomes

$$(U - c) \left[\frac{d^2 \phi}{dy^2} - k^2 \phi \right] + \phi \frac{\partial \Pi}{\partial y} - \frac{d\phi}{dy} \left[\frac{d^2 \phi}{dy^2} - k^2 \phi \right] + \phi \frac{\partial}{\partial y} \left[\frac{d^2 \phi}{dy^2} + \frac{d^2 \phi}{dx^2} \right] = 0 \quad (C9)$$

with the boundary condition

$$\phi = 0 \quad y = \pm 1. \quad (C10)$$

Pedlosky (1987) has shown that the barotropic stability problem posed by equation (C9)

is equivalent to a *baroclinic* disturbance to the *barotropic* current if k^2 is replaced with μ^2

where

$$\mu^2 = k^2 + \lambda \quad (C11)$$

and λ is the eigen value of a Sturm-Liouville problem describing the vertical structure of the streamfunction. So the dynamics of an arbitrary *baroclinic* perturbation of the *barotropic* current can be described entirely in terms of the equivalent *barotropic* mode with a modified wavelength. Since we are interested in the presence of barotropic instabilities and not the actual wavelength of the disturbances, we continue our analysis with equation (C9).

Since the disturbance velocities are related to the stream function as

$$\frac{d\phi}{dy} = -u', \quad (C12)$$

$$\frac{d\phi}{dx} = v', \quad (C13)$$

equation (C9) can be rewritten as

$$(u - c) \left[\frac{d^2 \phi}{dy^2} - k^2 \phi \right] + \phi \frac{\partial}{\partial y} \left[f + \frac{dv'}{dx} - \frac{du}{dy} \right] = 0 \quad (C14)$$

where

$$u = \text{total zonal velocity, } U + u'.$$

The stability problem described by equation (C14) with boundary conditions (C10) can be viewed as an eigen value problem in the following sense: A nontrivial solution of ϕ is only possible for specific values of c , which acts as the eigen value. As in the analysis of baroclinic instability, the existence of a complex phase speed, c , guarantees exponential growth.

Since it is impossible in general to determine the values of c for an arbitrary velocity profile, we will instead establish a weaker criterion that is necessary but not sufficient for instability. If equation (C14) is multiplied by the complex conjugate of ϕ and integrated across the domain, we get

$$-\int_{-1}^1 \left(\left| \frac{d\phi}{dy} \right|^2 + k^2 |\phi|^2 \right) dy + \int_{-1}^1 \frac{\partial Q / \partial y}{u - c} |\phi|^2 dy = 0 \quad (\text{C15})$$

where the absolute vorticity, Q , is described by

$$Q = f + \frac{\partial v}{\partial x} - \frac{\partial u}{\partial y} \quad (\text{C16})$$

after an integration by parts. The imaginary part of equation (C15) is

$$c_i \int_{-1}^1 \frac{\partial Q}{\partial y} \frac{|\phi|^2}{|u - c|^2} dy = 0 \quad (\text{C17})$$

For equation (C17) to be satisfied for nontrivial values of ϕ , either c_i must be zero, which according to equation (C8), would result in a wave that is stable, or the integral must be zero. This second condition requires that dQ/dy change sign somewhere within the domain of integration. The change of sign does not guarantee that barotropic instability exists, since c_i could still be zero even if the integral is zero, but the change of sign is necessary for a barotropic instability to exist.

REFERENCES

- Andrews, J. C., M. W. Lawrence, and C. S. Nilsson, 1980: Observations of the Tasman Front, *J. Phys. Oceanogr.*, **10**, 1854-1869.
- Bryan, K. and M. D. Cox, 1968: A nonlinear model of an ocean driven by wind and differential heating, I, Description of three-dimensional velocity and density fields, *J. Atmos. Sci.*, **25**, 945-967.
- Bye, J. A. T., R. A. Heath, and T. W. Sag, 1979: A numerical model of the oceanic circulation around New Zealand, *J. Phys. Oceanogr.*, **9**, 892-899.
- Campos, E. J. D., and D. B. Olson, 1991: Stationary Rossby waves in western boundary current extensions, *J. Phys. Oceanogr.*, **21**, 1202-1224.
- Carter, L., and J. L. Wilkin, 1999: Abyssal circulation around New Zealand – a comparison between observations and a global circulation model, *Marine Geology*, **159**, 221-239.
- Chiswell, S. M., 1996: Variability in the Southland Current, New Zealand, *N.Z. J. Mar. Freshwater Res.*, **30**, 1-17.
- Chiswell, S. M., J. Toole, and J. Church, 1997: Transports across the Tasman Sea from WOCE repeat sections: the East Australian Current 1990-94, *N.Z. J. Mar. Freshwater Res.*, **31**, 469-475.
- Cushman-Roisin, B., 1994: *Introduction to geophysical fluid dynamics*, Prentice Hall, 320 pp.
- Da Silva, I. C. A., G. R. Flierl, and W. S. Brown, 1999: Dynamics of separating western boundary currents, *J. Phys. Oceanogr.*, **29**, 119-144.
- Davis, R. E., 1998: Preliminary results from directly measuring middepth circulation in the tropical and south Pacific, *J. Geophys. Res.*, **103**, 24619-24639.

- Denham, R. N., and F. J. Crook, 1976: The Tasman Front, *N. Z. J. Mar. Freshwater Res.*, **10**, 15-30.
- De Szoek, R. A., 1987: On the wind-driven circulation of the South Pacific Ocean, *J. Phys. Oceanogr.*, **17**, 613-630.
- Godfrey, J. S., 1973: Comparison of the East Australian Current with the western boundary flow in Bryan and Cox's (1968) numerical model ocean, *Deep-Sea Res.*, **20**, 1059-1076.
- Godfrey, J. S., 1989: A Sverdrup model of the depth-integrated flow for the world ocean allowing for island circulations, *Geophys. Astrophys. Fluid Dyn.*, **45**, 89-112.
- Godfrey, J. S., 1996: The effect of the Indonesian throughflow on ocean circulation and heat exchange with the atmosphere: A review, *J. Geophys. Res.*, **101**, 12217-12237.
- Godfrey, J. S., G. R. Creswell, T. J. Golding, A. F. Pearce, and R. Boyd, 1980: The separation of the East Auckland Current, *J. Phys. Oceanogr.*, **10**, 430-440.
- Gordon, A. L., 1975: An Antarctic oceanographic section along 170E, *Deep-Sea Research*, **22**, 357-377.
- Haidvogel, D. B., and W. R. Holland, 1978: The stability of ocean currents in eddy-resolving general circulation models, *J. Phys. Oceanogr.*, **8**, 393-413.
- Haltiner, G. J., and F. L. Martin, 1957: *Dynamical and Physical Meteorology*, McGraw-Hill, 470 pp.
- Heath, R. A., 1972: The Southland Current, *N. Z. J. Mar. Freshwater Res.*, **6**, 497-533.
- Heath, R.A., 1985a: A review of the physical oceanography of the seas around New Zealand – 1982, *N. Z. J. Mar. Freshwater Res.*, **19**, 79-124.
- Heath, R. A., 1985b: Large-scale influence of the New Zealand seafloor topography on western boundary currents of the south Pacific Ocean, *Aust. J. Mar. Freshwater Res.*, **36**, 1-14.
- Heburn, G. W., 1994: The dynamics of the seasonal variability of the western Mediterranean circulation, *Seasonal and Interannual Variability of the Western Mediterranean Sea, Coastal Estuarine Stud.*, vol. 46, P. E. LaViolette, Ed., AGU Washington, D. C., 249-285.

- Hellerman, S., and M. Rosenstein, 1983: Normal monthly wind stress over the world ocean with error estimates, *J. Phys. Oceanogr.*, **13**, 1093-1104.
- Hogan, P. J. and H. E. Hurlburt, 2000: Impact of upper ocean - topographic coupling and isopycnal outcropping in Japan/East Sea models with $1/8^\circ$ to $1/64^\circ$ resolution, *J. Phys. Oceanogr.*, **30**, 642-657.
- Holland, W. R., and L. B. Lin, 1975: On the generation of mesoscale eddies and their contribution to the oceanic general circulation, I: A preliminary numerical experiment, *J. Phys. Oceanogr.*, **5**, 642-657.
- Holland, W. R., 1978: Role of mesoscale eddies in general circulation of ocean - numerical experiments using a wind-driven quasi-geostrophic model, *J. Phys. Oceanogr.*, **8**, 363-392.
- Hurlburt, H. E., and J. D. Thompson, 1980: A numerical study of Loop Current intrusions and eddy-shedding, *J. Phys. Oceanogr.*, **10**, 1611-1651.
- Hurlburt, H. E., and J. D. Thompson, 1982: The dynamics of the Loop Current and shed eddies in a numerical model of the Gulf of Mexico, *Hydrodynamics of Semi-Enclosed Seas*, J. C. J. Nihoul, Ed., Elsevier, New York, 243-297.
- Hurlburt, H. E., and J. D. Thompson, 1984: Preliminary results from a numerical study of the New England Seamount Chain influence on the Gulf Stream. *Predictability of Fluid Motions*, G. Holloway and B. J. West. Eds., Am. Inst. of Phys., College Park, Md, 489-504.
- Hurlburt, H. E., A. J. Wallcraft, W. J. Schmitz Jr., P. J. Hogan, and E. J. Metzger, 1996: Dynamics of the Kuroshio/Oyashio current system using eddy-resolving models of the north Pacific Ocean, *J. Geophys. Res.*, **101**, 941-976.
- Hurlburt, H.E., and E. J. Metzger, 1998: Bifurcation of the Kuroshio Extension at the Shatsky Rise, *J. Geophys. Res.*, **103**, 7549-7566.
- Huyer, A., R. L. Smith, P. J. Stabeno, J. A. Church, and N. J. White, 1988: Currents off South-eastern Australia: results from the Australian Coastal Experiment, *Aust. J. Mar. Freshwater Res.*, **39**, 245-288.
- Kuo, H. L., 1949: Dynamic instability of two-dimensional non-divergent flow in a barotropic atmosphere, *J. Meteorol.*, **6**, 105-122.
- Laing, A. K., B. R. Stanton, and P. G. Challenor, 1996: Variations in the East Auckland Current from satellite radar altimeter data, *N.Z. J. Mar. Freshwater Res.*, **30**, 175-191.

- Levitus, S., 1982: Climatological atlas of the world ocean, *NOAA Prof. Pap. 13*, 173 pp., U. S. Govt. Print. Off., Washington, D.C.
- Lighthill, M. J., 1969: Dynamic response of the Indian Ocean to onset of the Southwest Monsoon, *Philos. Trans. R. Soc. London, Ser. A*, **265**, 45-92.
- Luyten, J. R., J. Pedlosky, and H. Stommel, 1983: The ventilated thermocline, *J. Phys. Oceanogr.*, **13**, 293-309.
- McWilliams, J. C. and R. C. Flierl, 1979: On the evolution of isolated nonlinear vortices, *J. Phys. Oceanogr.*, **9**, 1155-1182.
- Mesinger, F., and A. Arakawa, 1976: Numerical methods used in atmospheric models, *GARP Publ. Ser.*, **17**, World Meteorol. Org., Geneva, Switzerland, 64 pp.
- Metzger, E. J., and H. E. Hurlburt, 1996: Coupled dynamics of the South China Sea, the Sulu Sea and the Pacific Ocean, *J. Geophys. Res.*, **101**, 12331-12352.
- Metzger, E. J., H. E. Hurlburt, J. C. Kindle, Z. Sirkes, and J. Pringle, 1992: Hindcasting of wind-driven anomalies using a reduced-gravity global ocean model, *Mar. Technol. Soc. J.*, **26**, 23-32.
- Mitchell, J. L., W. J. Teague, G. A. Jacobs, and H. E. Hurlburt, 1996: Kuroshio Extension dynamics from satellite altimetry and a model simulation, *J. Geophys. Res.*, **101**, 1045-1058.
- Mitchum, G. T., 1995: The source of 90-day oscillations at Wake Island, *J. Geophys. Res.*, **100**, 2459-2475.
- Moore, D. R., and A. J. Wallcraft, 1998: Formulation of the NRL Layered Ocean Model in spherical coordinates, NRL CR 7323-96-0005, 24 pp., Nav. Res. Lab., Stennis Space Center, MS.
- Moore, M. L., and J. L. Wilkin, 1998: Variability in the South Pacific Deep Western Boundary Current from current meter observations and a high-resolution global model, *J. Geophys. Res.*, **103**, 5439-5457.
- Morey, S. L., J. F. Shriver, and J. J. O'Brien, 1999: The effects of Halmahera on the Indonesian Throughflow, *J. Geophys. Res.*, **104**, 23281-23296.
- Mulhearn, P.J., 1987: The Tasman Front: A study using satellite infrared imagery, *J. Phys. Oceanogr.*, **17**, 1148-1155.

- Munk, W. H., 1950: On the wind-driven ocean circulation, *J. Meteorol.*, **7**, 79-93.
- Murphy, S. J., H. E. Hurlburt, and J. J. O'Brien, 1999: The connectivity of eddy variability in the Caribbean Sea, the Gulf of Mexico, and the Atlantic Ocean, *J. Geophys. Res.*, **104**, 1431-1453.
- National Oceanic and Atmospheric Administration, 1986: ETOP05 digital relief of the surface of the earth, *Data Announce. 86-MGG-07*, Natl. Geophys. Data Center, Washington, D. C.
- Ou, H. W., and W. P. M. De Ruijter, 1986: Separation of an inertial boundary current from a curved coastline, *J. Phys. Oceanogr.*, **16**, 280-289.
- Pedlosky, J., 1987: *Geophysical fluid dynamics*, Springer-Verlag, 710 pp.
- Phillips, N. A., 1954: Energy transformations and meridional circulations associated with simple baroclinic waves in a two-level, quasi-geostrophic model, *Tellus*, **6**, 273-286.
- Ridgway, K. R. and J. S. Godfrey, 1994: Mass and heat budgets in the East Australian Current: A direct approach, *J. Geophys. Res.*, **99**, 3231-3248.
- Ridgway, K. R. and J. S. Godfrey, 1997: Seasonal cycle of the East Australian Current, *J. Geophys. Res.*, **102**, 22921-22936.
- Roemmich, D. and P. Sutton, 1998: The mean and variability of ocean circulation past northern New Zealand: Determining the representativeness of hydrographic climatologies, *J. Geophys. Res.*, **103**, 13041-13054.
- Semtner, A. J., and R. M. Chervin, 1992: Ocean general circulation from a global eddy-resolving model, *J. Geophys. Res.*, **97**, 5493-5550.
- Shriver, J. F., and H. E. Hurlburt, 1997: The contribution of the global thermohaline circulation to the Pacific to Indian Ocean throughflow via Indonesia, *J. Geophys. Res.*, **102**, 5491-5511.
- Stanton, B. R., 1976: An oceanic frontal jet near the Norfolk Ridge northwest of New Zealand, *Deep-Sea Res.*, **23**, 821-829.
- Stanton, B. R., 1979: The Tasman Front, *N.Z. J. Mar. Freshwater Res.*, **13**, 201-214.

- Stanton, B. R., 1981: An oceanographic survey of the Tasman Front, *N.Z. J. Mar. Freshwater Res.*, **15**, 289-297.
- Stanton, B. R., P. J. H. Sutton, and S. M. Chiswell, 1997: The East Auckland Current, 1994-95, *N. Z. J. Mar. Freshwater Res.*, **31**, 537-549.
- Sverdrup, H. U., 1947: Wind-driven currents in the baroclinic ocean: With application to the equatorial currents of the eastern Pacific, *Proceedings of the National Academy of Sciences USA*, **33**, 318-326.
- Talley, L. D., 1983: Radiating instabilities of thin baroclinic jets, *J. Phys. Oceanogr.*, **13**, 2161-2181.
- Uddstrom, M. J., and N. A. Oien, 1999: On the use of high-resolution satellite data to describe the spatial and temporal variability of sea surface temperatures in the New Zealand region, *J. Geophys. Res.*, **104**, 20729-20751.
- Wallcraft, A. J., 1991: The Navy Layered Ocean Model users guide. NOARL Report 35, 21 pp., Nav. Res. Lab., Stennis Space Center, MS.
- Wallcraft, A. J., and D. R. Moore, 1997: A scalable implementation of the NRL Layered Ocean Model, *Parallel Computing*, **23**, 2227-2242.
- Warren, B. A., 1970: General circulation of the South Pacific, *Scientific Exploration of the South Pacific*, Warren S. Wooster, Ed., U. S. Nat. Acad. Sci., 33-49.
- Warren, B. A., 1981: Deep circulation of the world ocean, *Evolution of Physical Oceanography*, Warren, B. A., Wunsch, C., Eds., MIT Press, 6-41.

BIOGRAPHICAL SKETCH

Charles Edward Tilburg was born in Shalimar, Florida on October 6, 1970, the son of James Howard and Carolyn Giles Tilburg. In 1988, after graduating from Groton School in Groton, Massachusetts, he entered The University of Texas at Austin. He received the degree of Bachelor of Science in Aerospace Engineering in December, 1992, and the degree of Masters of Science in Environmental Engineering in December, 1994. After working for two years as an environmental engineer with INTERA, Inc.. in Austin, Texas, he taught high school math and science at the Brent School in Baguio City, Philippines. In 1997, he entered the graduate school of the Florida State University to pursue a Ph.D. in Physical Oceanography.